THEORY AND OBSERVATIONS OF RUNAWAY ELECTRONS IN THE SOLAR WIND

By

Konstantinos Horaites

A dissertation submitted in partial fulfillment of the

requirements for the degree of

Doctor of Philosophy

(Physics)

at the

UNIVERSITY OF WISCONSIN – MADISON

2019

Date of final oral examination: May 14, 2019

The dissertation is approved by the following members of the Final Oral Committee:

Stanislav Boldyrev, Professor, Physics

Jan Egedal, Professor, Physics

Cary Forest, Professor, Physics

Carl Sovinec, Professor, Engineering Physics

Ellen Zweibel, Professor, Astronomy and Physics

Abstract

In this thesis, I develop a kinetic theory that describes the population of thermal runaway electrons observed ubiquitously in the solar wind, which is commonly known as the "strahl". I solve the drift kinetic equation in the high-energy, magnetic field-aligned regime that is relevant to the strahl, to find the form of this electron population's gyrotropic distribution function. I then compare the model with direct measurements of the distribution function in the fast solar wind, sampled in the ecliptic at 1 AU by the Wind satellite's SWE strahl detector. This instrument's high angular resolution allowed it to characterize the angular width of the narrow strahl distribution. I demonstrate that the model accurately predicts the angular width of the strahl, in particular its dependence on the particle energy and background density. In this model, the angular diffusion experienced by the strahl is attributed entirely to Coulomb collisions, neglecting other diffusive mechanisms such as wave-particle interactions that may also impact the strahl distribution. Finally, I assess the kinetic stability of the model; I present a linear stability analysis of a distribution comprised of the model strahl function and a drifting Maxwellian "core" population. The stability analysis is performed numerically using the LEOPARD solver (3). Surprisingly, I find that the modeled core-strahl distribution is stable with respect to the whistler wave mode. The whistler mode is often invoked as a source of "anomalous scattering" of the strahl, as these waves may interact with strahl electrons via the cyclotron resonance. The analysis, however, does yield two growing modes which exhibit a Landau resonance with the thermal core electrons: namely, the kinetic Alfvén and magnetosonic modes.

Acknowledgments

I would like to first thank the members of my thesis committee for lending their time and expertise to review this dissertation. I am otherwise thankful to the committee members—either for their careful instruction in the classroom setting, or for their inquiries and discussions over the years that have amounted to a significant impact on the work presented here. To my advisor, Stanislav Boldyrev, I am deeply grateful. As a mentor, Stas has been flexible and supportive—I vividly remember when I first proposed the research topic that would lead to my thesis work, and his encouragement and engagement at that time and onward has meant the world to me. Stas has always made himself available, whether to answer a question or discuss some new data, and I enjoyed our many discussions together. His passion for the subject matter—what Feynman called "the pleasure of finding things out"—is a great inspiration, and I hope I can carry that same passion with me throughout my career.

My work in space physics, and on electron kinetics specifically, began as I was pursuing my undergraduate degree at UC-Berkeley. I would like to thank my group at the Space Sciences Laboratory, in particular Chadi Salem, Stuart Bale, and Marc Pulupa—their guidance influenced my future in no small way. They are among a host of collaborators that directly contributed to the publications compiled in this thesis; I would like to additionally acknowledge my collaborators Sergei Krasheninnikov, Lynn B. Wilson III, Adolfo Viñas, Jan Merka, Patrick Astfalk, Frank Jenko, and Mikhail Medvedev. A special thanks is owed to past and current members of the Wind team at NASA's Goddard Space Flight Center, who helped me revitalize the SWE strahl detector data that are

studied extensively in this work; Richard Fitzenreiter, in particular, graciously took time from his retirement to help me understand the nuances of this data set. James Callen, who took an interest in my work at Wisconsin, was another great resource as he introduced me to aspects of kinetic theory during our office discussions. Like many students in our department, I owe thanks to Jim Reardon, who helped me develop as a budding teacher and physicist.

Many friends and peers provided help and support during my long journey through graduate school. I would like to thank my former officemates Vladimir Zhdankin and Robert Siller, for their companionship and occasional feedback on my work. Yuguang Tong, whom I met in my Berkeley days, has been another good friend and I was happy to find our paths would cross many times again. I benefited from discussions with a small cohort of students at Wisconsin who shared an interest in the solar wind, among them Emily Lichko, Ethan Peterson, and Doug Endrizzi. I would also like to thank the multitude of people I have met through Ambrosia Cooperative, where I have lived for the second half of my graduate career; thanks to their friendship I have never been so rich with community, nor felt such a sense of place and purpose.

A thesis acknowledgment wouldn't be complete without mention of one's family. To my loving parents Andreas and Lorna, and dearest siblings Dimitri, Alice, Nik, and Alekka: I am eternally fortunate to have you as my first co-authors, in this strange life. If you will forgive the metaphor—but every day I see myself reflected in you in some small way, and I can think of no warmer feeling.

Contents

Chapter 1

Introduction

1.1 Heat Flow, Plasmas, and Collisions

It is well-known that when two bodies of unequal temperature come into contact, heat flows from the hotter body to the colder one. This phenomenon, which is called "thermal conduction", arises generally in the presence of a temperature gradient in all phases of matter: solids, liquids, gases, and plasmas. Thermal conduction is the result of many microscopic interactions among the constituent particles in the system; a region of high temperature contains particles that possess more energy on average than the particles in regions of low temperature, and heat is preferentially transferred to the cooler regions as particles collide and exchange energy. In some systems, it is possible for individual particles to transfer energy in the system simply by migrating into other regions (carrying their energy with them), with negligible interaction with other particles. These are known as "runaway" particles in the context of plasma physics, and they will be of central interest in this thesis. Specifically, we will be examining "thermal runaway" (26) electrons that are emitted by the sun, that are observed to flow through the plasma found in interplanetary space known as the solar wind.

A plasma is an ionized gas, in which electrons are dissociated from atomic nuclei. Electrons and ions are then free to move independently, and because all these particles

are charged, they exert electromagnetic forces on each other. In particular, a particle's motion is altered by the electric Coulomb force that it feels from the many surrounding particles. These interactions are known as Coulomb "collisions", even though a significant effect comes from the cumulative collisions that happen over a very large range—on the order of the electron Debye length, which is in practice many orders of magnitude larger than the typical atomic size. This picture should be contrasted with that of a neutral gas, where the neutral atoms will only interact if they approach each other within an atomic radius or so.

The process of particle scattering due to Coulomb collisions in a plasma is highly dependent on the energy of the scattered particle; it turns out that more energetic particles are scattered much less effectively. It is a common introductory problem in plasma physics to show that the frequency of large-angle collisions—i.e., collisions between charged particles that would deflect the incoming particle's velocity by 90 degrees or more—scales with the particle speed (v) as v^{-3}. The same speed (or energy) dependence holds true for the occurrence rate of the many diffusive small-angle collisions described above, which have a greater impact overall than the large-angle collisions.

In order to fully understand the processes by which energy is transferred between different regions in a plasma, one must apply a theory that can resolve these microphysical effects—namely, the advection of energy-carrying particles, and the electrostatic Coulomb interactions that mediate their trajectories. Although these processes naturally involve the motions of individual particles, it is not practical to treat the (many) particles individually and to solve for their trajectories from the classical equations of motion. Rather, one averages over the many possible realizations of the system, and

assumes that a particle has only some *probability* of being found with any particular velocity at any particular location; the "equations of motion" instead govern the evolution of these probabilities with time. This approach is known in plasma physics as *kinetic theory*.

1.2 Kinetic Theory

Kinetic theory provides a detailed description of plasma dynamics, by characterizing the classical motion of charged particles in terms of a "distribution function" $f(\mathbf{x}, \mathbf{v}, t)$. Loosely speaking, the function represents the relative probability that at time t, an individual particle will be found at a given position $\mathbf{x}$ with a given velocity $\mathbf{v}$.[1] Formally, the distribution function is a strictly non-negative scalar function of a seven-dimensional phase space—three spatial and velocity dimensions, plus time. At any given instant (neglecting the independent variable t), the distribution function is normalized to the volume density of particles, $n_s(\mathbf{x})$:

$$\int f_s(\mathbf{x}, \mathbf{v}) d^3v = n_s(\mathbf{x}). \tag{1.1}$$

Here, as throughout the chapter, the subscript s denotes the particle species.

The kinetic equation, which governs the time-evolution of $f_s(\mathbf{x}, \mathbf{v}, t)$ for a particle species with charge q_s and mass m_s, has the well-known form:

$$\frac{\partial f_s}{\partial t} = -\mathbf{v} \cdot \frac{\partial f_s}{\partial \mathbf{x}} - \frac{q_s}{m_s}\Big[\mathbf{E}(\mathbf{x}, t) + \mathbf{v} \times \mathbf{B}(\mathbf{x}, t)\Big] \cdot \frac{\partial f_s}{\partial \mathbf{v}} + \hat{C}(f_s), \tag{1.2}$$

[1] The function f is analogous to a probability density function; the quantity $f(\mathbf{x}, \mathbf{v}, t) d^3x d^3v$ represents the expected number of particles (at time t) found within an infinitesimal phase space volume $d^3x d^3v$, centered at position $\mathbf{x}$ and velocity $\mathbf{v}$.

where $\mathbf{E}(\mathbf{x}, t)$ and $\mathbf{B}(\mathbf{x}, t)$ denote the spatially and temporally varying electric and magnetic fields, respectively. The time-evolution of the distribution function, $\frac{\partial f_s}{\partial t}$, depends on the three terms on the right-hand side of eq. 1.2, here listed from left to right: 1) the advection of particles through space, 2) the Lorentz force $q_s(\mathbf{E} + \mathbf{v} \times \mathbf{B})$ which alters particle velocities, and 3) Coulomb collisions. Here the operator $\hat{C}(f_s)$, the "Coulomb collision operator", represents the cumulative effect of electrostatic scattering events, which stochastically deflect particle velocities. These Coulomb collisions occur over spatial scales equal to or less than the Debye length. The Coulomb collision operator and its various approximations are well-studied topics in plasma physics. For background on the collision operator see section C.2, where relevant derivations on the operator's form (as it appears in this work) can be found. Here we will simply note that the diffusive Coulomb collisions tend to drive the distribution towards a Maxwellian (i.e. Gaussian) function of velocity, a consequence of Boltzmann's famous "H-theorem" (e.g., 10).

In a magnetized plasma—i.e., a plasma in which the typical Larmor radius (or "gyroradius") r_L is much smaller than the scale of the system—charged particles move in circular orbits around the local magnetic field $\mathbf{B}$. An individual particle's spiral motion around the field can be described in terms of its parallel and perpendicular velocity components, i.e., the field-perpendicular and -parallel components of the velocity, $v_\perp$ and $v_\parallel$:

$$v_\parallel \equiv \mathbf{v} \cdot \mathbf{B}/B \tag{1.3}$$

$$v_\perp = \sqrt{v^2 - v_\parallel^2} \tag{1.4}$$

In this context, when the distribution is averaged over timescales on the order of the

particle gyroperiod, the function $f(\mathbf{v})$ will appear symmetrical under rotations around the unit vector $\mathbf{B}/B$—i.e., the distribution is said to be "gyrotropic". It is then superfluous to treat f as a function of three independent velocity variables (v_x, v_y, v_z), since the gyromotion effectively reduces the number of velocity degrees of freedom from 3 to 2. Rather, for many applications it is appropriate to apply the *drift kinetic equation* (37), which we may think of as a reduced version of equation (1.2), to analyze the kinetic properties of the system. The drift kinetic equation only has 2 independent velocity variables—e.g., $v_\perp$ and $v_\parallel$, or some equivalent set of variables—a consequence of the equation's derivation, which begins with eq. 1.2 and averages over the particle gyromotion.

The solar wind, the principal system considered in this thesis, is a highly magnetized plasma. These magnetic fields are generated by the solar dynamo (plasma motions in the sun that convert kinetic energy into magnetic energy), and ultimately dragged out into interplanetary space with the solar wind as it moves away from the sun. In the space environment just outside the Earth's magnetosphere, the Larmor radii of typical ("thermal") electrons and protons are about 2 and 80 kilometers, respectively (80); very small compared to the scale of Earth-Sun distance of 1.5×10^8 kilometers. The body of this thesis will concern electrons in the solar wind; our analytical modeling of the (steady-state) electron distribution will be derived from the drift kinetic equation (see section C.1 for details).

1.3 The Solar Wind

The solar wind is a plasma continuously emanated by the sun in all directions, that is accelerated to supersonic speeds by strong pressure gradients present in the region of the sun's atmosphere known as the solar corona. The first theoretical model of the solar wind was developed by Eugene Parker in 1958 (51), and satellite observations would soon confirm the existence of this fast-moving plasma directly. We will here review this system's basic properties.

The solar wind flow can be roughly approximated as a constant-speed, isotropic, radial outflow from the sun. Magnetic fields that are present in the coronal plasma are carried outwards with the solar wind flow—a consequence of the frozen-in flux theorem of ideal magnetohydrodynamics (MHD), which accurately describes the highly conductive heliospheric environment. Because the sun is rotating, the magnetic field in the plane of the sun's equator is drawn into a spiral pattern[2]. The field lines of this so-called "Parker spiral" are pictured schematically Figure 1; this field line configuration is very similar to that which is observed in the ecliptic (the plane defined by Earth's orbit around the Sun), because the sun's equatorial plane is nearly aligned with the ecliptic plane.

Of course, the picture shown in Figure 1 is only an idealization of a more complex system. Measurements by the Ulysses satellite (46) revealed, for instance, that the average speed v_{sw} of the solar wind depends on the heliographic latitude; the solar wind emitted near the sun's equator is typified by the so-called "slow" wind ($v_{sw} \sim 400$ km/sec), while observations above the sun's poles usually exhibit a "fast" wind ($v_{sw} \gtrsim 700$ km/sec).

[2]In particular, the line conservation property of ideal MHD, which states that two regions that are connected in space by a field line will stay so connected, can be used to derive the form of the Parker spiral.

The solar wind velocity is known to also vary with distance from the sun; upcoming observations of the inner heliosphere are expected to bound the region over which this acceleration occurs, and to reveal the physical mechanism behind the anomalous heating of the solar wind (e.g., 79). Besides these large-scale trends, the solar wind changes dynamically at any given location—for instance, coronal mass ejections (CMEs), which are large explosions of particles (with higher density than the background plasma) originating near the Sun, are observed to pass by Earth on an almost weekly basis (e.g., 58). Even within solar wind streams left unperturbed by a passing CME, the flows are ubiquitously observed to exhibit strong turbulent fluctuations; the magnetic field vector and bulk velocity fluctuate stochastically about their mean values. The turbulence is believed to be driven by large-scale motion—say, the motion of magnetic "footpoints" near the sun's surface (e.g., 12)—that develops into a spectrum of fluctuations at smaller scales through a forward cascade.

The vector $\mathbf{v_{sw}}$, as depicted in Figure 1, can be understood as the bulk flow of the solar wind ions. By "ions", we here basically refer to the proton population; the solar wind ions are comprised mostly of protons, with $\lesssim$5% relative abundance of Helium nuclei (see, e.g., 1) and only trace representation ($\lesssim$1% abundance total) of the other "minor" ions. The electrons are observed to move with the same *bulk* (average) speed as the ions (17). However, it should be noted that while the ion distribution $f_i(\mathbf{v})$ is highly concentrated around $\mathbf{v_{sw}}$ (i.e., the ions all move away from the sun with roughly the same speed), the electron distribution $f_e(\mathbf{v})$ is much more spread out in phase space. Many electrons are moving away from the sun with speeds significantly (at least a factor of 2) greater than v_{sw}, and many electrons are observed to actually be moving *towards* the sun. This difference is due to the fact that while the electrons and protons are observed to

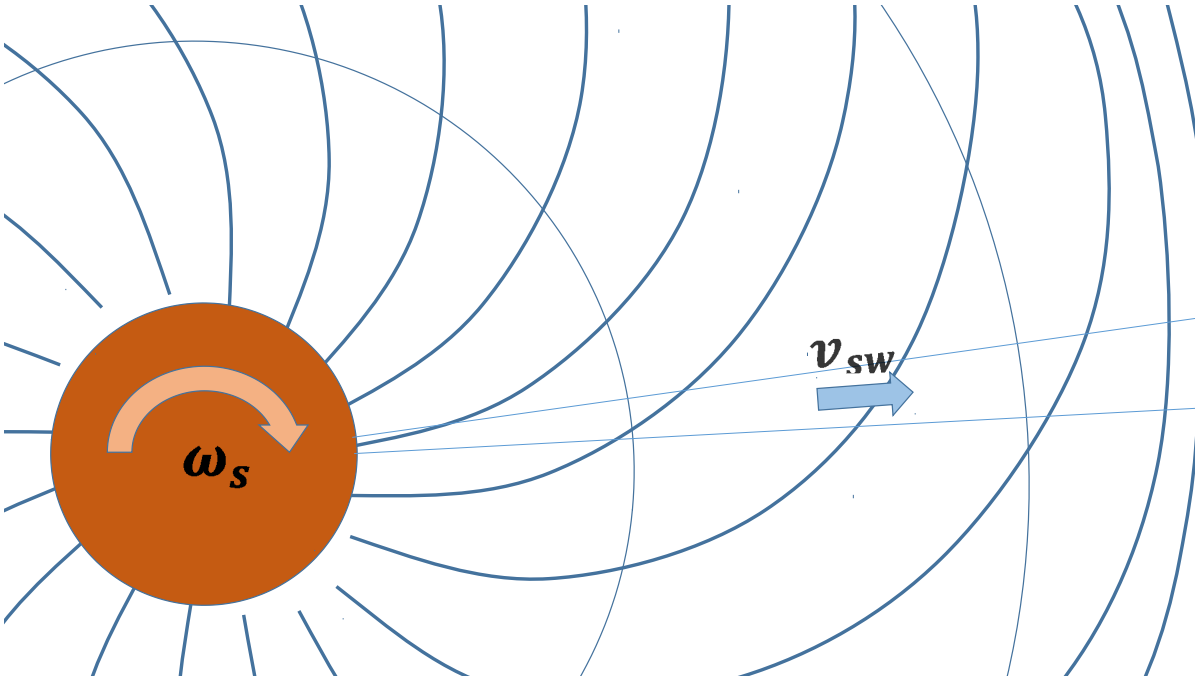

Figure 1: Schematic of the solar wind expansion and spiral magnetic field lines (blue) in the Sun's equatorial plane (if Earth were pictured in the diagram, the South pole would be visible). The sun is here pictured to rotate with angular frequency ω_s, while the solar wind expands isotropically with constant speed v_{sw}.

have similar temperatures (within an order of magnitude), the electrons naturally have a much lower mass. We will review the structure of the solar wind electron distribution $f_e(\mathbf{v})$, in preparation for later analysis, in detail in the next section.

1.4 Solar Wind Electron Populations—Core, Halo, and Strahl

The solar wind electron distribution $f_e(\mathbf{v})$ can be directly sampled by satellite instruments. Typical plasma densities are quite low (around 10 cm^{-3} at 1 AU), so it is in fact practical to develop detectors that measure the motion of particles by counting them one

at a time. This of course would be impossible to achieve in a laboratory plasma, where densities are many orders of magnitude higher (presenting, in many cases, a hazard to instruments are exposed to the hot gas). In this sense, the solar wind can be thought of as a unique laboratory for studying kinetic physics.

Direct measurements of the electron distribution will be presented in chapter 3 of this thesis, making use of an instrument known as an "electrostatic analyzer". The principle behind these devices is fairly simple: electrostatic analyzers are essentially a pair of closely-spaced, curved parallel plates that are set to have a voltage difference between them. Incoming particles (whose charge is of the correct sign), are guided in a circular path as they are accelerated by the electric field suffusing the space between the plates, and are counted at one end—but the particles can only be admitted if they have a particular energy, which is set by the plate voltage. Altering the plate voltage thus allows the spacecraft to sample different parts of phase space, and electrostatic analyzers are typically operated by stepping through voltages one at a time, until a broad range of energies are sampled. Particles with different incoming directions of motion may also be sampled, say, by utilizing the spin of the spacecraft (spacecraft are often spinning around some axis as a method of stabilization).

The distribution $f_e(\mathbf{v})$ measured in the solar wind is typically subdivided into 3 main populations: the core, halo, and strahl. Most of the electron density ($\gtrsim 90\%$) can be attributed to the Mawellian "core" of the distribution. At higher energies (e.g., between[3] approximately 10 eV and 1 keV at 1 AU) the distribution exhibits two "suprathermal"

[3]At even higher energies, the distribution exhibits another break, into an isotropic power-law tail known as the "superhalo" (42)

populations: a field-aligned beam known as the "strahl"[4], and a nearly-isotropic component known as the "halo" (e.g., 17; 55). Due to their relatively high energies, the strahl and halo electron populations are less affected by Coulomb collisions than the electron core, and particles in these populations can travel over heliospheric scales without coming into thermal equilibrium with the ambient plasma (e.g., 66). A schematic diagram, depicting these three electron populations, is shown in Figure 2. In the next section, we will explain the known features of the electron strahl in some detail, so let us first make a few remarks about the core and halo.

The core electrons are well-described by a Maxwellian distribution, with a few caveats. First, the core distribution drifts slightly relative to the ions in its field-parallel motion, so the peak of the core lags behind the ions by about 50 km/sec or so. This effect may be mediated by the solar wind collisionality (see, e.g., 56). The exact nature of this drift, particularly the shape of the electron distribution in this region of phase space ($\mathbf{v} \approx \mathbf{v_{sw}}$), is very difficult to measure due to the effect of *spacecraft charging* (e.g., 64): electrons are removed from the spacecraft surface as they are hit by photons from the sun (the photoelectric effect), and this loss of charge means that the spacecraft sits at some floating positive potential, typically around ∼2-3 eV. The measured electron distribution must then be corrected for this potential (which is not known a priori), which is on the order of the thermal energy of the core ($\sim$ 10 eV). The similarity of these energies presents a significant limitation on our understanding of the exact shape of core around this population's peak.

The halo distribution is usually modeled by a "kappa" distribution (e.g., 43). At very low energies, kappa distributions can be approximated as a Maxwellian in velocity

[4]The term "strahl" literally translates to "beam" in German.

space—however, this regime is not crucial to model because it is already occupied by the core distribution (which can be fit to a Maxwellian of its own). At high energies, kappa distributions approximate a power law (indexed by the value of a parameter κ). On average, the halo is found to be nearly isotropic in velocity space (54). However, it does exhibit temperature anisotropy at times, which may provide a source of free energy to fuel kinetic instabilities (e.g., 77). Not much about the origin of the halo distribution is known. Many theories posit that the halo may originate from the strahl particles (since these populations occupy similar energy regimes), say, through the action of some non-Coulomb scattering process that could isotropize the anti-sunward-moving strahl (e.g., 76).

1.4.1 The Strahl Electron Population

The strahl is a narrow, magnetic field-aligned population of suprathermal electrons (59) routinely observed in the ambient solar wind. The strahl is comprised of "thermal runaway" electrons (26). Because high energy particles are relatively insensitive to Coulomb collisions ($\nu_{coll} \sim v^{-3}$), electrons of sufficiently high energy can stream over large distances without coming into local thermal equilibrium (66). The strahl electrons generally move anti-sunward, because the relatively hot inner regions of the heliosphere act as a source of high-energy particles. However, in some instances—notably, during the transit of interplanetary coronal mass ejections—"counterstreaming" strahls (e.g., 23; 2), which are directed towards the sun, are also observed. When it is prominent, the strahl can provide the dominant contribution to the electron heat flux (55), which is an important source of heating of the solar wind during its non-adiabatic expansion (e.g.,

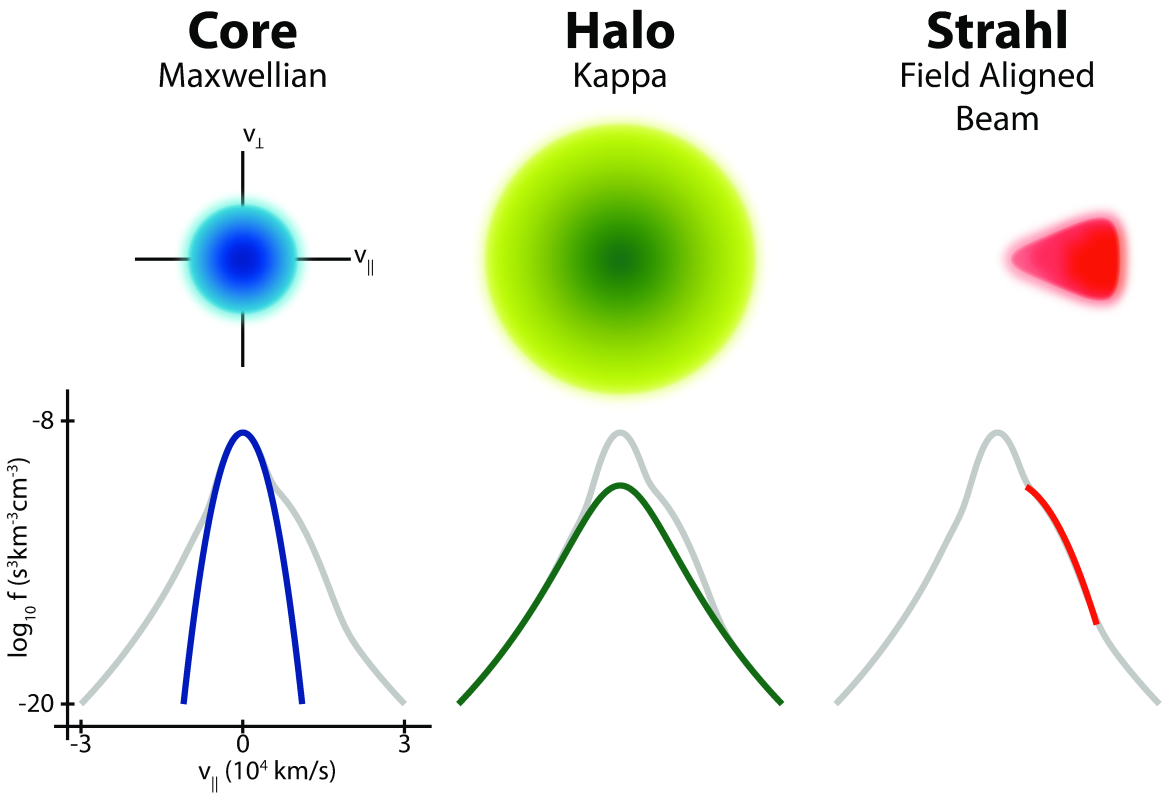

Figure 2: Schematic showing the core, halo, and strahl subpopulations of the electron distribution, and the regions of phase space they occupy (illustration courtesy of Marc Pulupa). The plots are shown in the solar wind frame (the peak of the ion distribution would appear at $\mathbf{v} \approx 0$ in this picture). The upper panels (roughly) show contours of the distribution in $v_\perp - v_\parallel$ space. The lower panels show field-parallel cuts ($v_\perp = 0$) of these subpopulations, in physical units, as they might typically appear at 1 AU. Note that the separation of the distribution into subpopulations is only an abstraction; a real observed distribution in the solar wind would appear as a superposition of these three populations.

78). The parallel electric current, on the other hand, is typically observed to be near zero regardless of the strahl amplitude (17).

The beam-like shape of the strahl in velocity space is believed to come from the competition of two physical processes: the mirror force and pitch angle scattering. The mirror force narrows this population, so that electron velocities run nearly parallel to the local magnetic field. The runaway electrons see a weakening field as they travel to larger heliocentric distances, which converts the particles' perpendicular velocity into parallel velocity. The observed strahls, however, are not as narrow as one would expect from conservation of the first adiabatic invariant ($\sim v_\perp^2/B$). It is therefore inferred that a scattering process provides some diffusion that broadens the distribution.

This pitch angle scattering is usually attributed to either Coulomb collisions or wave-particle interactions, and interest in the latter has been partially motivated by the perceived failure of the former. In particular, measurements conducted by (39) showed the strahl to be even broader than would be predicted by incorporating Coulomb collisions into exospheric theory, and it was suggested that a source of "anomalous diffusion" in the form of wave-particle interactions may be scattering the strahl particles.

Nonetheless, there is a wealth of evidence indicating that on average, characteristics of the strahl can be strongly correlated with the Coulomb collisionality of the background solar wind. We here refer to "collisionality" in terms of the Knudsen number $\gamma(x = const.) \propto T^2/n$, which parameterizes the ratio between advective and Coulomb scattering terms in the kinetic equation (see section 1.5 for more details). Prominent, narrow strahls have long been associated with the fast solar wind (e.g., 16; 55; 2). The fast wind is less collisional on average, since typically n is lower and T higher than in the slow wind. (49) specifically noted that prominent, narrow strahls can be seen when the

fast solar wind has very low density. (65) showed that the solar wind heat flux q, which comes from the skewness of $f(\mathbf{v})$ owing partially to the strahl, is correlated with γ. In (31), average field-parallel cuts of the electron distribution computed from Helios data were shown to vary with γ as predicted by a "self-similar" kinetic theory, with strahl amplitude increasing with γ. The fact that the solar wind data are so well-ordered by γ is a strong indication that Coulomb collisions play a central role in the physics that shapes the electron strahl.

Most wave-particle theories of strahl scattering have considered the effect of whistler waves (e.g., 82; 83; 61). These waves can resonate with the cyclotron motion of strahl electrons, scattering the particles and broadening their distribution. A variation on this mechanism was suggested by (67), in which anti-sunward halo particles *not* scattered by whistlers can be focused by the magnetic field into the strahl. Whistlers may be generated by the electron heat flux instability (e.g., 20; 22); this view has been supported by studies of whistler wave events (e.g, 84; 72). Whistlers may also be excited by the temperature anisotropy of the strahl population (e.g., 81), or may help comprise the small-scale interplanetary turbulence (e.g., 50; 6). Recently, the first direct observations of long-lived (lasting longer than 5 minutes) whistler waves were made (38), using data from the Cluster spacecraft mission. A subsequent study (35) demonstrated that the presence of whistler waves is correlated with broader strahl widths. However, the authors emphasized that whistler waves were detected infrequently by Cluster in the "pristine" (unperturbed by transient structures) fast wind: only 37 time intervals sustaining whistlers for a minute or longer were observed in a 10-year period. Looking beyond whistler waves, (53) proposed that strahl distributions focused by the mirror force should generate Langmuir oscillations. In their numerical simulations, quasilinear

oscillations continually scatter the strahl electrons, developing a steady state in which scattering balances magnetic focusing.

The detailed shape of the strahl distribution, which carries information about the physics that formed it, has been characterized in multiple observational studies. Using data from the Imp 6, 7, and 8 satellites, (16) found that the angular breadth of the strahl distribution decreases monotonically with energy in the fast wind. This is consistent with the predictions of Coulomb scattering models (see e.g., 61; 15) and some wave scattering models (e.g., 53). This picture is not always observed in the data, however; (2) reported that the strahl width can either increase or decrease with energy. Some instances where the strahl broadens with energy have been associated with rare transient events, such as solar electron bursts (13) and periods of increased wave activity (50). Counter to the notion that the magnetic field continuously focuses the strahl as the particles travel away from the sun, (27) found that the strahl width (at a given energy) actually increases with heliocentric distance r for Ulysses data $r > 1$ AU (see also (25)).

1.5 Spitzer Conductivity and the Knudsen Number

The strahl is of particular interest in solar wind studies because it introduces a field-parallel skewness in the distribution, that can significantly impact the so-called "heat flux" $\mathbf{q}$. The heat flux is computed from the 3^{rd} order moment of the distribution[5]:

$$\mathbf{q}(\mathbf{x}) = \frac{m_e}{2} \int v^2 \mathbf{v} f(\mathbf{x}, \mathbf{v}) d^3v, \tag{1.5}$$

[5]We will only consider electrons here, and drop the species subscript by default.

where m_e is the electron mass. Equation 1.5 describes the net flow of kinetic energy ($m_e v^2/2$) carried by electrons at a given location, in an inertial frame where the ions are at rest. The heat flux is of interest in fluid models of plasmas, as the divergence of this quantity appears in the time-dependent energy equation. As the distribution $f(\mathbf{x}, \mathbf{v})$ is not known a priori nor is it derivable from fluid theory, it is often convenient to develop a "closure"—an additional equation that prescribes the form of $\mathbf{q}$—in terms of other macroscopic plasma parameters (e.g., density, temperature).

In studies of the solar wind, the heat flux is often prescribed as a step in obtaining profiles for the solar wind speed (51; 7), as a player in the steady-state global energy balance (45), and as a source of free energy that drives instabilities (22).

Perhaps the most well-known closure in plasma physics is due to Spitzer & Härm (71), who solved the kinetic equation for $f(\mathbf{v})$ in the presence of a temperature gradient (in a plasma with constant density). They assumed that collisions between particles were frequent enough that $f(\mathbf{v})$ should be Maxwellian (a.k.a. Gaussian) to zeroth order, and solved for the first order perturbation $\delta f(\mathbf{v})$. Calculating the 3^{rd} order moment of this perturbation yielded an expression for the heat flux in the absence of a net electric current:

$$q_{sh} = -\kappa_{\parallel} \nabla_{\parallel} T. \tag{1.6}$$

Here $\kappa_{\parallel} \propto T^{5/2}$ is the thermal conductivity parallel to the magnetic field.

The Spitzer-Härm relation applies for collisional plasmas, where the collisional mean free path λ_{mfp} is sufficiently small. The degree of collisionality is parametrized by the temperature Knudsen number:

$$\gamma = -T^2(d\ln T/dx)/(2\pi e^4 \Lambda n) \sim \lambda_{mfp}/L_T, \tag{1.7}$$

where $L_T = |d\ln T/dx|^{-1}$ is the temperature scale height, Λ is the electron Coulomb logarithm, and x is the direction of the temperature variation. If $\gamma \ll 1$, the plasma is *collisional* and equation (1.6) applies, otherwise it is *weakly collisional* or *collisionless* and the description of $\mathbf{q}$ becomes more complicated. In particular, the Spitzer-Härm expansion is formally valid for $\gamma \lesssim 0.01$, while for larger values a population of "thermal runaway" electrons may contribute to the heat flux (e.g., 26; 36). Thus in a plasma with a temperature gradient, a population of electrons is locally detected that originated from distant, hotter regions. In the limiting case $\gamma \gtrsim 1$ the collisionless or "free-streaming" heat flux q_0 is given by the thermal energy density advected at the thermal speed, $q_0 \sim nv_{th}T$ (52; 26).

Recent measurements of the electron distribution function made by the Wind satellite's electrostatic analyzers EESA-L and EESA-H, presented by (4), have shed light on how Coulomb collisionality mediates the electron heat flux. The authors demonstrated in a broad statistical study of Wind data that the solar wind heat flux in fact scales with γ exactly as predicted by classical theory (71) in the collisional regime $\gamma \ll 1$; see Fig. 3, which is borrowed from the original paper. In the regime $\gamma \gtrsim 1$, the heat flux was observed to "saturate" at the collisionless value $q \sim nv_{th}T$. This saturation may owe to the onset of various plasma instabilities (e.g, 11). These results suggest that γ is the fundamental parameter needed to predict the heat flux and the electron distribution function in the weakly collisional solar wind—indeed, we will use γ as an ordering parameter, for the observations of $f_e(\mathbf{v})$ presented in section 3.5.

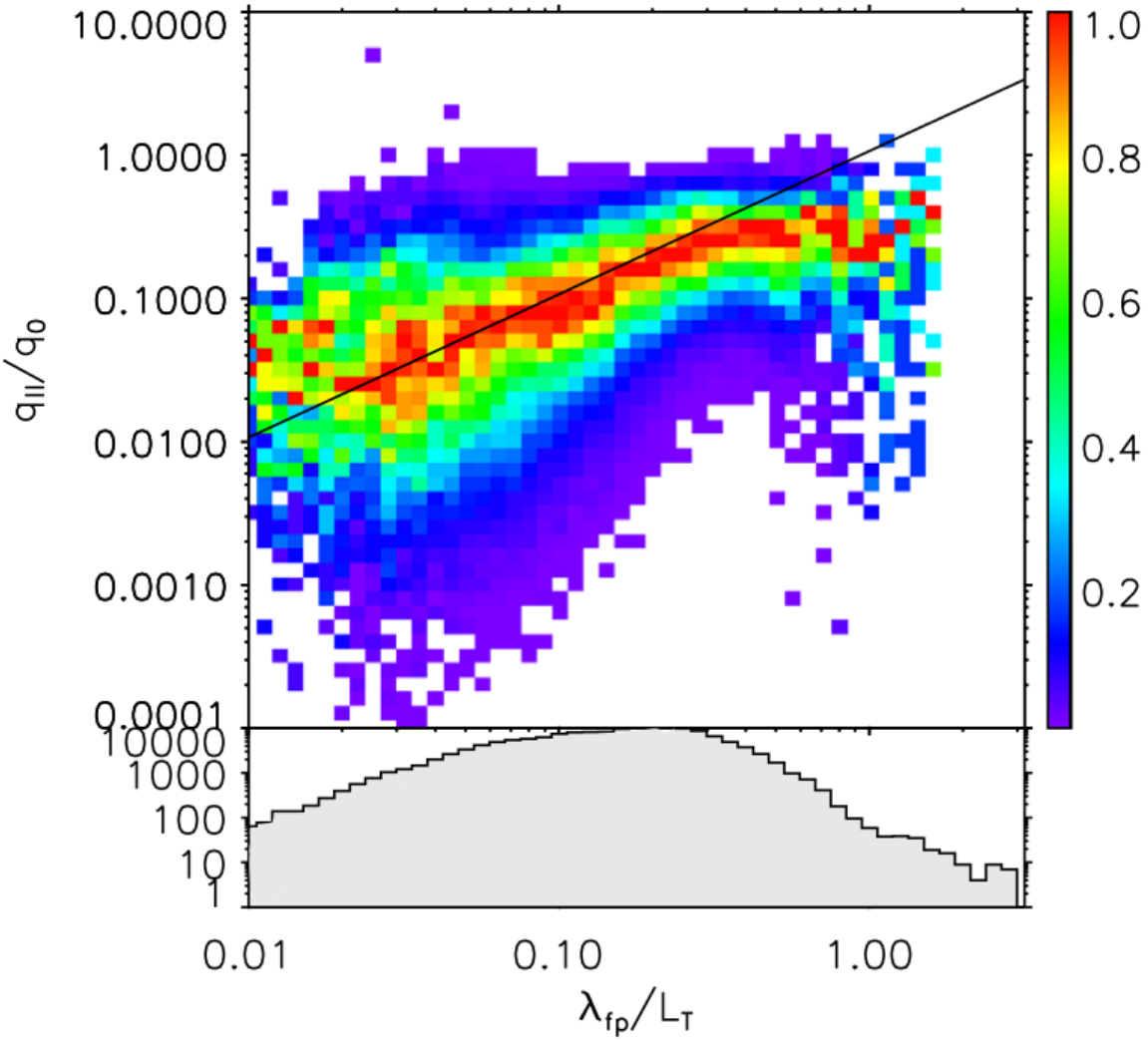

Figure 3: *Figure from (4)*—The field-parallel electron heat flux $q_{\|}$, normalized by the free-streaming heat flux $q_0 \sim nv_{th}T$, is plotted versus the temperature Knudsen number ($\gamma \sim \lambda_{mfp}/L_T$) as a joint normalized distribution. The plot displays about 4 years of slow solar wind data measured by Wind's 3DP instrument (an electrostatic analyzer). The black line shows the Spitzer-Härm relation, eq. (1.6), under the assumption that the temperature scales with distance as $T \propto r^{-2/7}$. The lower panel displays a histrogram of the total number of measurements at each Knudsen number. We see from the plot that the heat flux scales as predicted by Spitzer-Härm in the collisional regime $\gamma \ll 1$, and then approaches the free-streaming collisionless limit at lower collisionalities ($\gamma \sim 0.3$ in this plot).

Chapter 2

The Strahl—Asymptotic Solution

2.1 Introduction

The goal of this chapter is to develop an analytical model for the electron strahl population in the solar wind. The accurate analytic derivation of the full electron distribution function is a very complicated task since it requires one to solve the electron kinetic equation in an expanding background, subject to the boundary conditions at the base of the solar wind and at infinity. The analytical treatment of the strahl presented here was published in (32). Our model improves upon previous work on the subject (31; 33), by assuming the solar wind magnetic field evolves with distance according to the Parker spiral model. We additionally relax one of the assumptions made in those works, namely, that plasma parameters (e.g., density, temperature) should scale as power laws of the heliocentric distance. Rather, our solution for the strahl is cast in the most general terms, and such assumptions about solar wind structure may be applied afterwards (as we will do for the density, e.g., in section 3.4). Our model does not allow us to determine the solution uniquely, which reflects the fact that we do not solve a full boundary value problem, and, therefore, do not have enough information to fully describe the fast electrons that stream from the hot solar surface. We however demonstrate in chapter 3 that the remaining arbitrariness can be removed very efficiently by matching our analytic

solution with the observations.

2.2 Kinetic Equation and Solution

We will describe the electron distribution function[1] f in terms of the distance along a magnetic flux tube x, the velocity magnitude v, and cosine of the pitch angle μ:

$$\mu \equiv \hat{B} \cdot \mathbf{v}/v, \tag{2.1}$$

where the unit vector $\hat{B}$ points along the (Parker spiral) magnetic field, in the anti-sunward direction. The steady-state drift kinetic equation for the distribution function $f(v, \mu, x)$ then takes the following form (e.g., 37, see section C.1 of this thesis for detail):

$$\begin{aligned} \mu v \frac{\partial f}{\partial x} &- \frac{1}{2}\frac{d \ln B}{dx} v(1-\mu^2)\frac{\partial f}{\partial \mu} - \\ &- \frac{eE_{\parallel}}{m}\left[\frac{1-\mu^2}{v}\frac{\partial f}{\partial \mu} + \mu \frac{\partial f}{\partial v}\right] = \hat{C}(f), \end{aligned} \tag{2.2}$$

where $E_{\parallel}$ is the electric field parallel to the magnetic field line. In Equation (2.2) we have neglected the $\mathbf{E} \times \mathbf{B}$ drift. This equation describes the evolution of the (gyrotropic) electron distribution function for the electron population whose speed is much greater than the speed of the solar wind, $v \gg v_{sw}$. The magnetic fields lines are advected with the solar wind, and, therefore, the magnetic field can be assumed stationary for such electrons.[2] If we further assume that the energies of these electrons significantly exceed the thermal energy of the core particles, we may use the linearized form of the collision

[1] By default throughout the rest of this document, we will drop the subscript e when referring to the electron distribution.

[2] We treat the suprathermal electrons in an Eulerian frame.

integral for such electrons (e.g., 28, see section C.2 of this thesis for detail):

$$\hat{C}(f) = \frac{4\pi n e^4 \Lambda}{m_e^2}\left[\frac{\beta}{v^3}\frac{\partial}{\partial\mu}(1-\mu^2)\frac{\partial f}{\partial\mu} + \frac{1}{v^2}\frac{\partial f}{\partial v} + \frac{v_{th}^2}{2v^2}\left(-\frac{1}{v^2}\frac{\partial f}{\partial v} + \frac{1}{v}\frac{\partial^2 f}{\partial v^2}\right)\right], \tag{2.3}$$

where Λ is the Coulomb logarithm, $\beta = (1+Z_{eff})/2$, $Z_{eff} = \sum_i n_i Z_i^2/n_e$ is the effective ion charge, and $n \approx n_e$ and v_{th} are respectively the density and thermal speed of the core electron population. As is typical for the fast solar wind $v_{sw} > 550$ km/sec, we will assume that the abundance of He^{2+} is 5% of the H^+ abundance (85), and neglect the minor ions. For a quasi-neutral plasma with this composition, we find $Z_{eff} \approx 1.1$ and $\beta \approx 1.05$. The first term in the collision integral (2.3) describes the pitch-angle scattering of the fast electrons by the slow ions and electrons of the core population, while the remaining terms describe the energy exchange with the core electrons. If we are interested in the evolution of the fast electrons forming a narrow electron strahl with $v_\parallel \gg v_\perp$, one can demonstrate that the energy-exchange term is negligible in comparison to the scattering term. In what follows, we therefore keep only the first term in Eq. (2.3).

We simplify the analysis by introducing new variables, proportional to the electron energy, $E = v^2 + (2/m_e)e\phi(x)$, and the magnetic moment, $M = (1-\mu^2)v^2/B(x)$. In these expressions, $e < 0$ is the electron charge, and $\phi(x)$ is the electric potential measured with respect to $x = \infty$. In these variables, the drift-kinetic equation (2.2) for the electron distribution function $f(E, M, x)$ takes a simple form:

$$\frac{\partial f}{\partial x} = \frac{16\pi e^4 \Lambda \beta n(x)}{m_e^2 \mathcal{E}(E,x) B(x)}\frac{\partial}{\partial M} M\sqrt{1 - \frac{MB(x)}{\mathcal{E}(E,x)}}\frac{\partial f}{\partial M}, \tag{2.4}$$

where $\mathcal{E}(E,x) = E - (2/m_e)e\phi(x)$. For the runaway strahl electrons that we consider, $\mathcal{E} \approx E$, and since $v_\parallel \gg v_\perp$ we have $MB(x)/\mathcal{E}(E,x) \ll 1$. Equation (2.4) can then be

simplified as:

$$\frac{\partial f}{\partial x} = \frac{16\pi e^4 \Lambda \beta n(x)}{m_e^2 E B(x)} \frac{\partial}{\partial M} M \frac{\partial f}{\partial M}. \tag{2.5}$$

We can now introduce a new spatial variable y from the condition

$$dy = \left(\frac{16\pi e^4 \Lambda \beta}{m_e^2 E}\right) \left(\frac{n(x)}{B(x)}\right) dx, \tag{2.6}$$

where dx is the length element along the magnetic field line. We now notice that in ideal MHD, which is the basis for the Parker model, the vector $\mathbf{B}(x)/n(x)$ is frozen into the plasma flow, which means that this vector changes proportionally to the magnetic-line element dx when advected by the flow (e.g., 5; 73). This allows us to write:

$$dx/dx_{45} = \left(\frac{B(x)}{n(x)}\right) / \left(\frac{B(x_{45})}{n(x_{45})}\right), \tag{2.7}$$

where x_{45} is some fixed position, which we will choose, for definiteness, as the point where the magnetic field line is directed at 45° with respect to the radial direction.[3] For simplicity we will assume an axisymmetric Parker spiral model for the magnetic field. For the Parker spiral, the heliospheric distance r_{45} corresponding to the point x_{45} is given by the formula:

$$r_{45} = v_{sw}/\omega_s, \tag{2.8}$$

where ω_s is the model angular velocity of the sun and v_{sw} is the (constant) speed of the solar wind. In practice, the heliospheric distance r_{45} corresponding to the point x_{45} turns out to be approximately 1 AU.

[3]The frozen-in condition is elementarily related to flux conservation. Consider a radially expanding slab of solar wind plasma, with fixed thickness dr and small cross-sectional area $A(r)$. The frozen-flux condition dictates that $B(r)\hat{x} \cdot \hat{r} A(r) = const.$, while particle conservation within the expanding parcel can be expressed as $n(r)A(r)dr = const.$ Dividing the former equation by the latter, and noting that $\hat{x} \cdot \hat{r} dx = dr$, we find that the quantity $n(r)dx/B(r)$ is constant at all distances for the expanding parcel. In our azimuthally symmetric steady-state model, this identity holds throughout a single flux tube, which leads to Eq. (2.7).

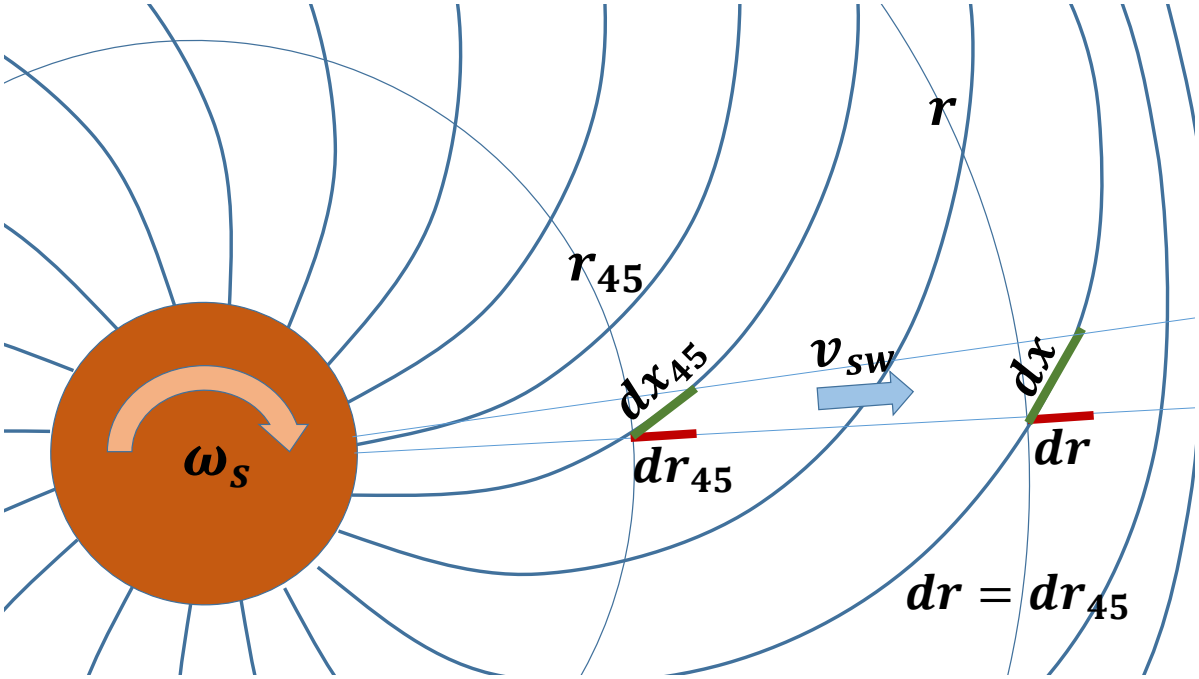

Figure 4: Sketch (drawn not to scale) of the magnetic field lines forming an azimuthally-symmetric Parker spiral. If the solar wind velocity, v_{sw}, is constant, the radial element dr does not change as the magnetic-field lines are advected with the solar wind, while the corresponding length element dx along a magnetic field line changes according to Eq. (2.9).

Since the lines are frozen into the radial solar-wind flow whose velocity, v_{sw}, is nearly constant, the radial displacement dr corresponding to the field-line element dx does not change as this element is advected with the flow, see Fig. (4). We therefore have $dx_{45} = dr_{45}\sqrt{2} = dr\sqrt{2}$. From Eq. (2.7) we therefore have

$$dx = dr\sqrt{2}\left(\frac{B(x)}{n(x)}\right) / \left(\frac{B(x_{45})}{n(x_{45})}\right), \tag{2.9}$$

which, after substitution into Eq. (2.6) gives

$$dy = \left(\frac{16\sqrt{2}\pi e^4 \Lambda \beta n(x_{45})}{m_e^2 E B(x_{45})}\right) dr. \tag{2.10}$$

Quite remarkably, we derive that the variable y is equal (up to a constant) to the heliospheric distance r. Parenthetically, we note that Eq. (2.10) would change if the solar wind velocity were not assumed to be constant.

Finally, conducting an additional change of variable $\zeta = \sqrt{M}$, we cast Eq. (2.5) in the form of a standard 2D radial diffusion equation describing $f(E, \zeta, y)$:

$$\frac{\partial f}{\partial y} = \frac{1}{4}\frac{1}{\zeta}\frac{\partial}{\partial \zeta}\zeta\frac{\partial f}{\partial \zeta}. \tag{2.11}$$

This equation can be solved if the distribution of the strahl electrons is known at some initial position y_{in}. We assume that this distribution is narrow, that is, concentrated at $v_{\parallel} \gg v_{\perp}$. Then at larger distances $y \gg y_{in}$ it can be approximated by the standard solution of the 2D diffusion equation:

$$f(E, M, y) = \frac{C(E)}{y}\exp\left(-\frac{\zeta^2}{y}\right) = \frac{C(E)}{y}\exp\left(-\frac{M}{y}\right), \tag{2.12}$$

where $C(E)$ is an arbitrary function that may be related to the distribution of fast electrons at the base of the solar wind. This supports similar conclusions drawn by, e.g., (69), about the coronal origins of the strahl electrons. We need not relate function

$C(E)$ to the thermal distribution of the core electrons at a given distance, a priori, since the strahl is not in thermal equilibrium with them.

In the Parker-spiral model, the magnetic field strength changes with the heliospheric distance as $B(r) = B(r_{45})(r_{45}/r)\sqrt{1 + r_{45}^2/r^2}/\sqrt{2}$, where r_{45} is the heliospheric distance corresponding to the field-line position x_{45}, as described by Eq. (2.8). We can now re-write the obtained solution (2.12) for the electron-strahl distribution function (again assuming $E \approx v^2$) using the variables v, μ, r:

$$f(v, \mu, r) = \frac{C(v^2)}{r} \exp\left\{ -\frac{v^4(1-\mu^2)}{\sqrt{1 + r_{45}^2/r^2}} \left(\frac{m_e^2}{16\pi n_{45} r_{45} e^4 \Lambda \beta} \right) \right\}, \tag{2.13}$$

where we have denoted $n_{45} = n(r_{45})$. This completes our solution for the strahl component of the electron distribution function. Except for the undetermined isotropic velocity function $C(v^2)$, this solution does not contain free parameters.

The width of the obtained strahl distribution function at a given energy can be found directly from this solution. From the exponential factor of Eq. (2.13), we find the so-called strahl full width at half maximum, θ_{FWHM}:[4]

$$\theta_{FWHM} = 2 \sin^{-1} \left\{ \frac{16\pi n_{45} r_{45} e^4 \Lambda \beta \sqrt{1 + r_{45}^2/r^2} \ln(2)}{m_e^2 v^4} \right\}^{1/2}. \tag{2.14}$$

Expressions (2.13) and (2.14) are the main predictions of our theory for the electron strahl.

A simpler expression can be derived using the small angle approximation $\sin^{-1}\theta \approx \theta$. By assuming the typical values for the parameters[5] $\Lambda \approx 30$, $\beta \approx 1.05$, and $r_{45} \approx 1$ AU,

[4]The full width at half maximum is twice as large as the corresponding half-maximum pitch angle θ.

[5]The Coulomb logarithm is estimated as $\Lambda \approx 24 - \ln(n^{1/2}/T)$, where n (cm^{-3}) is the density of the particles and T (eV) is their temperature (34). For the estimate, one needs to consider the particles whose thermal velocity is larger than the relative velocity between the scattered (strahl) and scattering (core) particles. We, therefore, substitute here the temperature of the strahl and halo particles, $T \sim 100$ eV, and their combined density $n \sim 0.5$ cm^{-3}, which is about $5 - 10\%$ of the core density (e.g., 76).

Eq. (2.14) can be approximated as:

$$\theta_{FWHM} \approx 24^\circ \left(\frac{K}{100\text{ eV}}\right)^{-1} \left(\frac{n_{45}}{5\text{ cm}^{-3}}\right)^{1/2} \left(1+\frac{r_{45}^2}{r^2}\right)^{1/4}, \tag{2.15}$$

where the variable K denotes the kinetic energy:

$$K \equiv \frac{m_e v^2}{2}. \tag{2.16}$$

As will be discussed in more detail in chapter 3, we note that the strahl width predicted by Eq. 2.15 varies as the square root of the density, and varies inversely with the energy.

Two important observations should be made about this solution. First, the width of the electron strahl is independent of the overall strength of the magnetic field, as e.g., the term $B(r_{45})$ is absent from Eq. (2.14). The width only depends on the way the magnetic field varies with distance in the Parker spiral. Second, at lower heliospheric distances, $r^2 \ll r_{45}^2$ the focusing effects dominate and the width of the strahl decreases with the distance. At higher distances, $r^2 \gg r_{45}^2$, however, the strahl width *saturates* and becomes independent of distance. The angular width of the saturated strahl, $\theta_{FWHM,s}$, at these distances then follows immediately from Eq. 2.15:

$$\theta_{FWHM,s} \approx 24^\circ \left(\frac{K}{100\text{ eV}}\right)^{-1} \left(\frac{n_{45}}{5\text{ cm}^{-3}}\right)^{1/2}. \tag{2.17}$$

Equation 2.17 may be interpreted to mean, for example, that the angular width of the 100 eV strahl electrons will saturate at a value on the order of 24° in the outer heliosphere.

The saturation of the strahl width may seem counterintuitive if one considers that at $r^2 \gg r_{45}^2$ the magnetic-field strength still declines rather rapidly with the heliospheric

distance, with the scaling $B(r) \propto 1/r$, and the magnetic focusing effects may be expected to dominate in a nearly collisionless plasma. The resolution to this paradox is that for $r^2 \gg r_{45}^2$ the magnetic field lines are nearly azimuthal in the Parker spiral, in which case the magnetic-field strength declines rather slowly *along* the magnetic field line. An electron following a magnetic field line has to travel an increasingly large distance along a rather slowly declining magnetic field, before considerable focusing can take place. This enhances the effects of collisional broadening relative to the effects of magnetic focusing, leading to the establishment of a universal strahl width in the regime $r^2 \gg r_{45}^2$, as seen from Eq. (2.14).

Our strahl model takes into account the defocusing effects caused only by electron Coulomb collisions. Our results thus present a lower boundary on the width of the strahl. They are however in good agreement with the set of observational data at 1 AU that we analyze in the next chapter. In chapter 3, we will show that our formula (2.14) underestimates the width of the strahl in those measurements by only about $15 - 20\%$, indicating that Coulomb collisions provide a dominant contribution to the strahl broadening. In practice, the strahl electrons may also be scattered by plasma turbulence that is ubiquitous in the solar wind, which could further enhance the strahl broadening.

Chapter 3

Comparison with Wind Data

3.1 Introduction

In this chapter, we will test our theoretical predictions for the shape of the strahl distribution, which were developed in chapter 2. The material presented here is adapted from our published work (33; 32), and is augmented by additional (or updated) figures.

To test our theory, we examine high resolution measurements of the strahl distribution made by the Wind satellite, whose Solar Wind Experiment (SWE) had an electrostatic analyzer dedicated to measuring the strahl distribution (48). Wind's strahl detector had very fine ($\sim$4.5°) angular resolution, making it ideal for measuring the shape of the strahl distribution. Following previous observational papers (e.g. 49), we will characterize the breadth of the distribution in terms of the angular full width at half maximum (FWHM). We will demonstrate in section 3.4 that the strahl widths are accurately described by our theory, as it correctly predicts how the width decreases with particle energy and increases with background density.

The angular breadth of the solar wind strahl distribution has been the object of study for some time. As mentioned in section 1.4.1, a seminal work on this topic (39) developed a model of strahl broadening based solely on Coulomb collisions. Their theoretical approach was quite different from that presented in chapter 2 of this thesis; for instance,

the authors of that work did not base their derivation not on the drift kinetic equation, nor did they account for the Parker spiral structure of the magnetic field (instead assuming $B(r) \propto r^{-2}$ throughout the heliosphere). The observational data presented in this chapter will lead us to a different conclusion than that of (39), in that we will find the strahl-widths to in fact be well-described by our collisional model. We therefore must differ with their inference that "another mechanism, for instance wave-particle interactions, scatter(s) these electrons". At least for the energy regimes investigated here[1], our observations indicate that Coulomb collisions are the primary source of diffusion for the strahl electrons.

It bears mentioning that prior to the publishing of our recent works, the SWE strahl detector data had fallen into disuse. Besides a few publications dating to the late 1990s and early 2000s, this data set was virtually absent from the solar wind literature. It required significant effort to revitalize this data set—to read the raw data files, apply the appropriate calibrations, and to remove experimental artifacts. This was made possible in large part due to help from current and past members of the Wind team at NASA's Goddard Space Flight Center (see the "Acknowledgments" section). For those interested, the strahl detector data have recently been made available for download via NASA/GSFC's Space Physics Data Facility's CDAWeb service.

[1]Even with the high angular resolution of the SWE strahl detector, at very high energies our model predicts that the strahl should be even narrower than the detector can resolve. We will thus limit our attempts to match our model with the data, to cases where observed strahl width is broader than the minimum detector resolution, i.e. when the strahl width is $\gtrsim 10°$.

3.2 SWE Strahl Detector

The Wind satellite's strahl detector is a toroidal electrostatic analyzer (48), which directly sampled the solar wind electron velocity distribution function (eVDF) at a heliocentric distance r =1 AU. The instrument's 12 anodes are set in a vertical pattern in a plane that contains the spacecraft spin axis, spanning a field of view $\pm 28^\circ$ centered around the ecliptic. Wind's spin axis is set at a right angle with the ecliptic plane, allowing different azimuthal angles to be sampled as the spacecraft spins (3 sec spin period). These azimuthal bins have a fixed separation of 3.53°. Each strahl distribution measured by the spacecraft consists of a 14x12 angular grid of electron counts, that was measured at a fixed energy during a single spacecraft spin. Counts can be converted into physical units of $f(\mathbf{v})$ (e.g., $\mathrm{cm}^{-6}\mathrm{s}^3$) in the standard fashion by accounting for the detector efficiency and geometric factor[2]. Accompanying each strahl measurement is an analogous 14x12 measurement of the "antistrahl", made at a clock angle 180° with respect to the strahl measurement. The detector voltage was set to a different value each spin, so that 32 energies from 19.34 to 1238 eV would be sampled in as many rotations.

In the original mode of operation, each measurement grid was centered on the nominal average Parker spiral (in the ecliptic plane, 45° offset from the radial direction $\hat{r}$). In practice, however, the local magnetic field only fell within the field of view of the detector about half the time. This prompted a revision of the instrument software in February 1999 (49), which matched the clock angle of the strahl measurement with the

[2]The discrete number of particles counted with given velocity $\mathbf{v}$, which we here denote as C_v, is related to the observed magnitude of the distribution at that velocity $f(\mathbf{v})$. The quantities are related via the proportionality $f(\mathbf{v}) \propto C_v \times v^{-4}$. The "geometric factor" is a constant factor that depends on the geometry of the electrostatic analyzer (e.g. its physical size and admittance angle), that sets this proportionality. Note: the factor of 4 in the speed exponent comes from the fact that the phase space volume sampled by the detector scales with the incoming particle speed as v^3, while rate at which particles impact the detector should also of course scale with their speed, v.

instantaneous measurement of the magnetic field provided by Wind's Magnetic Field Investigation (MFI).

Our data set ranges from January 1, 1995 to May 30, 2001, which nearly covers the operational lifetime of the strahl instrument. The strahl detector was reconfigured shortly after this period to serve as a replacement for SWE's Vector Electron/Ion Spectrometer (VEIS), whose power supply had recently failed.

3.3 Strahl Data

The data studied here are derived primarily from Wind's SWE strahl detector, supplemented by plasma data from SWE/VEIS and vector magnetic field data from MFI (48; 40). The background electron density n is taken from the VEIS measurement of proton density n_p, which is a reasonable estimate for the quasineutral, proton-dominated solar wind. This is more reliable than direct measurement of n with the electron instrument since measurements of the proton distribution are less susceptible to spacecraft charging effects (see, e.g., 14; 55). The temperature is calculated from the second-order moment of the eVDF measured by VEIS. We note that this measurement overestimates the core temperature T by a small factor (10-20%), since the suprathermal populations are included in the calculation. Plasma parameters (which are used to calculate ξ, γ, etc.) from other instruments are associated with each strahl measurement by matching to the nearest measurement time. If plasma data are not available within 5 minutes of the strahl measurement, then the data are excluded from our analysis. We also exclude data for which the $\hat{B}$ direction, as measured by the MFI instrument, is outside of the strahl detector's field of view.

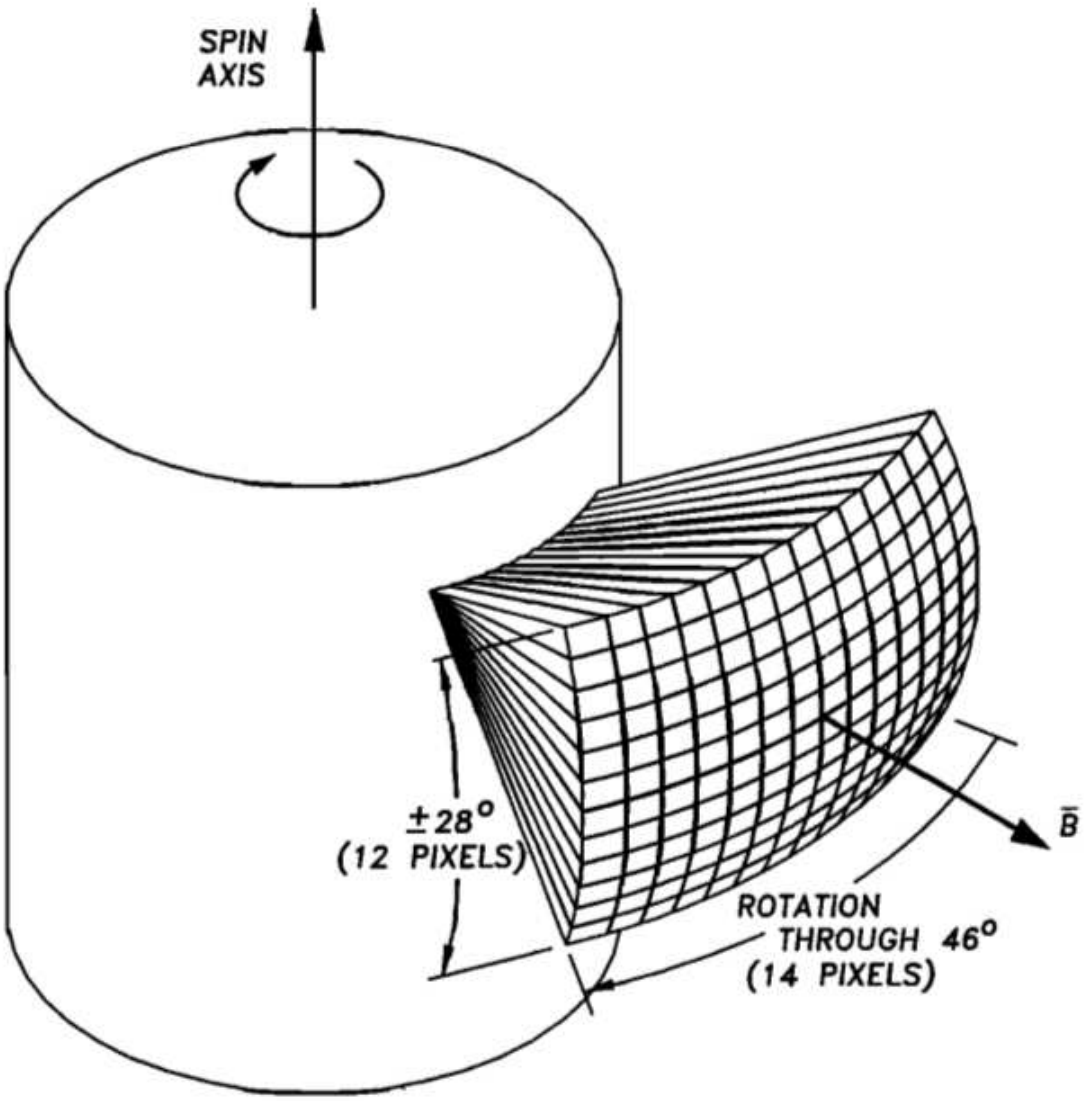

Figure 5: Schematic of the SWE strahl detectors 14×12 angular field of view, from (49).

Each measurement made by the SWE strahl detector is a composition of signals from the strahl, halo, and (at low energies) core components of the electron distribution (e.g., 55). In order to conduct a statistical study of the fast wind strahl, we developed an automated procedure for isolating the strahl signal from the background formed by the other populations. The procedure is as follows:

1. *Find the strahl*—For each 14x12 strahl distribution f_s (measured at a single energy), find the bin where the distribution is at a maximum, and designate the nominal velocity direction of electrons measured in that bin as the "peak direction".

2. *Remove the halo*—Let the maxima of the measured strahl and associated anti-strahl distributions be designated $f_{s,max}$, $f_{a,max}$ respectively. Zero out (ignore in future analysis) the bins of the strahl distribution where the criterion $f_s < Max\{f_{a,max} \times 3/2, f_{s,max}/5\}$ is satisfied.

3. *Clean up residual noise*—Calculate the pitch angle θ, relative to the peak direction, of every bin in the 14x12 grid. Find the minimum pitch angle $\theta_{min} = Min\{\theta\}$ among the bins zeroed out in the previous step. Zero out every bin in the strahl distribution f_s that satisfies $\theta > \theta_{min}$. From this point forward, "f_s" will refer to the cleaned strahl distribution resulting from the above procedure.

This cleaning procedure leads to a very clearly defined strahl, an example of which is shown in figure 6.

For strahl distributions measured after the February 1999 software revision, anomalously high count rates were observed when the sun was in the detector's view (R. J. Fitzenreiter 2016, personal communication). These spurious counts were caused by photoelectrons, and should be removed from our analysis. As a simple correction, we zero out (prior to step "Find the strahl" above) data from all 12 anodes at a given azimuthal angle, if one of these anodes pointed within 10° of the sun's position.

3.4 Measurement of the Strahl Width

We now compare the SWE strahl detector data with our model. We will only consider the fast solar wind, i.e. when the solar wind bulk velocity v_{sw} exceeded 550 km/sec. The strahl detector measures each distribution at fixed energy K and position $r = 1\text{AU}$. The measurements take place over an interval of a few seconds, so that the bulk density n and speed v_{sw} (from which n_{45} and r_{45} are respectively inferred) can be taken as constant as well. For the small angles ($\theta \approx 0$, $\mu \approx 1$) relevant to the strahl, we can approximate $(1-\mu^2) \approx 2(1-\mu)$ via the Taylor expansion. This implies that the measured angular distribution function $f(\mu)$ should fall off exponentially with $(1-\mu)$, as it follows from equation 2.13:

$$f(\mu) \propto \exp\{-A(r, r_{45}) n^{-1} K^2 (1-\mu)\}. \tag{3.1}$$

The form of $A(r, r_{45})$, a shorthand that we use here for simplicity, can be found immediately from equation 2.13:

$$A(r, r_{45}) \equiv \left\{ 2\pi r e^4 \Lambda \beta \sqrt{\left(\frac{r}{r_{45}}\right)^2 + 1} \right\}^{-1}. \tag{3.2}$$

In obtaining equation 3.2, as throughout this chapter, we assumed that the density n

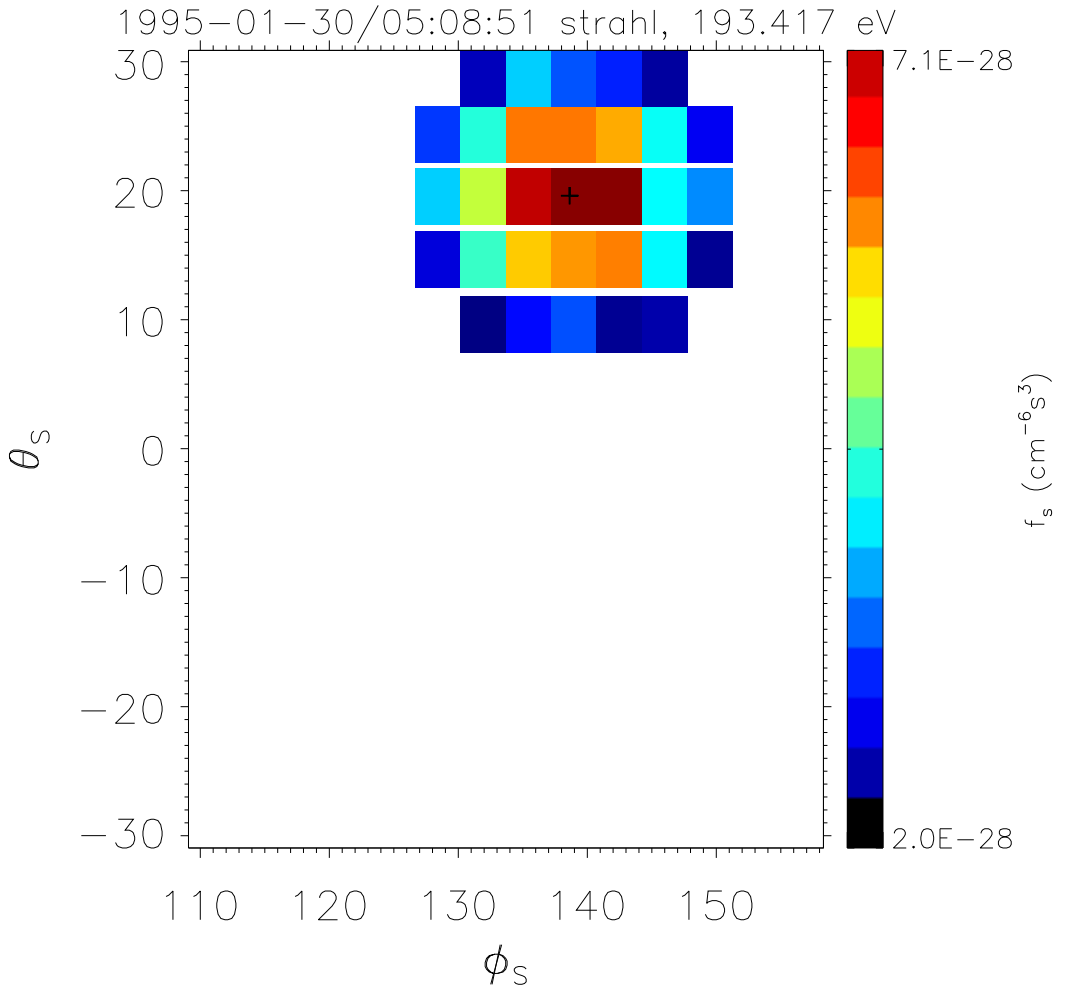

Figure 6: An example strahl spectrum f_s (linear z-axis scale), after applying an automated procedure for removing the halo population. This plot can be compared with figure 3, (18), which shows the "raw" spectrum. The variables θ_S, ϕ_S are spherical (GSE) coordinates that describe the velocity direction of the measured electrons. The angle $\theta_S = 0$ corresponds with the ecliptic. Note that the detector's 12 anodes are not evenly spaced in θ_S. The magnetic field direction $\hat{B}$ is determined through the process of nonlinear fitting described in section 3.4, and is shown in this example by a "+" symbol.

varies with heliocentric distance as $n(r) \propto r^{-2}$. This satisfies the continuity equation of fluid mechanics in a constant-speed solar wind.

Let us express equation 3.1 in terms of the pitch angle with respect to the magnetic field, $\theta \equiv \cos^{-1}(\mu)$. Still assuming small angles, we can approximate $\mu \approx 1 - \theta^2/2$, implying f should fall off as a Gaussian with θ:

$$f(\theta) \sim \exp\left\{\frac{-A(r, r_{45})K^2\theta^2}{2n}\right\}. \tag{3.3}$$

This prediction agrees with previous attempts to model the strahl; functions of the form $f(\theta) \propto \exp(-c\theta^2)$, where c is some constant, have been used to fit measured strahl distributions at fixed energy (27; 2). The exact expression for the full width at half maximum of this nearly-Gaussian strahl, θ_{FWHM}, is given already by equation 2.14. An approximate expression is given in equation 2.15. From this latter equation we obtain the following scaling relations for fixed r and $r_{45}(v_{sw})$:

i For given n, $\theta_{FWHM} \propto K^{-1}$

ii For given K, $\theta_{FWHM} \propto \sqrt{n}$

The local quantities n and K, which determine the breadth of the strahl in our model, are known to high accuracy. Measurements of these parameters have relative errors 10% and 3% for n and K, respectively (48). We note also that our prediction for θ_{FWHM} is independent of T.

To test our prediction for θ_{FWHM}, we must first calculate the observed strahl widths from the angular distributions. We fit each strahl distribution f_s to our model (3.1). Let us define the following variables:

$$z \equiv \ln(f_s/f_{s,max}) \tag{3.4}$$

$$y \equiv (1-\mu) \tag{3.5}$$

$$m \equiv -A(r, r_{45})n^{-1}K^2 \tag{3.6}$$

and write equation 3.1 as:

$$z(y) = my + \mathcal{Z}, \tag{3.7}$$

where m and $\mathcal{Z}$ are constants.

Since our model (3.7) is linear when expressed in these variables, it would seem natural to employ the weighted ordinary least squares (OLS) technique to find the parameters m, $\mathcal{Z}$ for each distribution. This could be accomplished by fitting to the data $\overline{z}_i$ comprising the distribution, which is measured at independent coordinates y_i ("i" indexes the bins of f_s). However, it turns out that there is considerable error in our determination of the magnetic field direction $\hat{B}$ which must be corrected for. If our measurement of $\hat{B}$ (as determined by the MFI instrument) is off by even a few degrees, errors in y_i will lead to significant inaccuracies in the determination of the strahl width. This effect is most problematic when the angular error of the $\hat{B}$ direction is on the order of θ_{FWHM}, which can occur for narrow strahls.

We therefore conduct a weighted *nonlinear* least squares fit to the distribution function (z), in which the direction $\hat{B}$ is determined by the fitting procedure. Our fits are generated using the MPFIT software (44), which implements the Levenberg-Marquardt algorithm. We fit to the (2D) model function:

$$z(\phi_S, \theta_S) = my(\phi_S, \theta_S; \phi_B, \theta_B) + \mathcal{Z}. \tag{3.8}$$

Here we introduced the function $y(\phi, \theta; \phi', \theta')$,

$$y(\phi, \theta; \phi', \theta') = 1 - \hat{U}(\phi, \theta) \cdot \hat{U}(\phi', \theta'), \tag{3.9}$$

and $\hat{U}(\phi, \theta)$ is a function that produces a unit vector pointing in the direction specified by ϕ, θ (azimuth and altitude, in GSE coordinates).

Equation (3.8) is the same as the OLS function (3.7) described above, with some nuance. Now there are two independent coordinates, ϕ_S and θ_S, which represent azimuth and altitude in spherical (GSE) coordinates. The model (eq. 3.8) has four fit parameters: m, ϕ_B, θ_B, and $\mathcal{Z}$. The parameters m and $\mathcal{Z}$ are as above. The direction $\hat{B}$ is specified by the fit parameters ϕ_B and θ_B, i.e. $\hat{B} = \hat{U}(\phi_B, \theta_B)$. The y_i data are interpreted as above, but now $y_i = 1 - \mu_i$ depends on the ϕ_i, θ_i identified with the nominal velocity direction of electrons measured in the i^{th} bin, as well as on the fit parameters ϕ_B and θ_B. Namely, $y_i = y(\phi_i, \theta_i; \phi_B, \theta_B)$.

Our weighted fit requires an estimate of the standard error of the $\overline{z}_i$ measurements, which we denote as σ_i. This can be estimated by assuming the strahl detector obeys Poisson ("counting") statistics. We assume the raw number of counts ζ_i registered by the detector in the i^{th} bin is sufficiently large, so that we can approximate the error of ζ_i as Gaussian-distributed, with standard deviation $\sqrt{\zeta_i}$. Then, we find $\sigma_i \approx 1/\sqrt{\zeta_i}$ from straightforward error propagation (noting f_s is proportional to counts).

Our fitting procedure minimizes the chi-squared statistic:

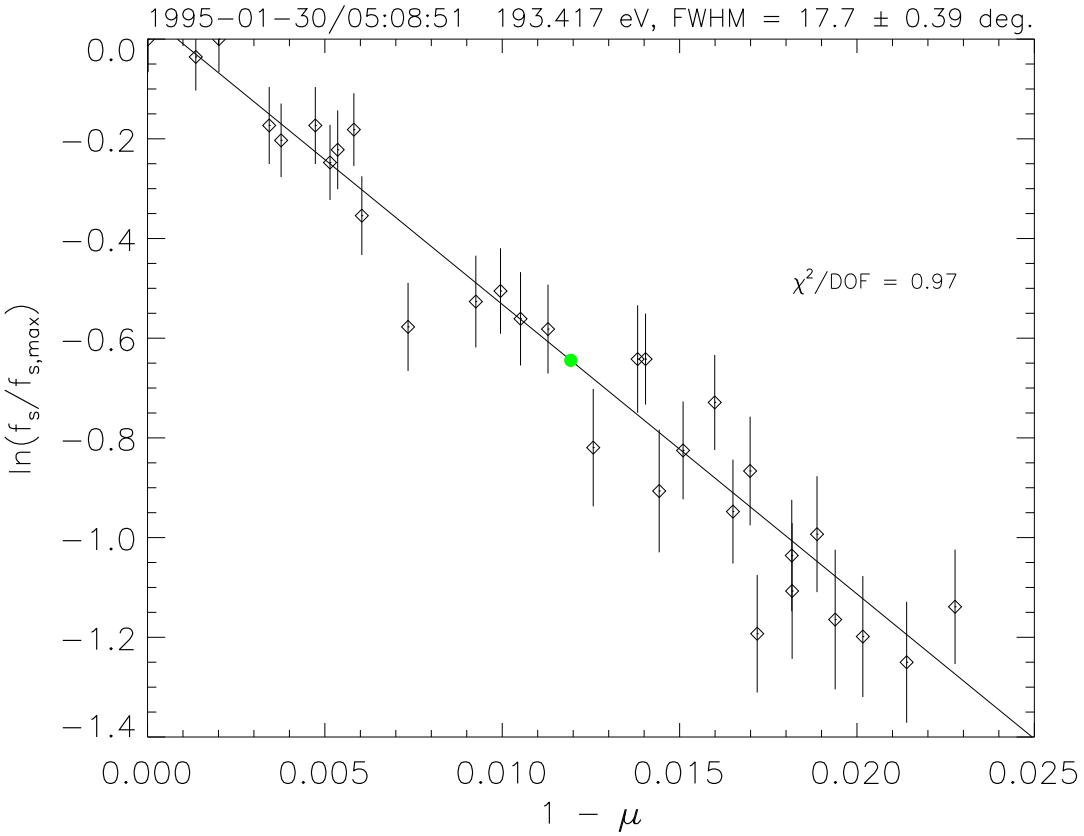

Figure 7: An illustration of our fitting method: the 2D angular distribution f_s (from Figure 6) is displayed above as what we may loosely call a "pitch angle" distribution $z(y)$, where $y = (1-\mu)$ and $z = \ln(f_s/f_{s,max})$. The data in the vicinity of the strahl peak is fit to the function $z = my + \mathcal{Z}$, see Eqs. 3.1, 3.7. Our method of fitting, a nonlinear least squares fit that allows the $\hat{B}$ direction to vary, is a weighted fit that accounts for the uncertainties σ_i of the $\overline{z}_i$ measurements. The estimated uncertainties σ_i are shown above as error bars. The full width at half-maximum of the strahl (green dot), θ_{FWHM}, is calculated from m according to equation 3.12.

$$\chi^2 = \sum_{i=1}^{N} (z_i - \overline{z}_i)^2 / \sigma_i^2. \tag{3.10}$$

Here, $(z_i - \overline{z}_i)$ represents the difference between our model function (z) and the data $(\overline{z})$, for the i^{th} bin of the distribution. N is the number of non-zero data points[3] in the 12×14 strahl distribution f_s; we only conduct a fit if there are at least 6 points left after applying the cleaning procedure (section 3.3), so $6 \leq N \leq 168$. Figure 7 shows an example of our fitting procedure, applied to the data appearing in figure 6.

The normalized chi-squared statistic χ^2/DOF can be used to test goodness of fit. Here $DOF = N-4$ represents the degrees of freedom of our 4-parameter model function (3.8). If our model accurately describes the data and if the errors σ_i are properly characterized, the quantity χ^2 is predicted (86) to have the following statistical distribution $P(\chi^2)$:

$$P(\chi^2) = \frac{(\chi^2)^{(DOF-2)} \exp(-\chi^2/2)}{2^{(DOF/2)}\Gamma(DOF/2)}, \tag{3.11}$$

where Γ denotes the gamma function. According to (3.11), the average ("expected") value of χ^2 is equal to the number of degrees of freedom, i.e. $\int_0^\infty P(\chi^2)\chi^2 d(\chi^2) = DOF$. We may therefore use the quantity χ^2/DOF, calculated for each of our fits to the strahl angular spectra, as a test of goodness of fit. For each of our fits to the fast wind data, we calculate χ^2/DOF, according to Eq. (3.11). We then calculate the average value of this quantity, $\langle\chi^2\rangle$, among the >100,000 fits in our analysis. We find $\langle\chi^2/DOF\rangle = 1.12$ for our data set. To calculate this average, we excluded outlier fits for which $\chi^2/DOF > 10$, which constituted only 1% of the completed fits. Since $\langle\chi^2/DOF\rangle \approx 1$, we conclude that equation 3.1 accurately describes the strahl data.

[3]By inspection, we see that $N = 31$ for the example spectrum plotted in Fig. 6.

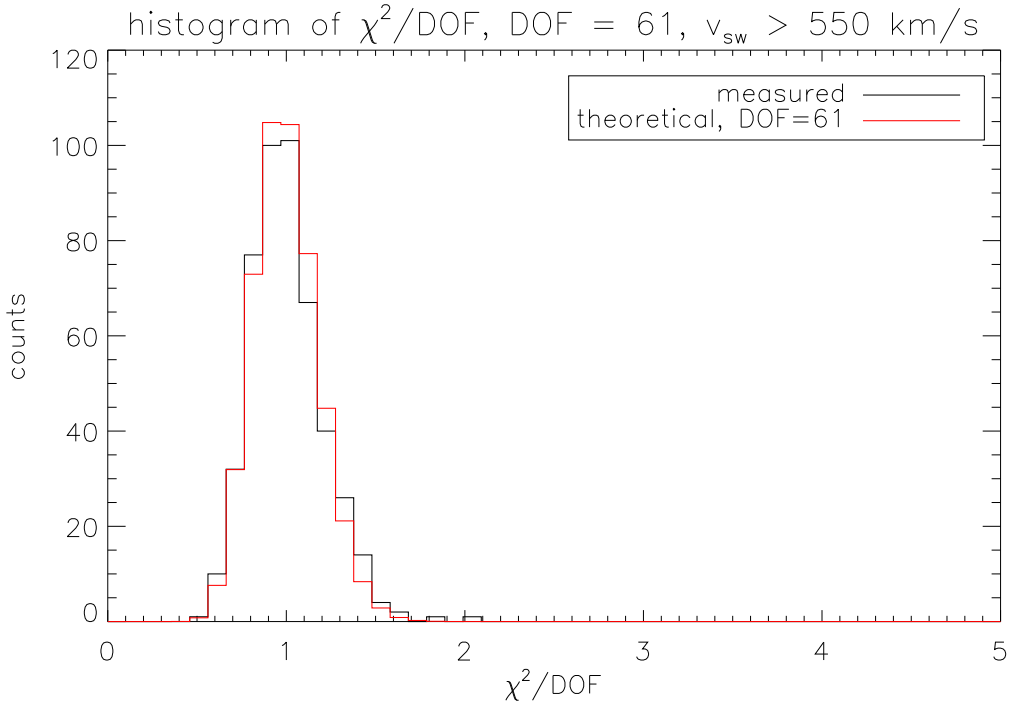

Figure 8: Comparison of calculated χ^2/DOF of fast wind data (black) with the expected (red) statistical distribution $P(\chi^2)$, see Eq. (3.11) and the following discussion. We present this plot to establish the goodness of fit of our model function, Eq. 3.8. To make this plot, we computed a histogram of values of χ^2/DOF with a fixed bin width $\Delta(\chi^2/DOF) \approx 0.1$, for our fits to the cleaned strahl spectra with $N = 65$ fit points ($DOF = 61$).

We may conduct a more detailed analysis of goodness-of-fit, by comparing the observed distribution of χ^2/DOF among our fits with the theoretical distribution (3.11). In Fig. (8) we plot a histogram of the obtained values of χ^2/DOF (black line), for our fits to the cleaned strahl spectra that each contained $N = 65$ data points ($DOF = 61$). This histogram has a fixed bin width $\Delta(\chi^2/DOF) \approx 0.1$. For comparison, we plot as a histogram the theoretical curve χ^2/DOF (red line), which we obtain from Eq. (3.11), setting $DOF = 61$. For the theoretical curve, we predict the number of "counts" that would fall into a bin of width $\Delta(\chi^2/DOF)$ from Eq. 3.11; first, we integrate this equation over the corresponding interval of width $\Delta\chi^2$ (which yields the relative probability that a measurement will fall in this interval), and then multiply the result by the total number of strahl spectra with $N = 65$ points. We observe that our synthetically produced distribution of χ^2/DOF only deviates from the observed distribution by $\lesssim 10\%$; similar agreement was seen in analogous plots for other values of N.

3.4.1 Comparison with Strahl Model

Having fit for the slope m (Eq. 3.8) for each strahl distribution f_s, we calculate the distribution's "measured θ_{FWHM}":

$$\theta_{FWHM} = 2\cos^{-1}\{1 - \log(1/2)/m\}. \tag{3.12}$$

This formula follows from equation (3.7), utilizing the definitions of y and z. For completeness, we note a selection criterion: a distribution f_s was only retained for study if the fit for the slope m (eq. 3.8) yielded a "measured θ_{FWHM}" (eq. 3.12) that was less than twice the maximum pitch angle among the bins of f_s. This avoids extrapolation

errors in our determination of θ_{FWHM}.

The strahl widths measured by this procedure are compared with the analytical prediction given by Eq. (2.14), in Fig. (9). The (peak-normalized) joint probability distribution shown, which compares the "expected" and "measured" θ_{FWHM}, is comprised of 100,000 width measurements of the fast wind ($v_{sw} > 550$ km/sec) strahl. To calculate the "expected" θ_{FWHM} from the data, we must extrapolate to find the values of n_{45} and r_{45} from the local parameters. The value of r_{45} is calculated according to Eq. (2.8), using the solar wind speed v_{sw} as derived from the proton bulk speed measured by Wind/SWE, and assuming $\omega_S = 2\pi/24.47$ days^{-1} (70). We assume that the density n varies with heliocentric distance as $n(r) \propto r^{-2}$, so that the density $n_{45} = n(r_{45})$ can be extrapolated straightforwardly from the local density measured by Wind. Assuming as before that the alpha particle density is 5% of the proton density n_p, we find that n_{45} can be estimated by the formula:

$$n_{45} = 1.1 n_p \left(\frac{r_{45}}{1\,\mathrm{AU}} \right)^{-2}. \tag{3.13}$$

Empirically, the value n_p in Eq. (3.13) is the local proton density as observed by SWE's Faraday cup at r =1 AU.

We see from Fig. (9) that our analytic formula (2.14) shows a reasonably good agreement with the observed strahl broadening, although it slightly underestimates the width, by about 15–20%. There may be several sources for the systematic error in our derivation. The discrepancy may result from the approximations that we used when we simplified Eqs. (2.3) and (2.4), from our evaluation of the parameter y in Eq. (2.10) where we assumed that the solar wind speed is constant (see appendix B), or from our idealized assumptions about the Parker spiral that do not take into account large-scale magnetic and

density fluctuations (e.g., due to large-amplitude Alfvén waves, corotating interaction regions, magnetic discontinuities, shocks, etc.). Importantly, however, the discrepancy may also result from the fact that Coulomb collisions may not be the only mechanism that provides the electron pitch-angle scattering. In the latter case, wave-particle interactions with ambient turbulence may possibly explain extra strahl broadening. Our analysis indicates that Coulomb collisions provide the primary scattering mechanism, however, as the strahl widths would be fully accounted for by an artificial increase of only 30-40% in the diffusion coefficient (noting that θ_{FWHM} scales as a square root of the diffusion coefficient).

Our model predicts that θ_{FWHM} depends on both the electron density n and the detector energy K, through scaling relations (i) and (ii). These dependencies cannot be discriminated in figure 9, so we will now examine them individually. In figure 10 we demonstrate (i): the strahl width is inversely proportional to the energy, for fixed density. To make this figure, we consider only fast wind data for which the background electron density falls within a narrow range, $3.6 < n < 4.4$ cm^{-3}. For this data, which is effectively a subset of the data shown in figure 9, we plot the measured θ_{FWHM} versus the detector energy K. The column-normalized 2D histogram nicely matches the predicted trend (equation 2.15), which is shown as a solid line for $n = 4$ cm^{-3}. To produce this line, we set $r_{45}/r = 1.2$—which follows from assuming representative values for our fast wind data set: $v_{sw} = 550$ km/sec and $\omega_s = 2\pi/24.47$ days^{-1} (eq. 2.8). Similar predictions for $n = 3.6, 4.4$ cm^{-3} are shown as dotted lines.

We now verify scaling relation (ii), in a similar manner. The SWE strahl detector only sampled the distribution function at discrete energies; in figure 11, we only show fast wind data measured at energy $K = 270$ eV. Here we plot a column-normalized

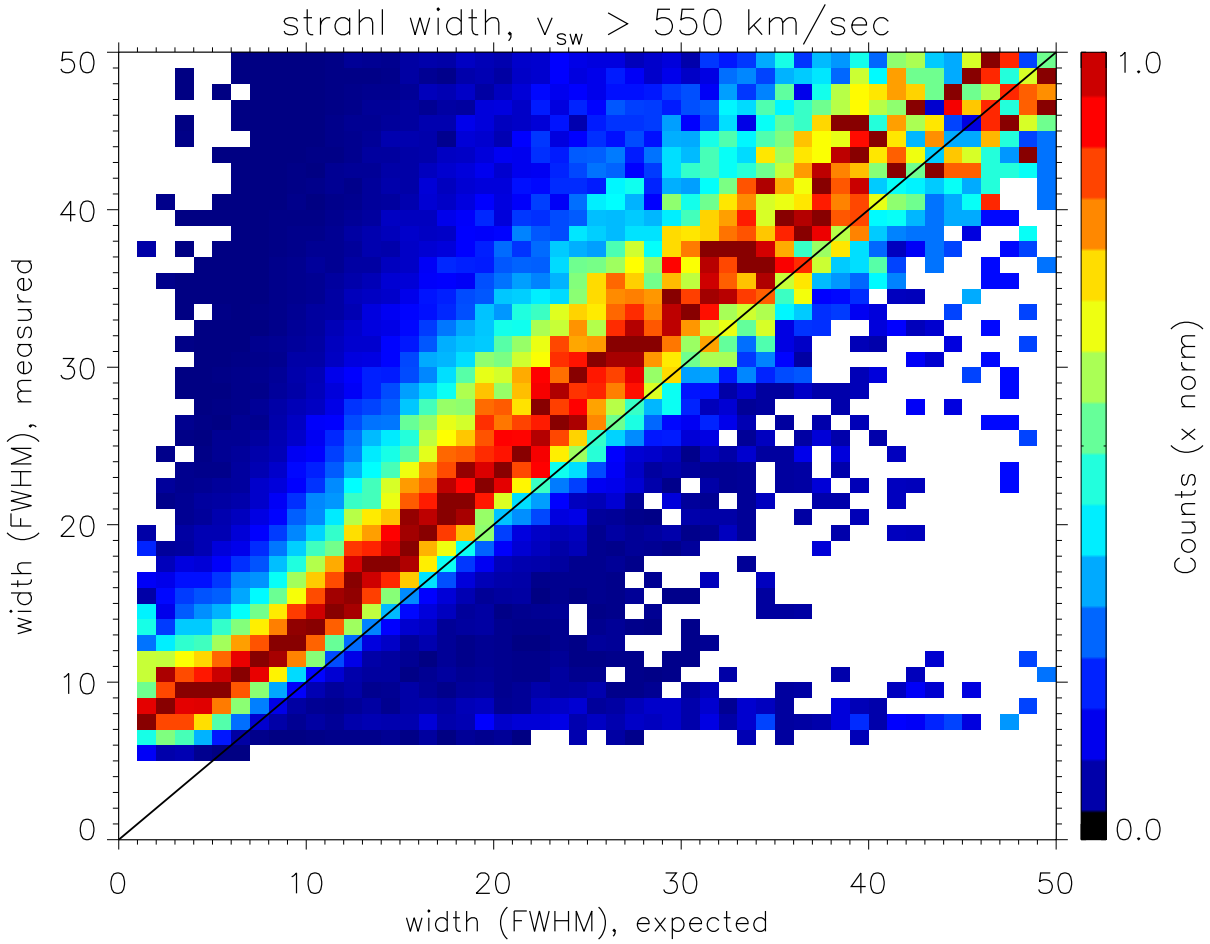

Figure 9: The electron-strahl width measured in the fast solar wind intervals (y-axis), as described in (33), compared with the analytic prediction (x-axis) given by Eq. (2.14). Here we present the joint probability distribution of the "measured" and "expected" values of θ_{FWHM}, normalizing each column of the distribution by that column's peak value. The most probable observed widths nearly agree with the predicted values, to within 15-20%—the data would agree exactly if it fell on the solid diagonal line, shown for reference. As mentioned in the text, θ_{FWHM} can only be resolved to a minimum of about $\sim$5–10°, which helps explain the relatively large deviation seen between theory and experiment at very small widths.

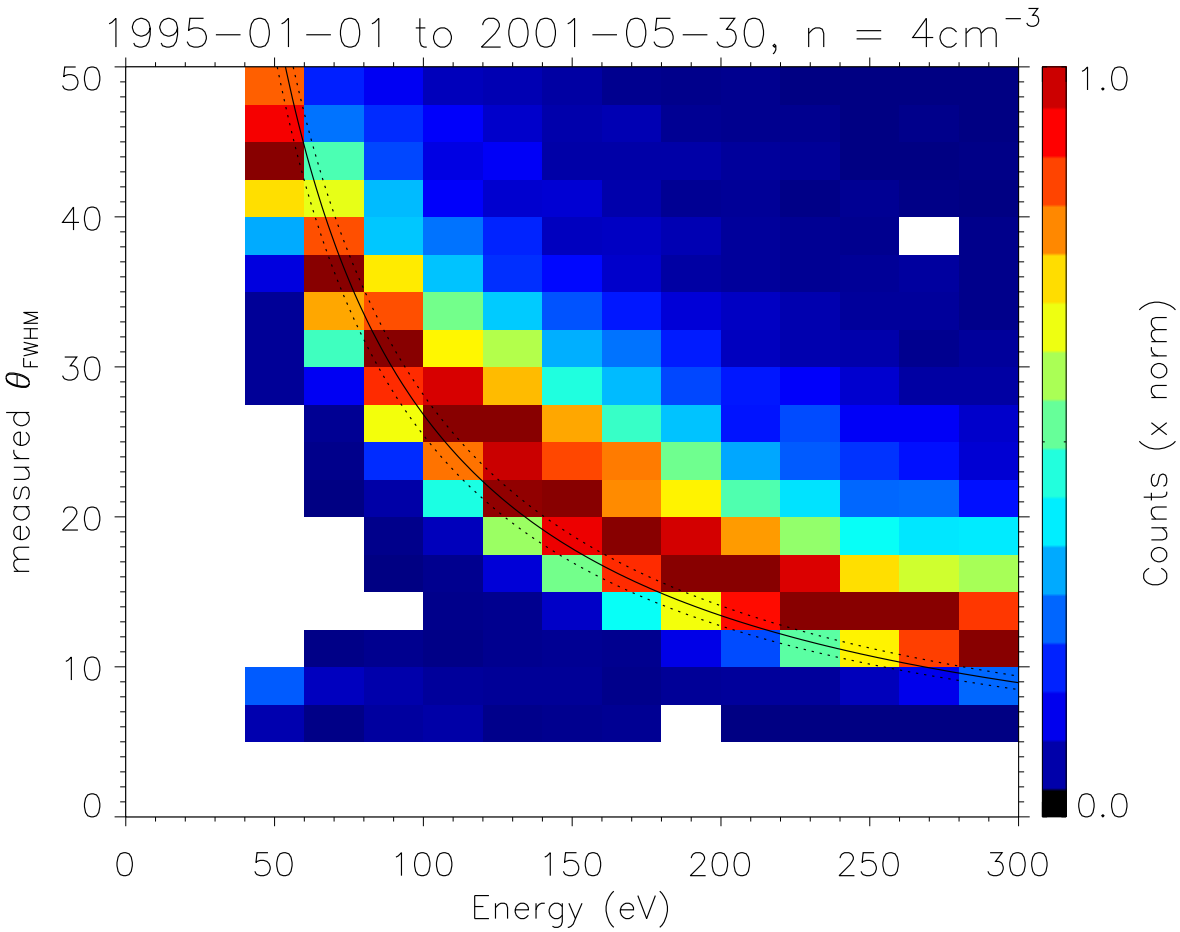

Figure 10: Experimental verification of scaling relation (i): $\theta_{FWHM} \propto K^{-1}$ at fixed n. Data shown fall in the range of densities $3.6 < n < 4.4\text{cm}^{-3}$.

2D histogram of the measured θ_{FWHM} versus the electron density n. For comparison, we show our model's prediction for the strahl width at this energy, as a solid line. Predictions resulting from varying K by $\pm 3\%$ (energy range admitted by the detector), are shown as dotted lines.

In figures 9, 10, and 11, strahl widths are only shown for the regime $\theta_{FWHM} < 50°$. This is because the asymptotic formula for the strahl, equation 2.13, was derived under the assumption $\mu \approx 1$. Including data with pitch angles less than 25° corresponds with the regime $\mu > 0.9$, so our assumption is well-satisfied.

Our 100,000 fits represent only about 1% of the distributions (f_s) measured by the SWE strahl detector. Despite this low proportion, we believe our data are representative of the fast wind strahl. We note our cleaning procedure (section 3.3) and selection criteria make only a small proportion of the observed f_s suitable for our study. That is, we only consider fast wind strahls that are prominent and resolved by the detector. This tends to exclude high-energy measurements. For example, SWE/strahl measured f_s at energies > 500 eV about 38% of the time; only 5% of our retained fits are at these energies.

The data presented in this study include some measurements made during transient events, such as shocks and coronal mass ejections (CMEs). During such events, the eVDF can exhibit properties that are not representative of the ambient fast wind; e.g. "counterstreaming" strahls associated with CMEs. Due to the complexity of the task of sorting our data for all events that could potentially exhibit anomalous anti-sunward strahls, we assume such events to be infrequent enough as to not appreciably bias our data. To justify this assumption, we have conducted a preliminary study, in which we repeated the analysis presented in this section, but excluded data measured during times when a CME passed the Earth (as tabulated in (58)). This exclusion had minimal

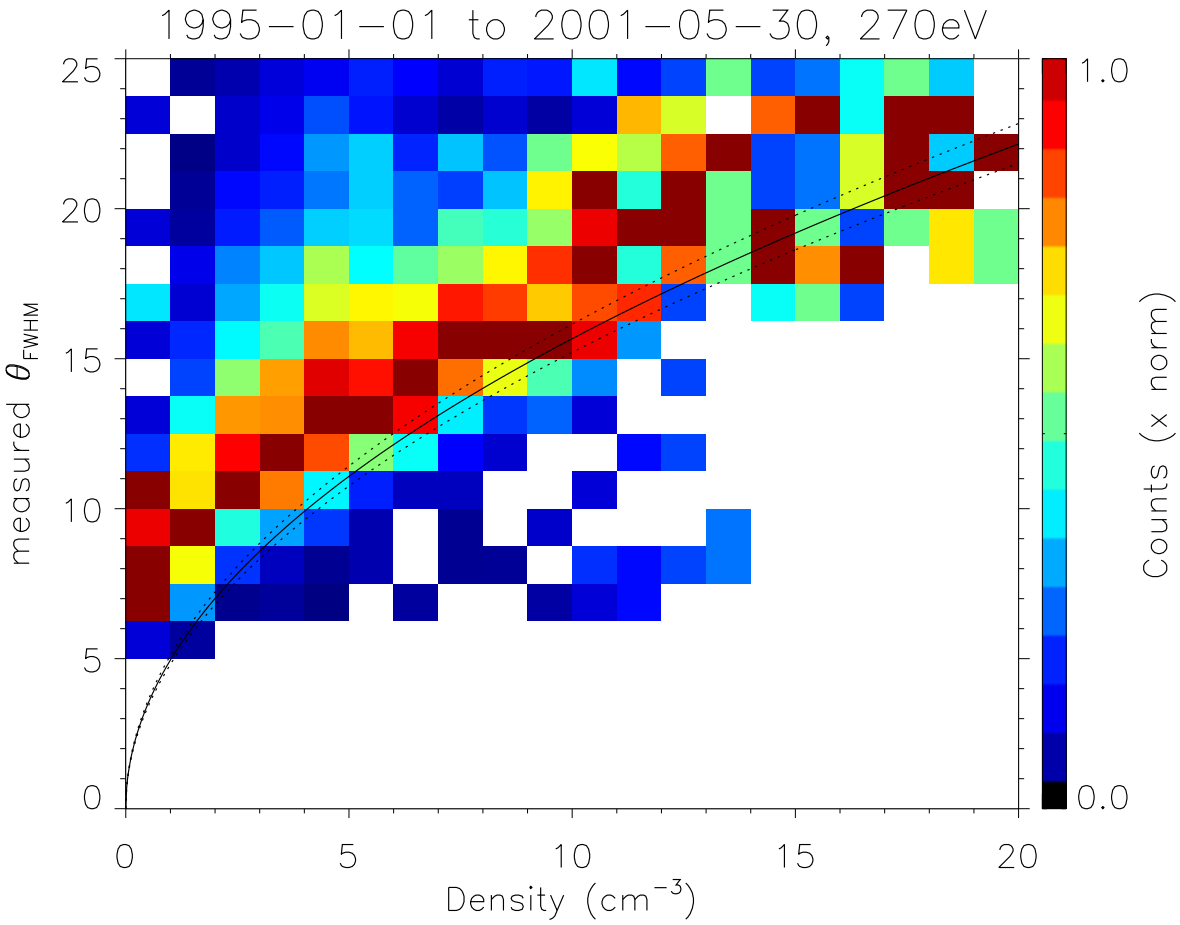

Figure 11: Experimental verification of scaling relation (ii): $\theta_{FWHM} \propto \sqrt{n}$ at fixed K. Data shown at detector energy 270 eV (specified by the detector with accuracy $\Delta K/K \approx 3\%$).

effect on the plots presented in figures 9, 10, and 11. We note also that of the eVDF measurements used for fitting here, that took place after May 27, 1996 (the date of the first CME in the index), only 16% were measured during the transit of a near-Earth CME.

3.5 Fitting to F_{ave}

The results of section 3.4 demonstrate that our model accurately captures the strahl width's dependence on density and energy. However, we have not yet analyzed the overall amplitude of the strahl, which is captured by the arbitrary function $C(v^2)$ appearing in Eq. (2.13). A previous study (49) computed the strahl amplitude $f_{s,max}$, which at a given energy occurs along the magnetic field direction ($\theta = 0$). They found that the amplitude varies as an exponential function of the energy K (Eq. 2.16): $f_{s,max}(K) \sim \exp(-K/T_{strahl})$, where the observed values T_{strahl} ∼100 eV are reminiscent of coronal temperatures. Only a few test cases were presented in (49), however, and we would like to study this problem more broadly and with improved statistics. In this section, we will conduct a similar analysis—originally presented in (33)—assuming that the strahl peak varies as a power law with energy: $f_{s,max}(K) \sim K^{\epsilon}$, where ϵ is a constant to be determined by fitting to the data.

We would like to fit the observed distributions directly to our model function, Eq. (2.13), in order to empirically determine the functional variation of $f_{s,max}(K)$ that is representative of the fast wind. Approaching this problem for our data set (which spans more than 6 years) is no small task, so we will attempt to reduce the problem by combining the observed spectra into an averaged distribution, that we will call $F_{ave}(\mu, \xi)$.

The reader should note the capitalization of the distribution F_{ave}, and the introduction of a new independent variable ξ—let us here discuss this notation.

The electron distributions measured in the fast wind at 1 AU show significant variation across our data set; for instance, the observed densities span roughly an order of magnitude 1 cm$^{-3} \lesssim n \lesssim 10$ cm^{-3} (see Fig. 10). Let us consider a Maxwellian core distribution, which is usually modeled with the form:

$$f_c(\mathbf{v}) = \frac{n_c}{\pi^{3/2} v_{th}^3} \exp\left(\frac{-v^2}{v_{th}^2}\right), \tag{3.14}$$

where n_c denotes the core density v_{th} is the core thermal speed, which is related to the core temperature T_c via the formula $v_{th} = \sqrt{2T_c/m_e}$. Even if the densities of the core distributions are the same across two different measurements, the distributions will appear quite different if they have different temperatures (the observed temperatures also vary significantly across our data set). In order to analyze the *shape* of the distribution (including the suprathermal populations), it then is appropriate to normalize (as in, e.g., 76) the amplitude of f to the core amplitude, and to scale speeds to the core thermal speed $v_{th} = \sqrt{2T_c/m_e}$. Let us then introduce the (dimensionless) normalized distribution $F(\mathbf{v}/v_{th})$, which can be computed from the physical distribution $f(\mathbf{v})$ from the following formula:

$$F(\mathbf{v}/v_{th}) = \frac{v_{th}^3 f(\mathbf{v})}{n_c}. \tag{3.15}$$

Now, introducing the independent variable ξ,

$$\xi \equiv \frac{v^2}{v_{th}^2}, \tag{3.16}$$

we see that eq. (3.14), which describes the core distribution f_c, reduces to the form:

$$F_c \equiv \frac{v_{th}^3 f_c}{n_c} = \frac{\exp(-\xi)}{\pi^{3/2}}. \tag{3.17}$$

We see the utility of the normalization (3.15): the core distribution appears the same regardless of the temperature and density. Normalizing the whole distribution in this fashion will allow us to study the strahl distribution, as it appears *relative* to the core.

3.5.1 Analysis

Having analyzed the angular variation of the strahl in detail in section 3.4, we now conduct a new comparison between the data and equation 2.13, with 2D fits that describe the variation of the eVDF with both angle and energy. We will assume the function $C(v^2)$ appearing in equation 2.13 is a power law, and write the distribution in terms of independent variables μ, ξ. As in chapter 2, we will assume small angles, so we can approximate $1 - \mu^2 \approx 2(1 - \mu)$. We will assume that the density varies as the inverse square of the distance, $n \propto r^{-2}$, and set the distance to r =1 AU (the location of the Wind satellite). Normalizing the distribution to the core population, as described by Eq. (3.15), our strahl model (2.13) can then be expressed in the form:

$$F(\mu, \xi) = C_0 \xi^{\epsilon} \exp\left\{\tilde{\gamma}\Omega\xi^2(1 - \mu)\right\}, \tag{3.18}$$

In (3.18) we have introduced the notation $\tilde{\gamma}$ for the so-called temperature Knudsen number. The Knudsen number parametrizes the collisionality of the system, literally the ratio[4] between the mean free path $\lambda_{mfp} = (T^2/2\pi e^4 \Lambda n)$ and the system scale size r:

[4]The Knudsen number is usually represented as the ratio between λ_{mfp} and the temperature scale height $L_T \equiv (d \ln T/dr)^{-1}$. As $L_T \sim 1$ in the solar wind, we will simply refer to $\tilde{\gamma}$ as the Knudsen

$$\tilde{\gamma} \equiv T^2/(2\pi e^4 \Lambda n r). \tag{3.19}$$

In (3.18) we also introduced the parameter Ω:

$$\Omega \equiv -\frac{1}{\beta\sqrt{1+(r/r_{45})^2}}. \tag{3.20}$$

Note that the parameters C_0, ϵ, and Ω appearing in equation 3.18 are constants to be determined via the fitting procedure.

Since each angular distribution f_s was measured at a single energy by the SWE strahl detector, for the purpose of filling out the μ-ξ space with data we must develop a method of combining multiple measurements. We choose to do this by computing an average distribution $F_{ave}(\mu, \xi)$ from the data, which will be used for our 2D fits. $F_{ave}(\mu, \xi)$ is composed from data that are measured in principle at many different times within our >6 year period of study, and may be associated with many different flux tubes. Since we expect the prevalence of the strahl to vary significantly with collisionality $\tilde{\gamma}$ (see section 1.5), we will only average together distributions that fall within a narrow range of Knudsen numbers.

For each cleaned angular distribution f_s, the associated normalized distribution F_s is calculated according to equation 3.15 using the local plasma parameters n, v_{th}. The angular bins of F_s are assigned coordinates[5] μ and ξ, which are then sorted into a μ-ξ grid with resolution $\Delta\mu = 0.0005$, $\Delta\xi = 1$. All of the strahl data from our >100,000 fits are sorted in this way and averaged by μ-ξ bin to construct the distribution $F_{ave}(\mu, \xi)$.

number, for convenience.

[5]The energy $\xi = K/T$ is calculated from the detector energy K and local temperature T, while μ depends on each angular bin and on the $\hat{B}$ direction that was determined during the angular fitting procedure (section 3.4).

As mentioned, we expect the distribution to depend on the Knudsen number, so we only average together data with similar values of $\tilde{\gamma}$ (calculated from the locally observed n and T) when computing F_{ave}. We bin by $\tilde{\gamma}$ logarithmically, covering the range $0.365 < \tilde{\gamma} < 3.651$ in 8 bins. This range contains $\sim$90% of our fast wind strahl measurements. Cuts of F_{ave}, for these 8 Knudsen numbers, are shown as points in Figure 12. The error bars displayed are the nominal standard deviation of the mean that is computed during the averaging process.

Once the average distribution $F_{ave}(\mu, \xi)$ is constructed, we fit the data to our model function, equation 3.18. The parameters C_0, ϵ, and Ω are determined by a nonlinear least squares fit. For the purpose of fitting, $\tilde{\gamma}$ is set to a fixed value, the geometric mean of the maximum and minimum $\tilde{\gamma}$ that were used to bin F_{ave}. A comparison between F_{ave} and our fitted model function is shown in figure 12. In the interest of presenting the data clearly, we choose to fit along only along a few cuts of F_{ave}. Namely, we fit to data along the cuts $\mu = 0.9995$, 0.9960, 0.9850, 0.9660, 0.9395, 0.9065, which corresponds with roughly 5° spacing in pitch angle. These cuts of our fit function are shown as lines in the figure.

Some cuts in figure 12 span a larger energy range than others, because the data must satisfy multiple selection criteria to be included in the fit. Two of these selection criteria are based on the expected width of the strahl at each energy ξ. In terms of Ω, we can write the strahl full width at half maximum, θ_{FWHM}, as (see Eq. 3.18):

$$\theta_{FWHM} = 2\cos^{-1}\left\{1 + \frac{\ln(2)}{\tilde{\gamma}\Omega\xi^2}\right\}. \tag{3.21}$$

We predict θ_{FWHM} by assuming $\Omega = -0.34$ (this assumption is seen to be reasonable a posteriori, see Table 1). Our selection criteria are then as follows: first, if the expected

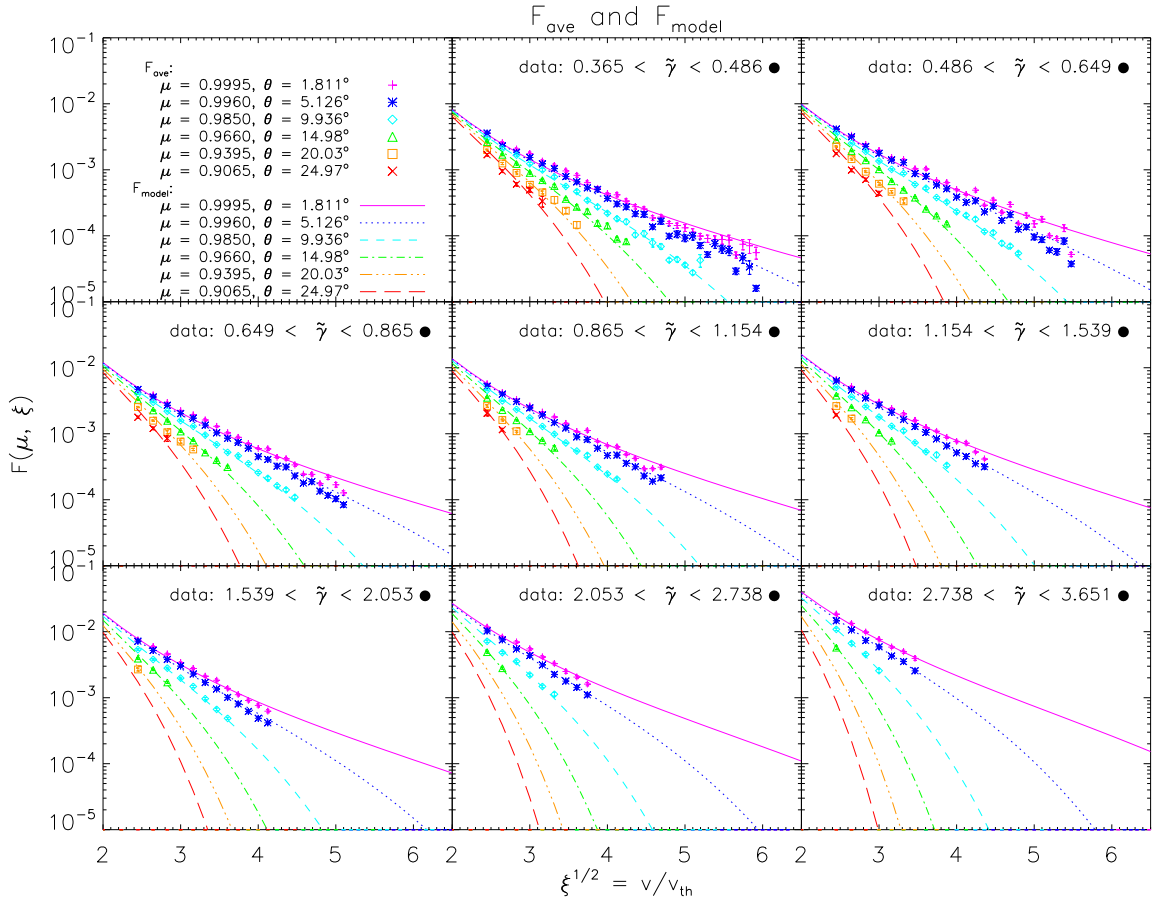

Figure 12: The 2D strahl distributions $F_{ave}(\mu, \xi)$ are constructed from averaging pitch angle distributions measured by the SWE strahl detector, from fast wind data where $\tilde{\gamma}$ falls within a given range. Data are selected only where the strahl amplitude is sufficiently above the background, and where the strahl is expected to be resolved (see section 3.5). Cuts of F_{ave} are shown as points. Fits to a Coulomb scattering model (F_{model}), given by equation 3.18, are plotted as lines. Parameters of the fits are displayed in Table 1.

$\tilde{\gamma}$ range (F_{ave})	nominal $\tilde{\gamma}$ (F_{model})	C_0	ϵ	Ω
—	—	model: $F(\mu,\xi) = C_0\xi^\epsilon \exp\{\tilde{\gamma}\Omega\xi^2(1-\mu)\}$		
$0.365 < \tilde{\gamma} < 0.486$	$\tilde{\gamma} = 0.421$	0.157 ± 0.011	-2.13 ± 0.031	-0.38 ± 0.013
$0.486 < \tilde{\gamma} < 0.649$	$\tilde{\gamma} = 0.562$	0.191 ± 0.014	-2.14 ± 0.033	-0.35 ± 0.013
$0.649 < \tilde{\gamma} < 0.865$	$\tilde{\gamma} = 0.749$	0.234 ± 0.019	-2.14 ± 0.035	-0.30 ± 0.012
$0.865 < \tilde{\gamma} < 1.154$	$\tilde{\gamma} = 1.000$	0.264 ± 0.020	-2.13 ± 0.033	-0.28 ± 0.011
$1.154 < \tilde{\gamma} < 1.539$	$\tilde{\gamma} = 1.333$	0.306 ± 0.025	-2.13 ± 0.036	-0.27 ± 0.010
$1.539 < \tilde{\gamma} < 2.053$	$\tilde{\gamma} = 1.778$	0.401 ± 0.040	-2.19 ± 0.045	-0.25 ± 0.011
$2.053 < \tilde{\gamma} < 2.738$	$\tilde{\gamma} = 2.371$	0.485 ± 0.053	-2.08 ± 0.050	-0.28 ± 0.010
$2.738 < \tilde{\gamma} < 3.651$	$\tilde{\gamma} = 3.162$	0.669 ± 0.065	-2.02 ± 0.046	-0.28 ± 0.009

Table 1: Model parameters C_0, ϵ, Ω corresponding with fits displayed in figure 12. The range of $\tilde{\gamma}$ listed in each row represents the Knudsen numbers spanned by the data used to create F_{ave}. The column "nominal $\tilde{\gamma}$" shows the Knudsen number used for the fit.

θ_{FWHM} (3.21) at a given energy is less than 10°, these data are not included; this is to ensure that the measured strahl is resolved by the detector. Secondly, if F at a given angle is expected to be less than 1/5 the peak ($\mu = 0$) value at that same energy, then the data are not included in the fit; this is to prevent any accidental contamination by the halo.[6]

Additionally, we only include data that falls in the energy range $\xi > 5$, because our model equation was derived under the assumption $\xi \gg 1$ (see chapter 2).

The results of our fits, for various Knudsen numbers, are summarized in table 1. We note that the overall amplitude of the strahl (relative to the core), C_0, increases with $\tilde{\gamma}$. This is as expected, since more runaway electrons should be observed as collisionality decreases. The fit parameter ϵ, which dictates the energy dependence of the strahl amplitude, seems fairly independent of $\tilde{\gamma}$, with $\epsilon \approx -2.1$ for all 8 fits. The fit parameter Ω is also fairly constant, with $\Omega \approx -0.3$ describing most fits well.

[6]See also step "Remove the halo" of our data cleaning procedure, section 3.3.

An important caveat should be kept in mind when interpreting the data in Table 1: in order to calculate $\tilde{\gamma}$ (used in both the model function and when binning F_{ave} by Knudsen number), we assumed $\tilde{\gamma} = 25.5$. This is the appropriate value for the Coulomb logarithm, when considering scattering of the *core* population (e.g., 65). Indeed, the exposition in chapter 2 assumes the value $\Lambda = 30$, which is a more appropriate value for treating the strahl; see section 2.2. We have displayed the results of our fits as they appeared in the original reference (33). The reason is in part because the correction is fairly small—to correct for this error the values of $\tilde{\gamma}$ (Table 1) should to be divided by a factor of $30/25.5 \approx 1.2$, and the values of Ω should be multiplied by this same factor. As these terms enter our model (3.18) only as a product ($\tilde{\gamma}\Omega$), we do not believe this error seriously affects our results. Nonetheless, we note that the next chapter refers to the results of Table 1, to develop a stability analysis of a model core-strahl distribution, where it is implicitly assumed $\Lambda = 25.5$. As mentioned in the introduction to this section, the analysis of F_{ave} was primarily focused on obtaining an estimate for the energy-scaling of the strahl peak ($\epsilon \approx -2.1$), which is basically unaffected by these considerations.

Chapter 4

Electron Kinetic Stability

4.1 Introduction

The results of chapter 3 demonstrate that the solar wind data are effectively described by our model of the electron strahl (introduced in chapter 2). However, this analysis did not address the question: are the electron distributions *stable*? That is, are there any growing wave modes in the solar wind plasma that may resonate with the strahl electrons and perturb their motion, and therefore affect their distribution in velocity space? Motivating this question, we note for instance that our collisional model of strahl broadening slightly underestimated the observed strahl widths that were presented in chapter 3; wave-particle interactions, as would be generated in the presence of a kinetically unstable electron distribution, may account for the small amount of additional diffusion required to explain the strahl widths.

In this chapter, we perform a numerical linear stability analysis using the LEOPARD solver (3), which allows for arbitrary gyrotropic distribution functions in a magnetized plasma. This work was originally published in (30). In contrast with previous reports, we do not find evidence for a whistler instability directly associated with the electron strahl. This may be related to the more realistic shape of the electron strahl distribution function adopted in our work, as compared to previous studies. We however find that

for typical solar wind conditions, the core-strahl distribution is unstable to the kinetic Alfvén and magnetosonic modes, which are in resonance with the core electrons. The maximum growth rates for these instabilities occur at wavenumbers $kd_i \lesssim 1$ (where d_i is the ion inertial length), at moderately oblique angles of propagation, thus providing a potential source of kinetic-scale turbulence. We therefore suggest that if the whistler modes are invoked to explain anomalous scattering of strahl particles, these modes may appear as a result of nonlinear mode coupling. Speculatively, these whistlers could then develop into a turbulent cascade at scales $kd_i \lesssim 1$.

4.2 Background

The suprathermal electron populations observed in the solar wind carry free energy that may drive kinetic instabilities. We remind the reader (see section 1.4) that at 1 AU, suprathermal electrons with energies between ∼10 eV and ∼1 keV are typically divided into two components: the halo and strahl (e.g., 55). The halo component is relatively isotropic, and is often modeled in velocity space as a kappa distribution (e.g., 43). The strahl, which we attempted to model in chapter 2, forms a narrow beam in velocity space that is aligned with the local magnetic field **B**, and flows anti-sunward.

The field-parallel skewness of solar wind eVDFs, and the heat flux associated with it, has spurred the study of so-called "heat flux instabilities" (e.g., 19; 20). In these models, the field-parallel bulk velocity of the core population drifts slightly sunward relative to the ions. This drift offsets the anti-sunward flow of the heat flux-carrying particles so that the net parallel current is nearly zero. If the model parameters are adjusted so that the heat flux and associated core drift amplitude both increase, eventually an instability

threshold may be reached for a particular wave mode. (20) modeled the eVDF as a combination of two drifting Maxwellians, which respectively represented the core and halo populations. They found these core-halo distributions to be unstable to Alfvén, magnetosonic, and whistler mode fluctuations, with instability regimes depending on the wavenumber. Empirically, it has been shown that the electron heat flux q may be constrained by thresholds imposed by the whistler as well as the kinetic Alfvén (21; 84; 75) heat flux instabilities; these thresholds are derived assuming a core-halo model eVDF. We note that the core drift and heat flux appear to also be mediated by the Coulomb collisionality of the solar wind, as was shown in large statistical studies of *Wind* satellite data (4; 56).

Kinetic instabilities have garnered particular interest in studies of the strahl population, as they may provide a source of scattering of the strahl beam. Such a source was called for by (39), who incorporated Coulomb collisions into a collisionless model of strahl formation. After comparing with data from the *IMP 8* satellite, it was claimed that pitch-angle scattering by Coulomb collisions alone could not account for the observed angular width of the strahl. Following e.g., (55), we refer to the non-Coulombic scattering that is sometimes invoked to explain the strahl width as "anomalous diffusion" or "anomalous scattering". Recently, (24) inferred the presence of a strahl-scattering process that occurs over distance, by showing that for 1 AU data measured near SEP (Solar Energetic Particle) events, the angular width of the strahl population is correlated with the length of the interplanetary magnetic field lines that stretch back to the coronal base. Beyond anomalous diffusion, wave-particle scattering of the strahl has been suggested by some authors to be a potential source of the nearly-isotropic halo distribution. For instance, (43) and (76) found that the relative densities of the strahl and

halo populations vary inversely with heliocentric distance, providing indirect evidence that the halo population may be formed from scattered strahl particles.

A new analytical model for the strahl distribution was developed in (32)—see chapter 2—by deriving exact solutions to the collisional kinetic equation in the asymptotic high-energy regime relevant to the strahl. This model was compared to eVDF data measured by the *Wind* satellite's SWE strahl detector at 1 AU, with remarkable agreement (chapter 3). In particular, it was shown that the model can predict how the angular width of this population scales with particle energy and background density. The model also predicts, in accordance with (39), that at a given energy the strahl should become narrower with heliocentric distance, before eventually "saturating" at a fixed width at distances $r \gg 1$ AU. By contrast, some authors have reported that the strahl width actually *increases* (27; 25) with distance in the outer heliosphere. Despite the successes of collisional model proposed in (32), it may require improvement through the inclusion of additional physical processes.

Examples of such processes are the kinetic instabilities that can be triggered by a non-Maxwellian electron distribution function. In this work we revisit the question of kinetic instabilites in the solar wind plasma, for an eVDF that is composed of parallel-drifting core and strahl components. For the first time we conduct the stability analysis using a realistic distribution function (developed chapters 2 and 3) for the strahl component, derived from the electron kinetic equation. The strahl distribution function is rather nontrivial and, therefore, its stability analysis has to be conducted numerically. For this purpose, we employ the LEOPARD solver (3), which has been recently developed to analyze the stability of arbitrary gyrotropic distributions in a magnetized plasma.

We search for unstable modes that one may expect to be most relevant to a core-strahl

eVDF: the Alfvén, magnetosonic, and whistler modes. These modes have been shown to be unstable for model distributions composed of drifting core and halo components. For our core-strahl model, we indeed find that the distributions are unstable to the Alfvén and magnetosonic modes with wavenumbers $kd_i \lesssim 1$. The ion inertial length d_i is defined:

$$d_i = v_A/\Omega_i, \tag{4.1}$$

where $\Omega_i \equiv eB/m_p$ is the ion cyclotron frequency and v_A is the Alfvén speed. However, we have not been able to identify the whistler modes that would be directly excited by a Cherenkov resonance with the strahl particles; such modes appear to be damped overall. We therefore speculate that for the strahl particles to be scattered by the whistler modes (as in, e.g. 83; 61), such modes may be generated not by the strahl electrons but rather transferred to small scales as a result of a turbulent cascade, say originating from the core-drift instabilities at $kd_i \lesssim 1$. This result provides a source for whistler waves that is different and complementary to the previously discussed mechanism of whistler instabilities (e.g., 19; 20; 60).

The effect of whistler waves on the eVDF has been investigated in Particle-in-Cell (PIC) simulations. For instance, (62) demonstrated that a broadband spectrum of parallel propagating whistlers could significantly broaden the strahl population. We note though that in PIC simulations of whistler turbulence, e.g., (63) and (8), the parallel temperature of the eVDF increases with time more quickly than the perpendicular temperature. This calls into question the effectiveness of whistler turbulence as a source of electron pitch-angle (perpendicular) scattering; at least insofar as one might try to explain the presence of the nearly-isotropic halo through direct strahl scattering, as

suggested by (76). However, these turbulent simulations did not include a strahl component, so the impact of the turbulence on this component has not to our knowledge been directly studied.

We note that our model core-strahl eVDF omits the halo component; this choice is based on practical and theoretical considerations. First of all, halo-driven instabilities are already a well-studied topic that need not be rehashed here, as it is well known for instance that halo temperature anisotropy and core-halo drift can lead to linear instabilities. Furthermore, the inclusion of a halo component would complicate our model by introducing additional free parameters, such as halo anisotropy and relative density, which would needlessly expand the parameter space we wish to explore. We might reasonably try to simplify such a core-halo-strahl model by assuming a strictly isotropic (and monotonic with energy) halo, which would be consistent with the average properties of this component (54). But isotropic, monotonic distributions are always linearly stable (e.g., 9), so the inclusion of a tenuous isotropic halo can be expected to have only a slight stabilizing effect, and should not introduce any new instabilities beyond those found with the more straightforward core-strahl model. For empirical support of this claim, see section 4.5, in which we present a preliminary stability analysis of a fiducial core-halo-strahl eVDF.

4.3 Core-Strahl Distribution Function

In order to conduct a stability analysis, we will model the electron velocity distribution function $f(\mu, v)$ as a core-strahl system. Since the distributions are assumed to be gyrotropic, we use as independent variables the velocity magnitude v, and cosine of the

pitch angle μ:

$$\mu \equiv \hat{\mathbf{B}} \cdot \mathbf{v}/v, \tag{4.2}$$

where the unit vector $\hat{\mathbf{B}}$ points along the (Parker spiral) magnetic field, in the anti-sunward orientation.

Let us designate our core and strahl model functions as $f_c(\mu, v)$, $f_s(\mu, v)$, respectively. The total distribution is then $f = f_c + f_s$, and the total density n is given by:

$$\int f(\mathbf{v}) d^3v = 2\pi \int_0^\infty \int_{-1}^1 f(\mu, v) v^2 d\mu dv = n. \tag{4.3}$$

The core Maxwellian distribution $f_c(\mu, v)$ is allowed to drift (sunward) at parallel velocity v_d relative to the protons. This distribution has the form:

$$f_c(\mu, v) = \frac{n_c}{\pi^{3/2} v_{th}^3} \exp\left(\frac{-v^2 + 2\mu v v_d - v_d^2}{v_{th}^2}\right), \tag{4.4}$$

where n_c, v_{th} represent the electron core density and thermal speed, respectively.

Our model for the strahl distribution, $f_s(\mu, v)$, comes from Eq. 3.18:

$$f_s(\mu, v) = C_0 A(v) \frac{n_c}{v_{th}^3} \left(\frac{v}{v_{th}}\right)^{2\epsilon} \exp\left[\tilde{\gamma}\Omega (v/v_{th})^4 (1-\mu)\right]. \tag{4.5}$$

In this expression we use the "effective" Knudsen number, Eq. 4.6, which we repeat here for convenience:

$$\tilde{\gamma}(r) = \frac{T^2}{2\pi e^4 \Lambda n_c r}, \tag{4.6}$$

where $T(x) = m_e v_{th}^2/2$ is the core electron temperature, Λ is the Coulomb logarithm, and r is the heliospheric distance. We let the parameters ϵ and Ω be given by empirical measurements (Table 1, from (33)), representative of the typical ($\tilde{\gamma} = 0.75$) fast wind: $\epsilon \equiv -2.14$, $\Omega \equiv -0.3$. A summary of these constants, that do not vary throughout

$\tilde{\gamma}$	0.75
Ω	-0.3
ϵ	-2.14
a	10
b	2 ϵ - 4 = -8.28

Table 2: Constants used in Eq. (4.5), that are not altered throughout our analysis.

our analysis, are given in Table 2. The analytic derivation of the strahl shape (4.5) does not however allow one to obtain the overall strahl amplitude. In section 3.5 the constant C_0 in the strahl distribution was therefore estimated from matching with the observational data. In our current consideration it is kept as a free parameter, and the stability analysis is performed for a range of possible strahl amplitudes C_0.

In Eq. (4.5) we also introduced a truncation function $A(v)$, to ensure that $f_s \to 0$ as $v \to 0$:

$$A(v) = \frac{1}{1 + a(v/v_{th})^b}, \tag{4.7}$$

where we defined constants $a \equiv 10$, $b \equiv 2\epsilon - 4$. The form of this low-energy truncation function is somewhat arbitrary, but its introduction is necessary since Eq. (4.5) was derived assuming $(v/v_{th})^2 \gg 1$. The function $A(v)$ artificially modifies the strahl only at $v < v_{th}$, where the distribution function is anyway dominated by the core component.

As an input to the kinetic solver, we will assume a steady state where the parallel current $J_\parallel$ is zero. That is, we require:

$$J_\parallel \equiv \int v_\parallel f(\mathbf{v}) d^3v = 2\pi \int_0^\infty \int_{-1}^1 f(\mu, v) v^3 \mu d\mu dv = 0. \tag{4.8}$$

We can decompose total parallel current into contributions from the core and strahl, that is:

$$J_\parallel = J_{\parallel,c} + J_{\parallel,s}. \tag{4.9}$$

The analytic form of the core contribution $J_{\parallel,c}$ follows from Eq. (4.4):

$$J_{\parallel,c} = n_c v_d, \tag{4.10}$$

and we can therefore write a simple expression for the core drift v_d that ensures $J_\parallel = 0$:

$$v_d = -J_{\parallel,s}/n_c. \tag{4.11}$$

Eq. (4.11) suggests a simple procedure for finding the core drift v_d that ensures $J_\parallel = 0$. First, the strahl distribution $f_s(\mu, v)$ is integrated numerically to find $J_{\parallel,s}$, and this value is substituted into Eq. (4.11) to find v_d (n_c is given).

In the analysis presented in section 4.4, we will assume a set of plasma parameters that are representative of the fast wind at 1 AU, that we will use as a baseline. These fiducial plasma parameters—the core density n_c, core temperature T, magnetic field strength B—are presented in table 3. These parameters are consistent with a $\tilde{\gamma} = 0.75$, $\beta_e = 0.307$ plasma, where $\tilde{\gamma}$ is defined in Eq. (4.6) and the electron beta, β_e, is defined:

$$\beta_e \equiv 8\pi n_c T/B^2. \tag{4.12}$$

The strahl amplitude C_0, typical of the $\tilde{\gamma} = 0.75$ solar wind (33), is also presented in the table.

4.4 Stability Analysis

We analyze the linear stability of the eVDF using the LEOPARD solver (3), which can calculate the dispersion relation $\omega(\mathbf{k})$ for an arbitrary gyrotropic electron distribution. The imaginary part of our solutions determines the stability of the particular wavemode: stable for $Im(\omega) \leq 0$ and unstable for $Im(\omega) > 0$. We will assume that the large-scale

n_c ($\approx n$)	4 cm^{-3}
T	12.21 eV
B	8 nT
C_0	0.234

Table 3: The set of physical constants presented in this table are used as a baseline for our model. These constants are consistent with a $\beta_e = 0.307$, $\tilde{\gamma} = 0.75$ plasma. When we investigate the effect of β_e on stability, a different set of n_c, T, B will be used (see section 4.4). The strahl amplitude C_0 reported here is a typical value that was measured in the $\tilde{\gamma} = 0.75$ fast wind, see Table 1. The parameter C_0 will be varied to investigate its effect on stability, to produce Figs. 13 and 17.

variation in any plasma parameters (density, temperature, E- and B-fields) is slow enough that it can be neglected on the spatial scale of the waves. For simplicity, we assume the background electric field is zero.

The final solution $\omega(\mathbf{k})$ is found through an iterative scheme, that converges most efficiently when the initial guesses for ω, $\mathbf{k}$ are near an actual solution. As a starting point for our analysis, we use fully kinetic dispersion relations of the kinetic Alfvén, fast magnetosonic, and whistler branches[1] in a Maxwellian plasma given in, e.g., (74). By smoothly varying the parameters in our model, we can then scan through different propagation angles and parameter regimes to explore the stability of the branches with respect to our core-strahl distribution.

For each branch, we scanned through the propagation angles $0° < \theta < 89°$, with $1°$ resolution. At these angles, we varied the strahl amplitude across the values $C_0 = 0.000, 0.050, 0.100, 0.200$ while holding $\beta_e = 0.307$ fixed. Holding $C_0 = 0.234$ fixed and scanning through these same angles, we varied beta across the values $\beta_e = 0.307, 0.500, 0.700$. We completed these scans for wavenumbers $0.1 < kd_i < 1.0$ for the magnetosonic mode and $0.1 < kd_i < 4.0$ for the KAW mode. We conducted a similar analysis over the

[1]These modes are all stable (damped) if the background distributions are Maxwellian, but may be unstable for non-Maxwellian plasmas.

range of wavenumbers $1 < kd_i < 40$ for the whistler mode; however, we investigated only angles $0 < \theta < 79°$ and $\theta = 180°$.

In Fig. 13, we show our numerical results for the kinetic Alfvén (KAW) mode in the range of wavenumbers $0 \lesssim kd_i \lesssim 0.7$. In all figures, frequencies and growth rates are normalized to the ion cyclotron frequency Ω_i and wavenumbers are normalized to the ion inertial length d_i (Eq. 4.1). We solve for the dispersion relation for different strahl amplitudes C_0 (Eq. 4.5), represented as different lines in Fig. 13. Note that adjusting C_0 also requires adjustment of the core drift v_d according to Eq. (4.11). All other physical parameters and constants are as listed in tables 2 and 3. The propagation angle is set to $\theta = 63°$. We see that the distribution becomes unstable if the strahl amplitude is sufficiently large, i.e. in the regime $C_0 \gtrsim 0.20$. We also note that since $Re(\omega < 0)$, the waves propagate with a *sunward* parallel phase speed.

The growth rate of the KAW instability appears particularly sensitive to the propagation angle θ; see Fig. 14. Here we hold the strahl amplitude C_0 constant, and instead vary the propagation angle θ. We see the distribution is only unstable in a range of moderately oblique angles $55° \lesssim \theta \lesssim 69°$, and is maximally unstable at $\theta \approx 63°$.

In Fig. 15, we investigate the KAW instability's dependence on the electron beta. Each line in the figure shows the dispersion relation for a different β_e. The line corresponding with $\beta_e = 0.307$ is generated using the physical parameters given in Table 3. The other lines, representing different β_e, require at least one of the parameters n_c, T, B to be adjusted. Let the fiducial parameters listed in table 3 be written as $n_{c,0}$, T_0, B_0, and let $\beta_{e,0} \equiv 0.307$. To investigate a different plasma beta, $\beta_e = \alpha\beta_{e,0}$ (where $\alpha \neq 1$),

we choose n_c, T, B in the following manner:

$$T = \alpha T_0, \tag{4.13}$$

$$n_c = \alpha^2 n_{c,0}, \tag{4.14}$$

$$B = \alpha B. \tag{4.15}$$

This scheme allows us to scale β_e while holding $\tilde{\gamma}$ and the Alfvén speed v_A constant. Holding $\tilde{\gamma}$ constant enables ready comparison to the fits to the distribution that were conducted in section 3.5, while holding v_A constant follows the precedent set by (22). We see in Fig. 15 that the distribution is unstable in the range $0.2 \lesssim \beta_e \lesssim 0.6$, and is maximally unstable at $\beta_e \approx 0.4$.

The distribution also exhibits a second KAW instability; the unstable regime falls in the range of wavenumbers $1 \lesssim kd_i \lesssim 4$, see figure 16. The unstable waves are more oblique here, with propagation angles falling in the range $78^\circ \lesssim \theta \lesssim 87^\circ$. Although the waves here possess growth rates that are about an order of magnitude larger than the growth rates of the less oblique KAW waves (figure 14), their obliquity makes them less able to couple to whistler waves, and therefore these waves are less relevant to generating whistler turbulence that may scatter the strahl (see section 4.6).

Our core-strahl model function is also unstable to the magnetosonic mode, as shown in Figs. 17, 18, 19. These plots are analogous to Figs. 13, 14, 15 respectively, but for the magnetosonic mode instead of the KAW mode. In figure 17, we see that the function is unstable for the baseline parameters shown in Table 3. We see in Fig. 17 that for the magnetosonic mode, as with the KAW mode, the distribution is unstable when the strahl amplitude is sufficiently large, i.e. in the regime $C_0 \gtrsim 0.20$. Fig. 18 demonstrates that the largest growth rate occurs at $\theta \approx 60^\circ$, a moderately oblique angle. As with the KAW

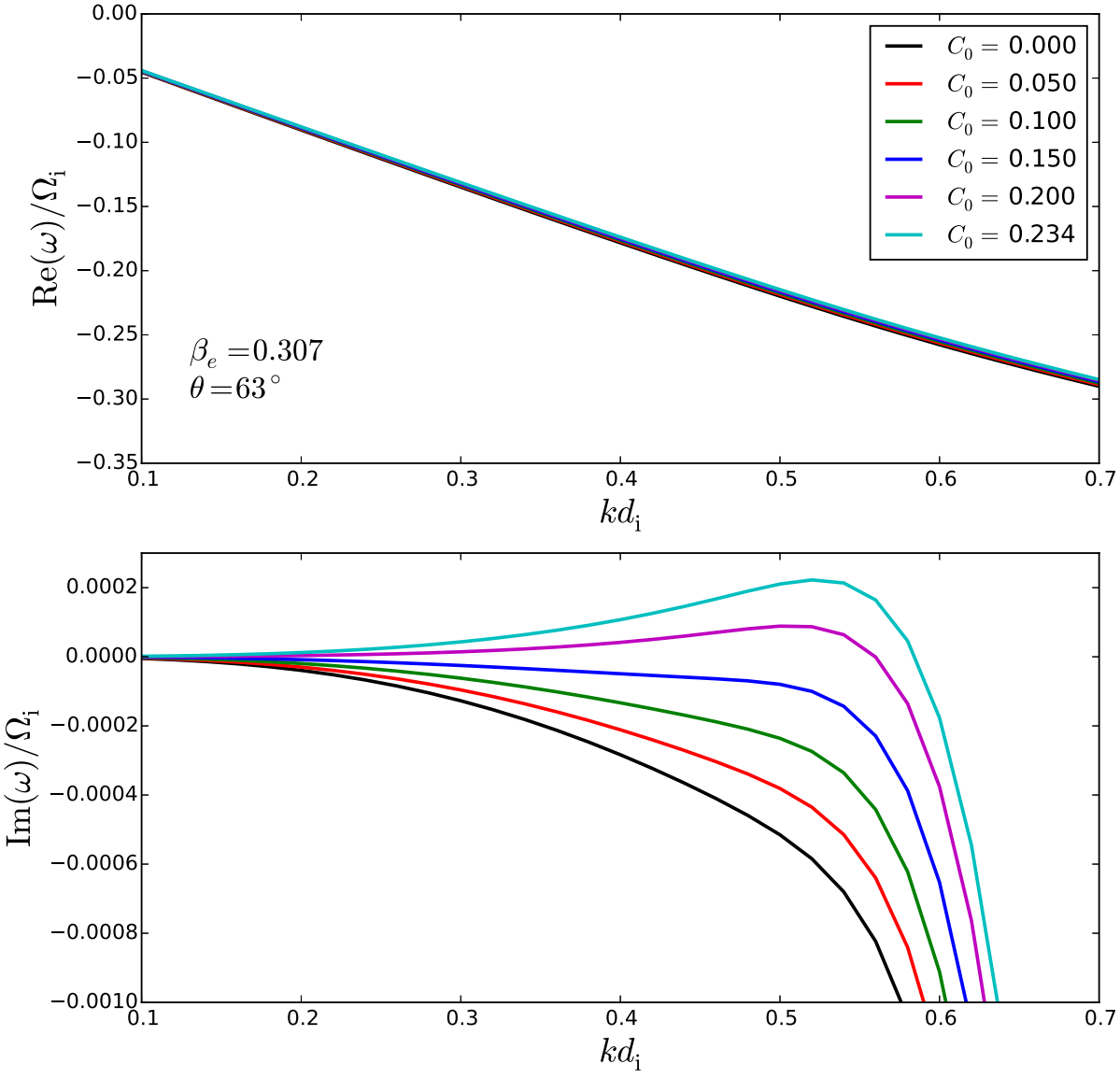

Figure 13: *KAW—Less oblique*. Real (upper) and imaginary (lower) parts of the KAW dispersion relation, shown for different strahl amplitudes C_0. We set $\theta = 63°$ and $\beta_e = 0.307$ for all calculations, but vary the strahl amplitude C_0 (and the core drift v_d, by Eq. (4.11)). The distribution becomes unstable for $C_0 \gtrsim 0.20$.

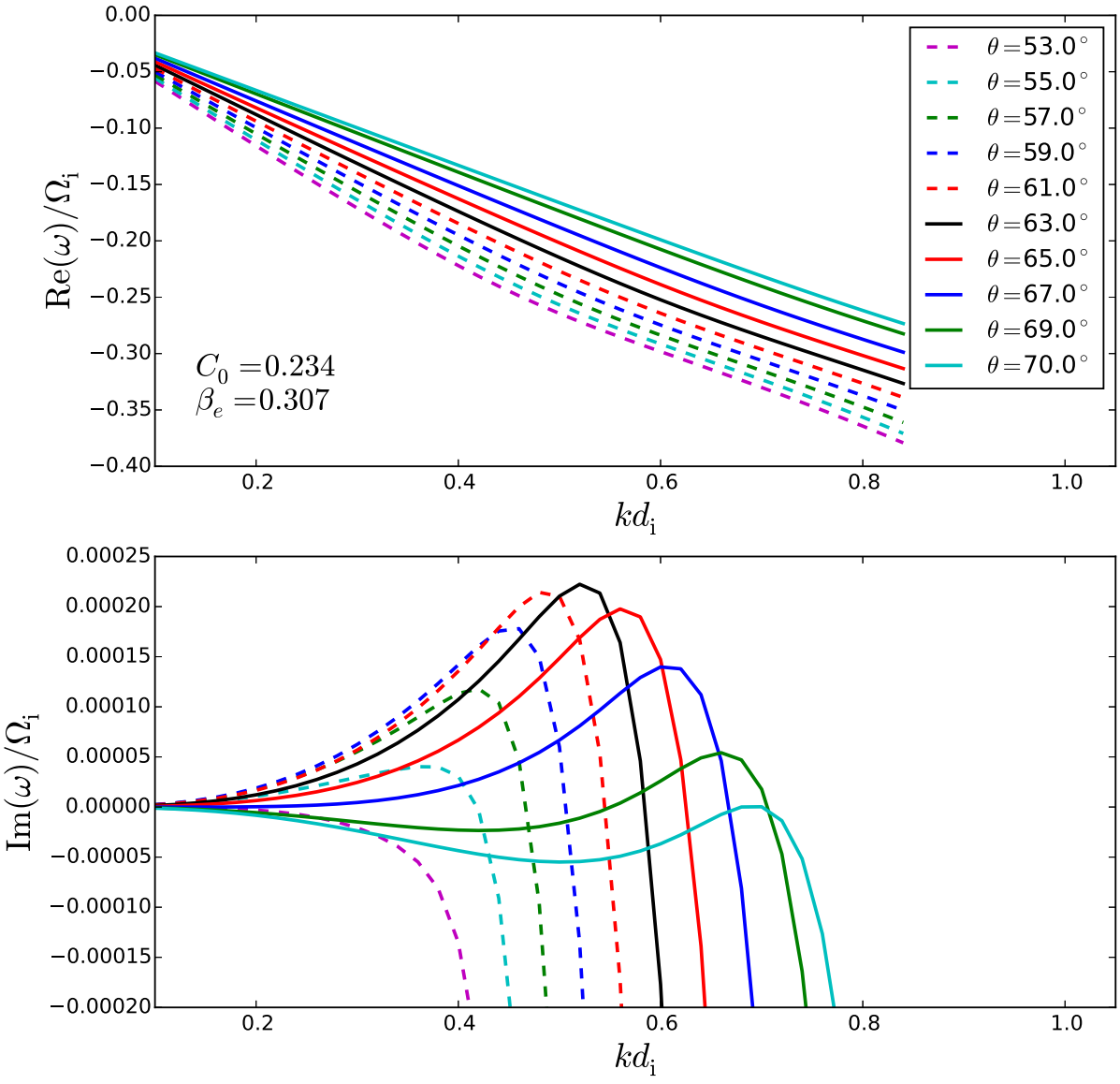

Figure 14: *KAW—Less oblique*. Real (upper) and imaginary (lower) parts of the KAW dispersion relation, shown for different propagation angles θ. We set $\beta_e = 0.307$ and $C_0 = 0.234$ for all calculations, but vary the propagation angle θ. The distribution is unstable in the range $55° \lesssim \theta \lesssim 69°$, and is maximally unstable at $\theta \approx 63°$.

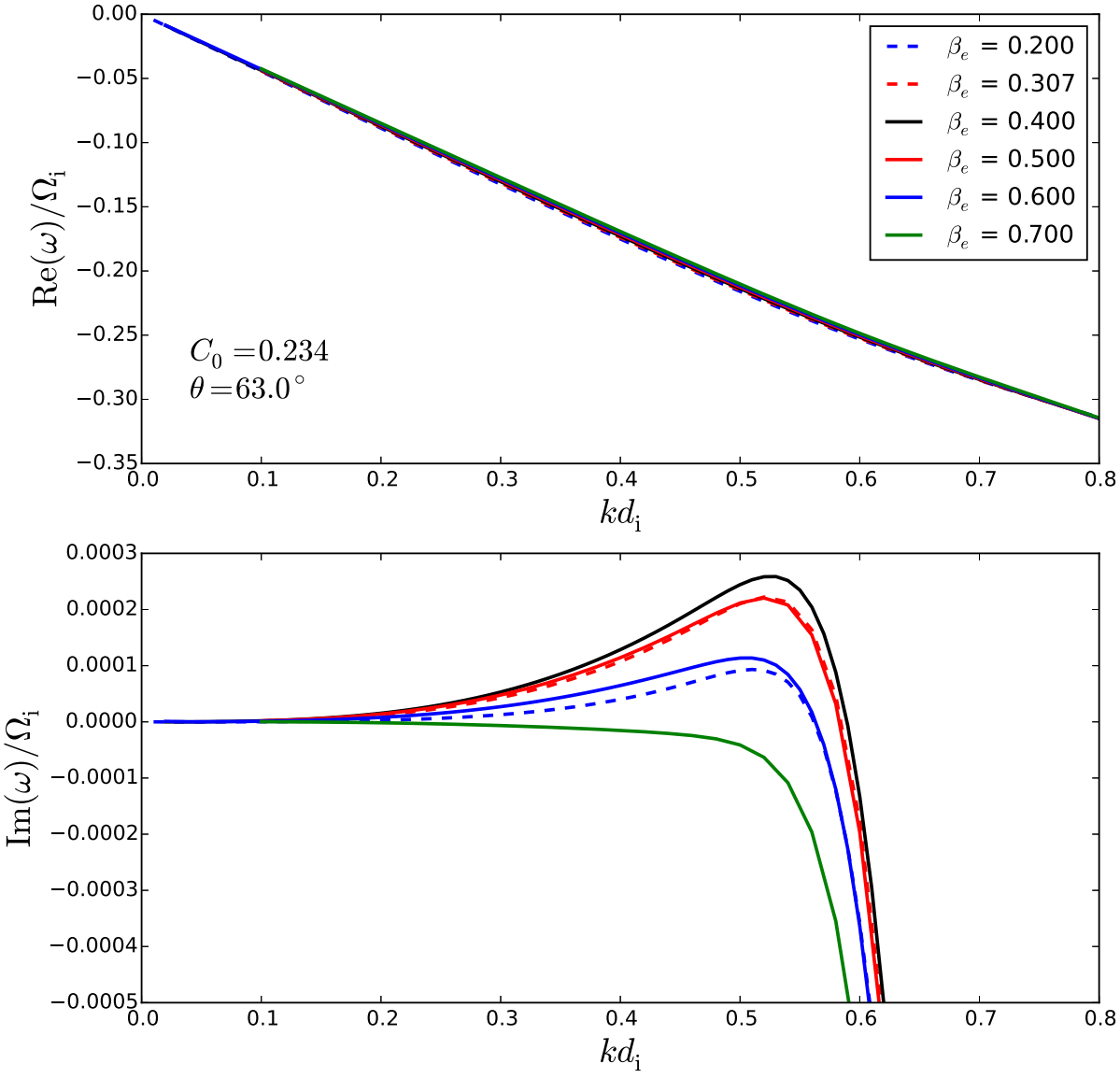

Figure 15: *KAW—Less oblique*. Real (upper) and imaginary (lower) parts of the KAW dispersion relation, shown for different electron betas (β_e). We set $\theta = 63°$ and $C_0 = 0.234$ for all calculations, but vary the electron beta β_e. The distribution is unstable in the range $0.2 \lesssim \beta_e \lesssim 0.6$, and is maximally unstable at $\beta_e \approx 0.4$.

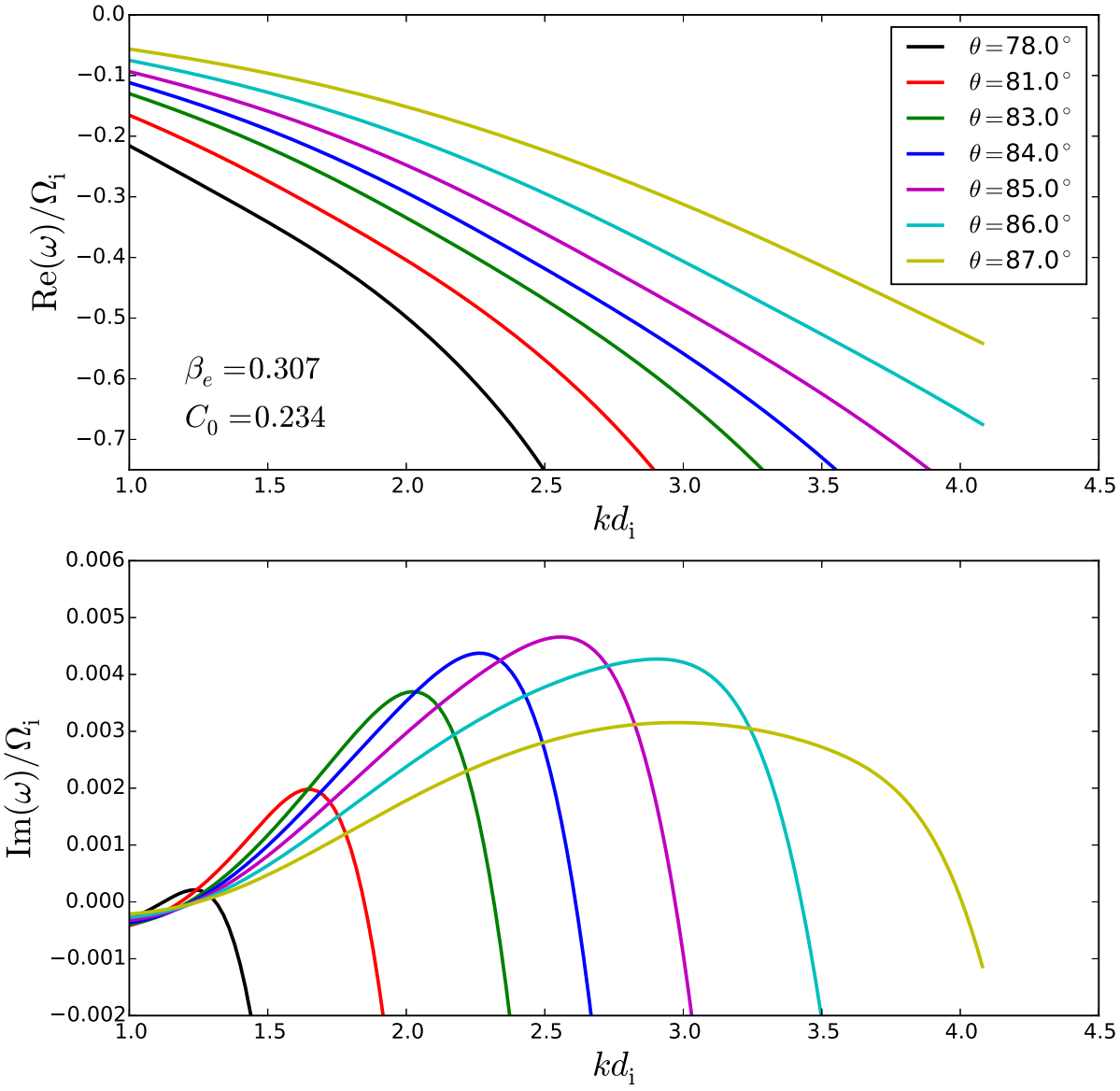

Figure 16: *KAW—More oblique.* Real (upper) and imaginary (lower) parts of the KAW dispersion relation, shown for different propagation angles θ. We set $\beta_e = 0.307$ and $C_0 = 0.234$ for all calculations, but vary the propagation angle θ. Here we see an instability in the range of wavenumbers $1 \lesssim kd_i \lesssim 4$. The distribution is unstable in the range $78^\circ \lesssim \theta \lesssim 87^\circ$, and is maximally unstable at $\theta \approx 85^\circ$.

mode, the instability occurs for $Re(\omega) < 0$; i.e., the waves propagate toward the sun. Fig. 19 displays the instability's dependence on β_e; here we see that the distribution is unstable in the range $0.3 \lesssim \beta_e \lesssim 0.7$, with monotonically increasing growth as β_e increases in this range. The parameter β_e was adjusted by varying n_c, T, B in the scheme described by Eqs. (4.13-4.15) and the preceding paragraph.

Finally, we note that no instabilities were found for the whistler mode. Although we did observe a whistler mode, all solutions were damped ($Im(\omega) < 0$). In addition to searching through the angles 0°-79°, we checked the stability of antiparallel-propagating ($\theta = 180°$) waves as well. We note that the whistler waves observed recently observed by (72), which were attributed to the presence of a heat flux instability, exhibited only parallel and anti-parallel propagation angles. For brevity, we do not show a plot of the whistler results, but note only that the absence of a whistler instability is in contrast with the results of (22), who use a core-halo electron model to show linear theory growth of the whistler heat flux instability.

4.5 Further Analysis: Comparison with a Core-Halo-Strahl Model

In the preceding analysis, we have ignored the halo component, which appears ubiquitously in solar wind eVDFs. Our reasons for omitting this component were described in section 2.13. In particular, we argued that if we were to assume an isotropic halo, its presence would likely have only a slight stabilizing effect on the distribution. In order to test this claim, we here add a halo component to our model eVDF, and compare the

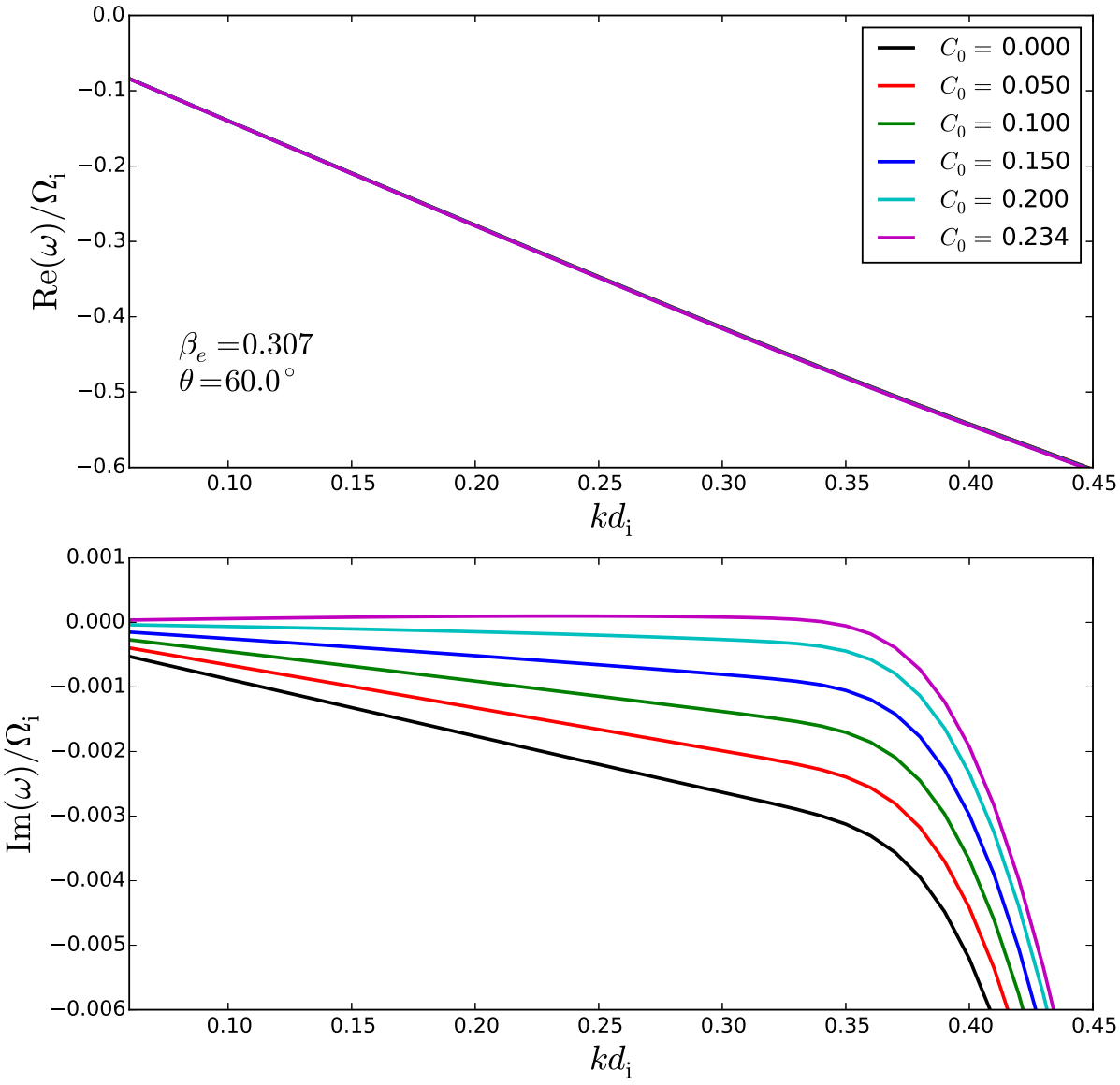

Figure 17: *Magnesotonic.* Real (upper) and imaginary (lower) parts of the magnetosonic dispersion relation, shown for different strahl amplitudes C_0. We set $\theta = 60°$ and $\beta_e = 0.307$ for all calculations, but vary the strahl amplitude C_0 (and the core drift v_d, by Eq. (4.11)). The distribution becomes unstable for $C_0 \gtrsim 0.20$.

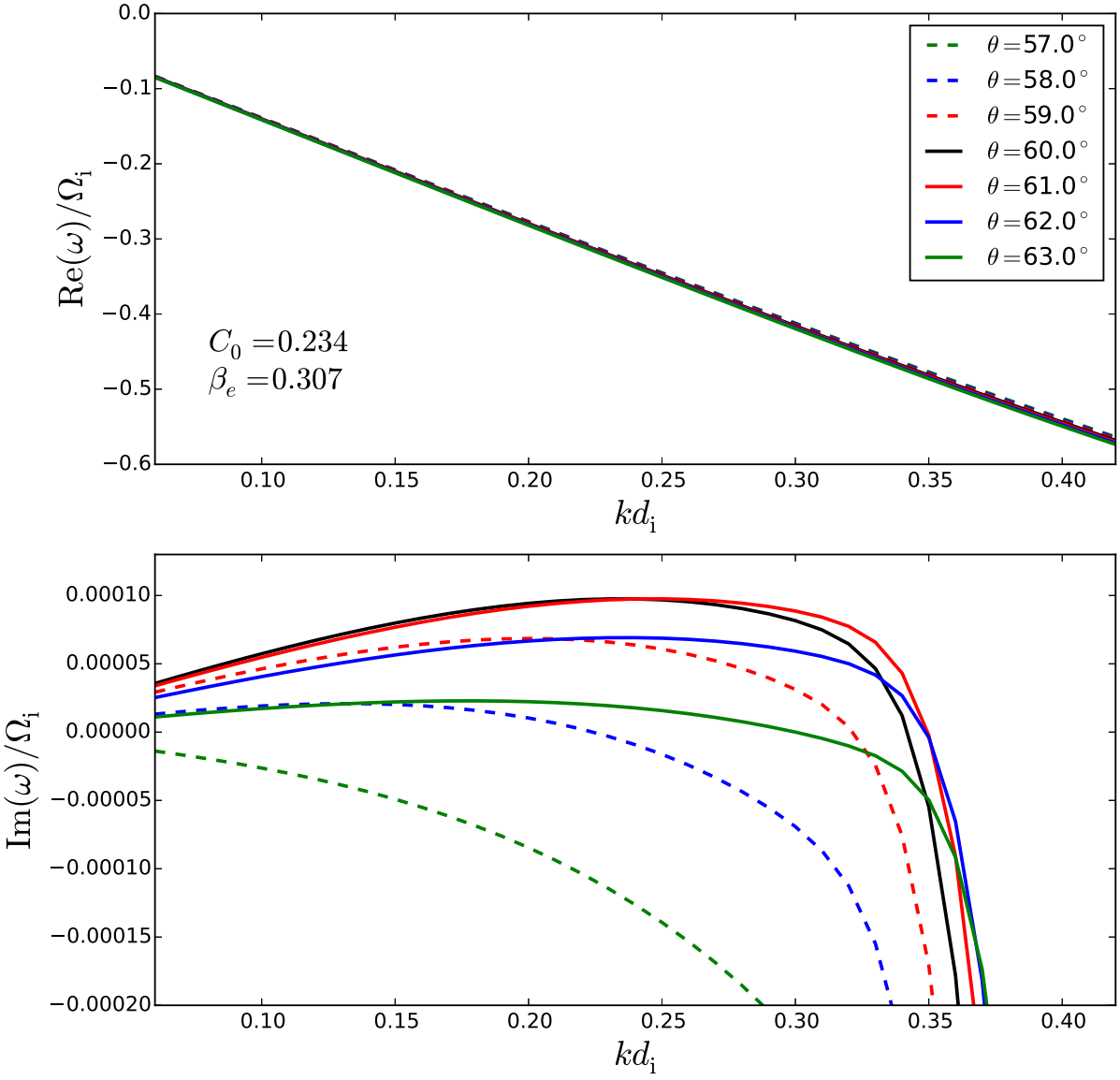

Figure 18: *Magnetosonic.* Real (upper) and imaginary (lower) parts of the magnetosonic dispersion relation, shown for different electron betas (β_e). We set $\beta_e = 0.307$ and $C_0 = 0.234$ for all calculations, but vary the propagation angle θ. The distribution is unstable in the range $58^\circ \lesssim \theta \lesssim 63^\circ$, and is maximally unstable at $\theta \approx 60^\circ$.

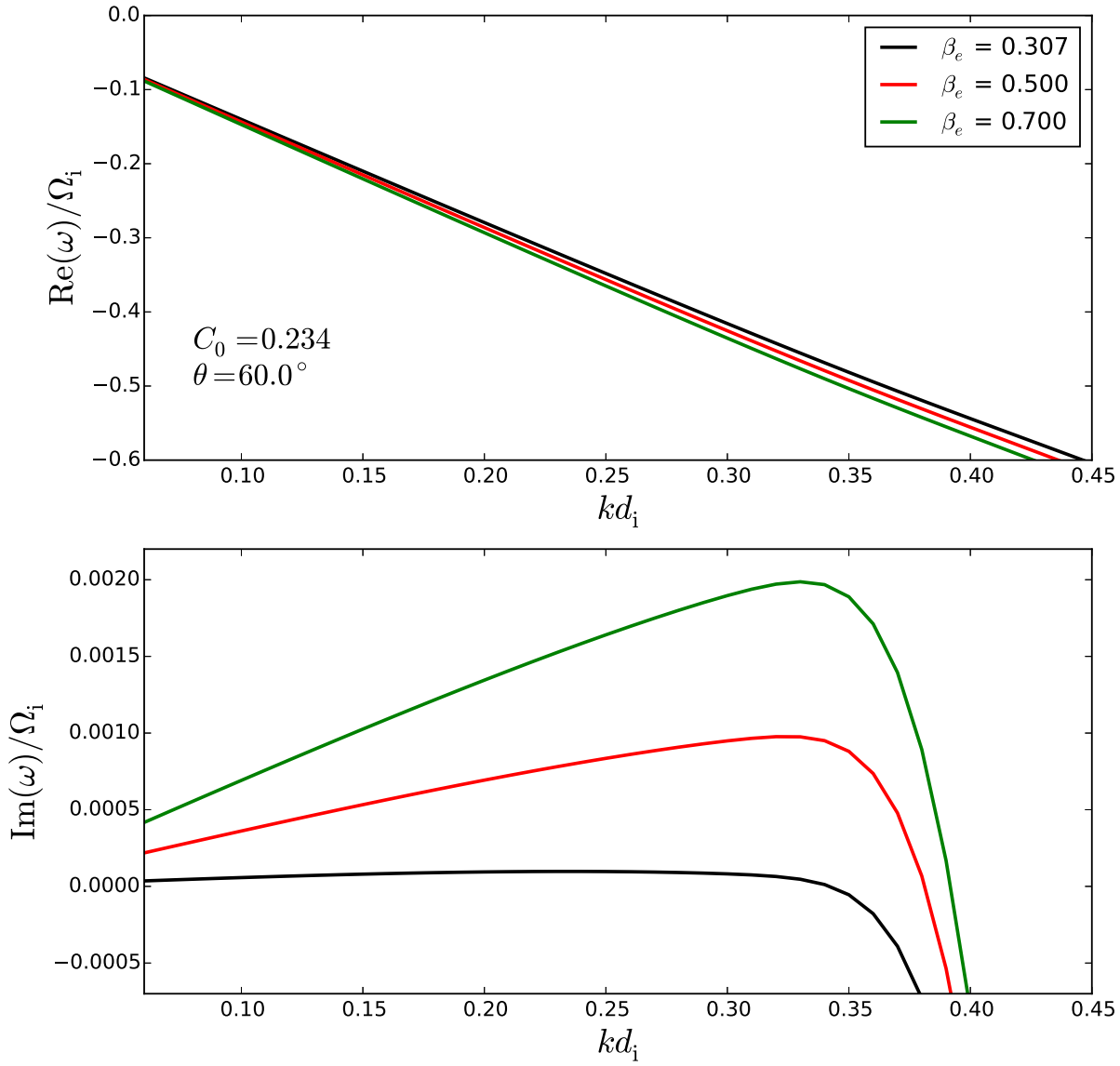

Figure 19: *Magnetosonic.* Real (upper) and imaginary (lower) parts of the magnetosonic dispersion relation, shown for different electron betas β_e. We set $\theta = 60°$ and $C_0 = 0.234$ for all calculations, but vary the electron beta β_e. The distribution is unstable in the range $0.3 \lesssim \beta_e \lesssim 0.7$, with monotonically increasing growth as β_e increases in this range.

dispersion relations derived from the core-halo-strahl function with those of the foregoing core-strahl model. Rather than conduct an in-depth analysis, we assume some representative halo function with fixed parameters, so as not to introduce any new free parameters to our model.

We will represent the core and strahl distributions by Eqs. 4.4 and 4.5, as elsewhere in this paper. Let us then model the halo distribution $f_h(\mu, v)$ as an isotropic kappa function (e.g., 43; 76):

$$f_h(\mu, v) = A_h \Big[1 + \frac{m_e v^2}{(2\kappa - 3)T_h}\Big]^{(-\kappa-1)}, \tag{4.16}$$

where m_e is the electron mass, and A_h is defined:

$$A_h = n_h \Big[\frac{m_e}{\pi(2\kappa - 3)T_h}\Big]^{(3/2)} \frac{\Gamma(\kappa + 1)}{\Gamma(\kappa - 1/2)}, \tag{4.17}$$

where $\Gamma()$ is the gamma function. Table 4 lists our fiducial values for the density n_h, temperature T_h, and kappa parameter κ that appear in Eqs. 4.16 and 4.17.

In Figs. 20-23, we compare the dispersion relations for the core-strahl model (solid lines) with those found for the core-halo-strahl model (dashed lines). In all plots, we see that $Re(\omega)$ for the wavemodes is not changed significantly, while the $Im(\omega)$ is made slightly more negative due to the damping introduced by the halo.

For the KAW mode, as plotted in Figs. 20, 21, the character of the instabilities are not significantly altered by the inclusion of the halo. Naturally, the extra damping in the core-halo-strahl case slightly narrows the range of angles over which the instability

n_h	$n_c/10$
T_h	61.05 eV
κ	5

Table 4: Here we present the set of physical constants, that appear in Eqs. 4.16 and 4.17, that specify our halo model.

exists.

Inclusion of the halo component has a more noticeable effect on the magnetosonic mode in a $\beta_e = 0.307$ plasma, see Fig. 22. We see that the damping introduced by the halo is significant enough to stabilize this mode at this particular β_e. However, the magnetosonic instability still exists at higher β_e (i.e. at $\beta_e \gtrsim 0.5$), as we can see from Fig. 23. The halo damping thus has the effect of pushing the instability to a slightly different regime in β_e.

As for the core-strahl case, we find that the whistler mode is stable for our core-halo-strahl eVDF.

4.6 Discussion and Conclusions

We here summarize our main results:

1. We analyzed the kinetic stability of a core-strahl eVDF, using a realistic distribution function that is representative of the typical fast solar wind at 1 AU. In agreement with (20), we observe the eVDF is unstable to the magnetosonic and KAW modes in the range of wavenumbers $kd_i \lesssim 1$. These modes are driven by the Landau resonance with the core electrons, i.e. at parallel velocities $v_\parallel = Re(\omega)/k_\parallel \sim (-v_A)$. The negative sign here indicates that the resonant electrons are traveling slightly sunward, relative to the proton bulk flow. In fact, this resonant velocity falls somewhere between the peaks

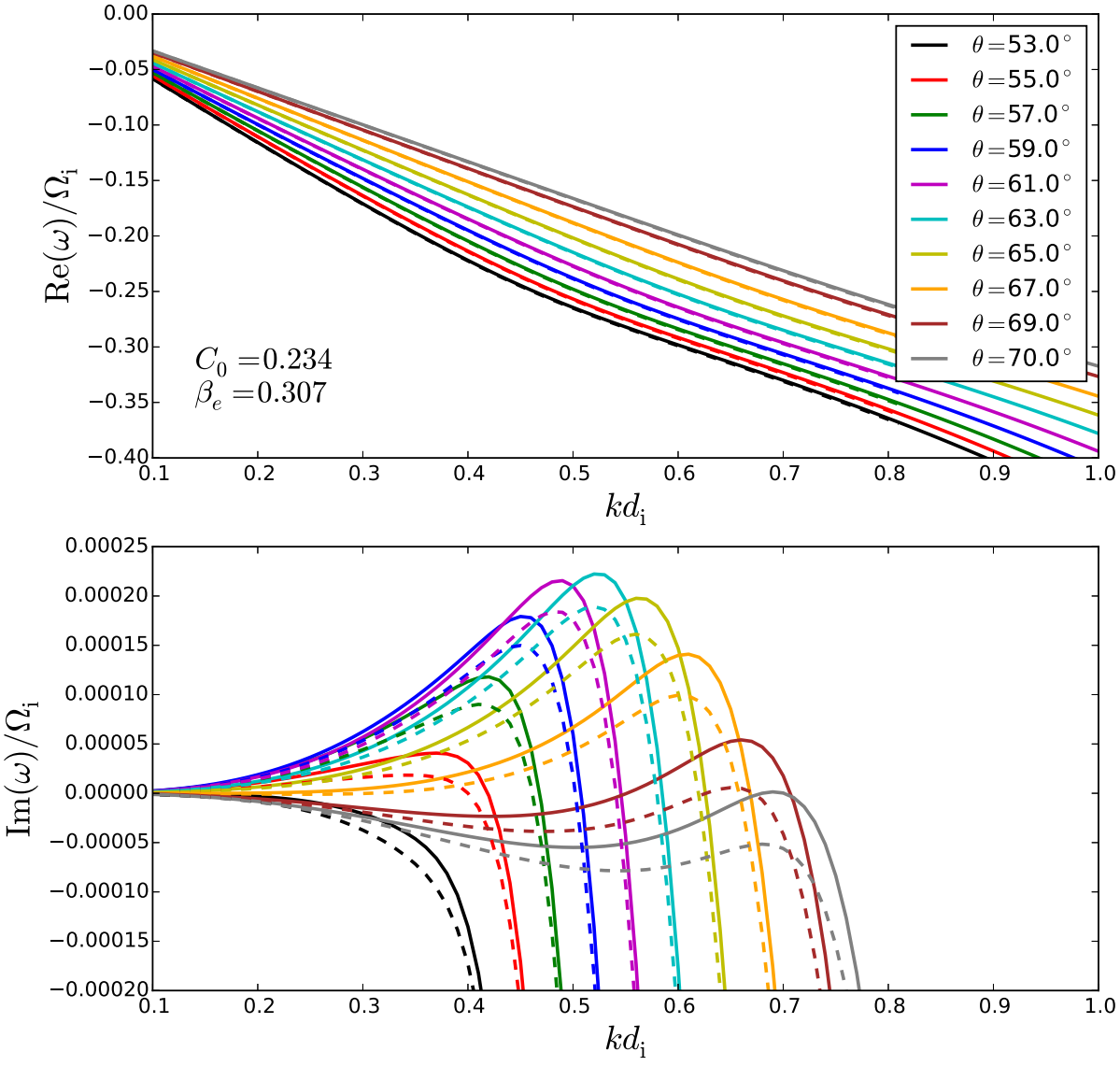

Figure 20: *KAW—Less oblique.* Dispersion relations for the original core-strahl model (solid lines, from Fig. 14) and the core-halo-strahl model (dashed lines) described in this section.

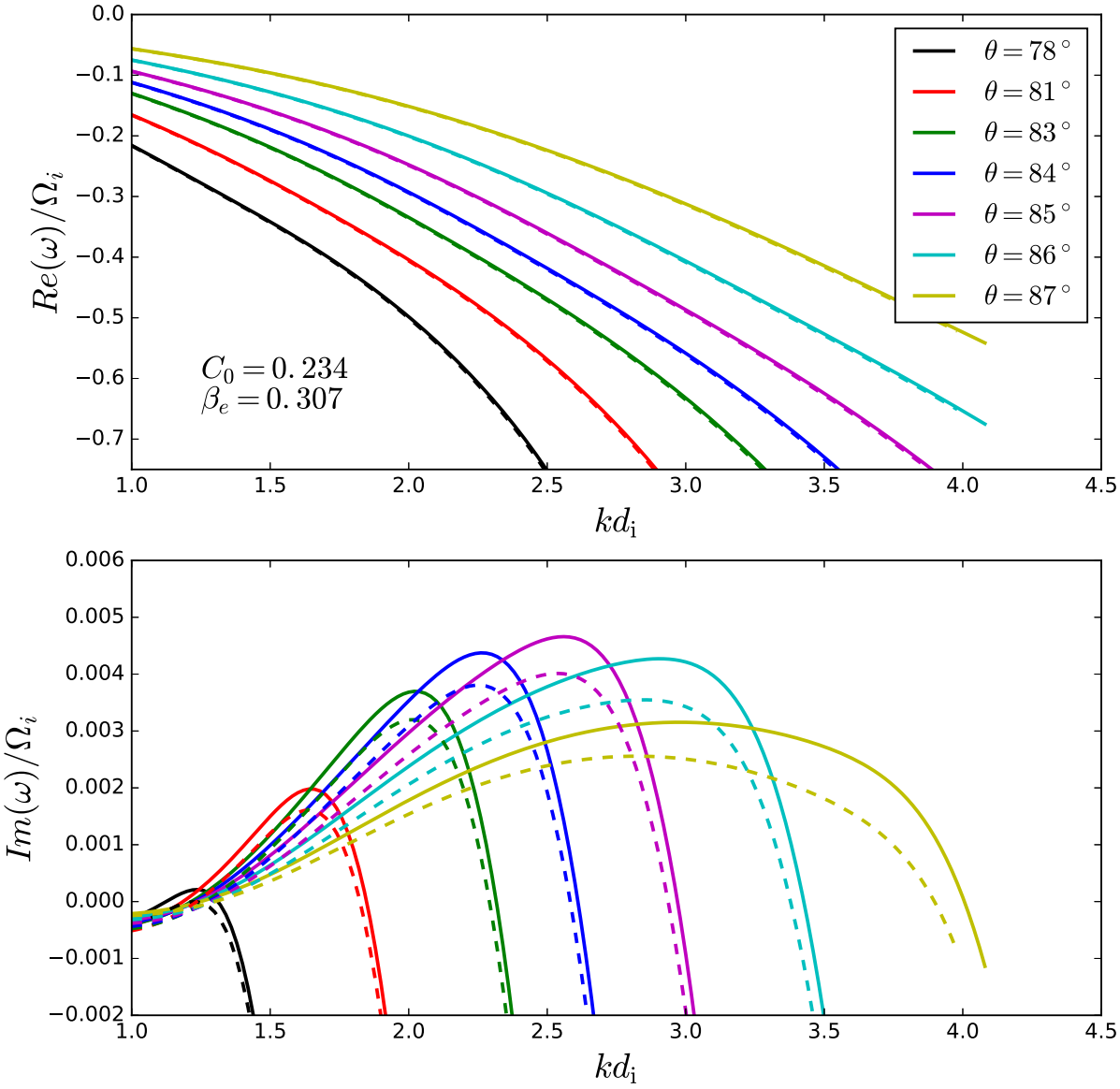

Figure 21: *KAW—More oblique.* Dispersion relations for the original core-strahl model (solid lines, from Fig. 16) and the core-halo-strahl model (dashed lines) described in this section.

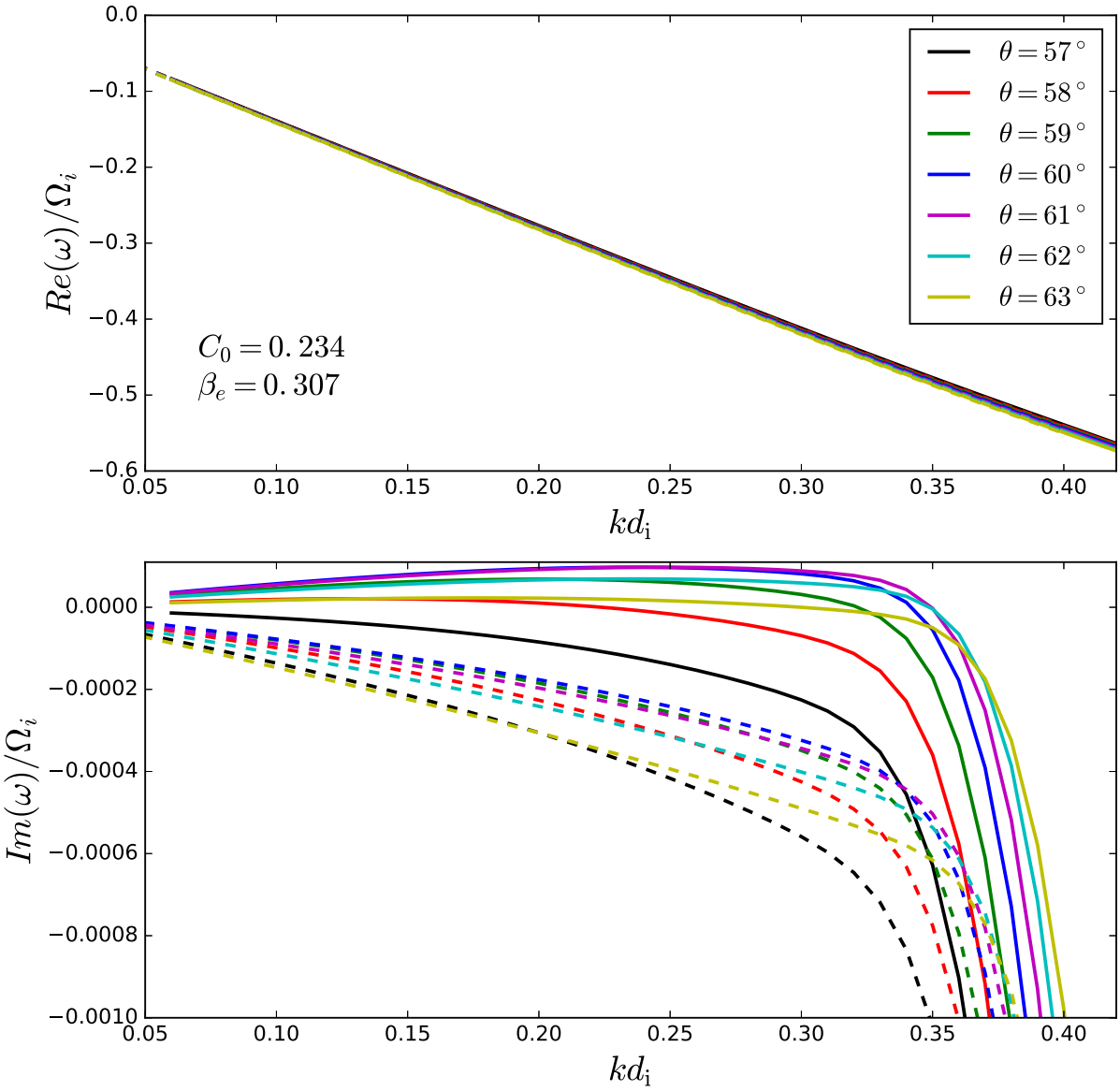

Figure 22: *Magnetosonic.* Dispersion relations for the original core-strahl model (solid lines, from Fig. 18) and the core-halo-strahl model (dashed lines) described in this section.

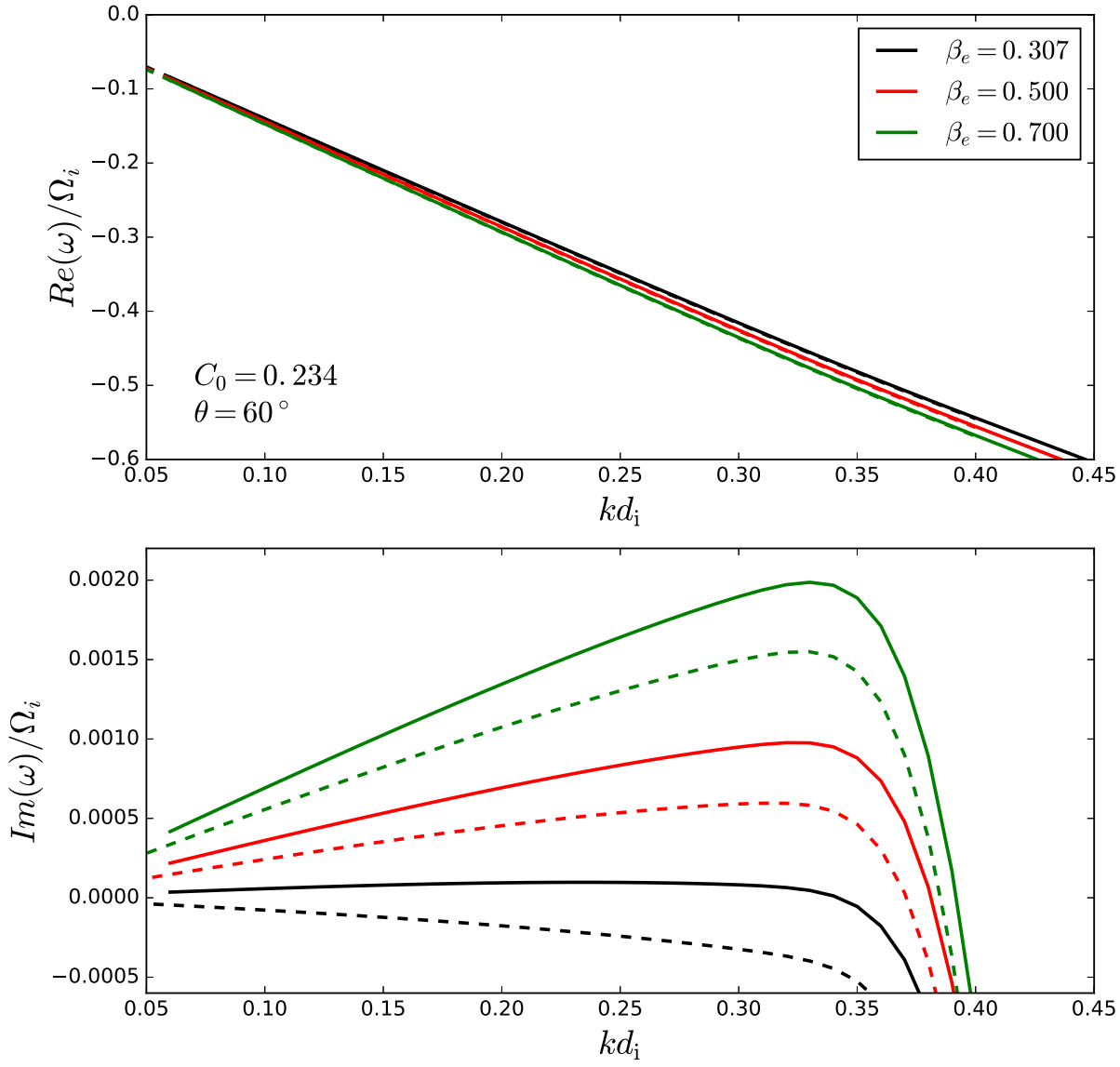

Figure 23: *Magnetosonic*. Dispersion relations for the original core-strahl model (solid lines, from Fig. 19) and the core-halo-strahl model (dashed lines) described in this section.

of the electron and ion VDFs. These results may be fairly insensitive to the particular model used for the core distribution—we note that (19) found similar waves and resonances for a core distribution that was non-Maxwellian, i.e. a Maxwellian distorted by a Spitzer-Härm electric field (71).

2. Our linear theory analysis does not yield a whistler instability. This begs comparison with the results of (22), in which a whistler heat flux instability could be excited by a skewed non-thermal eVDF. The difference is likely due to the fact that our model describes a core-strahl rather than a core-halo distribution. That is, the suprathermal heat-flux carrying electrons are modeled by Eq. (4.5), rather than by a drifting Maxwellian (or other function that is isotropic in its own frame).

The cases where the direct observation of whistler waves has been associated with a large electron heat flux appear to be limited to the slow wind, where the strahl tends to be less prominent (see figures 5 and 9, 38). We propose that further investigation of these events could reveal the presence of a drifting halo; however, to our knowledge such a study has not yet been undertaken.

In the cases where the heat flux is mostly accounted for by the electron strahl, on the other hand, our present work suggests that a large electron heat flux does not necessarily trigger a whistler instability. As a large heat flux is typically associated with a prominent strahl (e.g., 55), caution must be used when parametrizing the stability of the eVDF in terms of the heat flux, so that the physics of core-halo and core-strahl distributions are not confounded.

3. Remarkably, the observed instability thresholds at $C_0 \sim 0.2$ appear very close to the average strahl amplitude $C_0 = 0.234$ observed (Table 1), for the $\tilde{\gamma} = 0.75$ fast wind. This indicates that the strahl amplitude may be regulated by the instabilities, as has

been suggested by other authors. We note that the peak growth rates of the instabilities detected here, with $Im(\omega)/\Omega_i > 10^{-4}$, are just fast enough to be relevant for the solar wind strahl. That is, a typical strahl particle traveling as speed 10^4 km/sec at 1 AU, where the local ion cyclotron frequency is $\Omega_i \sim 1$ Hz, traverses a typical scale height ($\sim$1 AU) in a time $\sim 10^4/\Omega_i$. However, since the observed magnetosonic and KAW modes do not resonate directly with the strahl, we must assume that they could only regulate the strahl amplitude by some indirect mechanism (see also, 75).

When strong turbulence of moderately oblique kinetic Alfvén and magnetosonic modes is generated at scales $kd_i \lesssim 1$, it can produce whistler fluctuations at the scale $kd_i \sim 1$. These nonlinear fluctuations could then cascade into moderately oblique whistlers at even smaller scales, where they can interact with the strahl electrons, providing their "anomalous" scattering via the cyclotron resonance. This mechanism may also provide an explanation for the moderately oblique whistler-like fluctuations observed in the solar wind by (47).

Appendix A

Glossary

- **Anomalous Diffusion**: The idea that an additional physical effect, beyond Coulomb collisions, may contribute significant pitch angle scattering to the strahl population.
- **AU**: Astronomical Unit. The Earth and Sun are separated by a distance of exactly 1 AU.
- **Ecliptic**: The plane that contains Earth's orbital path around the Sun.
- **Electrostatic Analyzer (ESA)**: An instrument that directly samples the distribution function in a plasma by counting particles one at a time. An ESA uses electrostatic forces to admit only particles that have a specified energy to the instrument's detector.
- **eVDF**: Electron Velocity Distribution Function. This typically refers to a direct measurement of the electron distribution $f(\mathbf{v})$ in the solar wind.
- **Geocentric Solar Ecliptic (GSE) Coordinates**: A Cartesian coordinate system where the $\hat{\mathbf{x}}$ direction points from the Earth to the Sun, $\hat{\mathbf{z}}$ points perpendicular to the ecliptic (roughly aligned with the North Pole), and $\hat{\mathbf{y}} = \hat{\mathbf{z}} \times \hat{\mathbf{x}}$. GSE spherical coordinates may be defined accordingly.

- **Heliosphere**: A bubble-like region that is carved out of interstellar space, where the solar wind has a significant influence. The "inner heliosphere" refers to heliospheric distances less than 1 AU, while the "outer heliosphere" refers to distances greater than 1 AU.

- **Suprathermal**: This phrase is used to refer to particles that are not part of the thermal (core) part of the distribution—in the solar wind, the main suprathermal electron populations are the halo and strahl.

- **SWE**: Solar Wind Experiment. This refers to a suite of instruments onboard the Wind satellite that measured the solar wind's properties at 1 AU. The strahl detector, an electrostatic analyzer used widely in chapter 3, was part of this suite.

Appendix B

Definitions and Identities

B.1 Variables and Parameters

$$\mu = \cos\theta = \frac{\mathbf{v}\cdot\hat{\mathbf{B}}}{v} \tag{B.1}$$

$$K = \frac{m_e v^2}{2} \tag{B.2}$$

$$\xi = \frac{v^2}{v_{th}^2} \tag{B.3}$$

$$M(\mu, v, x) = \frac{(1-\mu^2)v^2}{B(x)} \tag{B.4}$$

$$E(v, x) = v^2 + \frac{2e\phi(x)}{m_e} \tag{B.5}$$

$$v_{th} = \sqrt{\frac{2T}{m_e}} \tag{B.6}$$

$$F(\mathbf{v}/v_{th}) = \frac{v_{th}^3 f(\mathbf{v})}{n}. \tag{B.7}$$

$$\lambda_{mfp} = \frac{T^2}{2\pi e^4 \Lambda n} \tag{B.8}$$

$$\tilde{\gamma} = \frac{T^2}{2\pi e^4 \Lambda n r} = \frac{\lambda_{mfp}}{r} \tag{B.9}$$

$$\beta = \frac{1 + Z_{eff}}{2} \approx 1.05 \tag{B.10}$$

$$\beta_e = \frac{8\pi n T}{B^2} \tag{B.11}$$

$$\Omega = -\frac{1}{\beta\sqrt{1 + (r/r_{45})^2}}. \tag{B.12}$$

$$\Omega_i = \frac{eB}{m_p c} \tag{B.13}$$

$$v_A = \frac{B}{\sqrt{4\pi n m_p}} \tag{B.14}$$

$$d_i = \frac{v_A}{\Omega_i} \tag{B.15}$$

B.2 Moments

$$n \equiv \int f(\mathbf{v}) d^3v \tag{B.16}$$

$$\mathbf{J} \equiv \int \mathbf{v} f(\mathbf{v}) d^3v \tag{B.17}$$

$$T \equiv \frac{m_e}{3n} \int v^2 f(\mathbf{v}) d^3v \tag{B.18}$$

$$\mathbf{q} \equiv \frac{m_e}{2} \int \mathbf{v} v^2 f(\mathbf{v}) d^3v \tag{B.19}$$

Appendix C

Derivations

C.1 Drift Kinetic Equation

In magnetized plasmas, as are frequently observed in astrophysical systems, the charged particles are constrained to spiral around the local magnetic field. This cyclotron motion reduces the effective number of velocity degrees of freedom, as compared to an unmagnetized plasma. It these circumstances, one can average over the particles' cyclotron motion to derive the so-called "drift kinetic equation" (37). The velocity space can be parametrized in terms of the speed v and magnetic moment μ_B, so that the drift kinetic equation describing $f(\mathbf{x}, \mu_B, v, t)$ can be expressed in the form:

$$\frac{\partial f}{\partial t} + (\mathbf{U_d} + v_\parallel \hat{b}) \cdot \nabla f - \left(\hat{b} \cdot \frac{D\mathbf{U_d}}{Dt} - \mu_B B \nabla \cdot \hat{b} - \frac{q_e}{m} E_\parallel \right) \frac{\partial f}{\partial v_\parallel} = \hat{C}(f) \tag{C.1}$$

Here μ_B is the magnetic moment, defined as:

$$\mu_B \equiv \frac{{v_\perp}^2}{2B}, \tag{C.2}$$

and $\mathbf{U_d}$ represents the $\mathbf{E} \times \mathbf{B}$ drift,

$$\mathbf{U_d} \equiv \frac{c\mathbf{E} \times \mathbf{B}}{B^2}, \tag{C.3}$$

and $\frac{D}{Dt}$ is a shorthand for the expression,

$$\frac{D}{Dt} \equiv \frac{\partial}{\partial t} + (\mathbf{U_d} + \hat{b}v_\parallel) \cdot \nabla. \tag{C.4}$$

The Coulomb collision operator, which is often neglected under the assumption of a collisionless plasma, is included on the RHS of equation C.1. We note that although the collision operator is derived for the kinetic equation describing an unmagnetized plasma, the same operator can be applied to the drift kinetic equation for magnetized plasmas, as long as the particle gyrorbits can be well approximated by straight-line trajectories over the scale of a Debye sphere. This condition amounts to the requirement that the electron Larmor radius be much larger than the Debye length. This condition is well-satisfied in the solar wind, where at 1 AU the typical Debye sphere measures a few meters across and the thermal electron gyroradius is on the order of kilometers.

We will consider the drift kinetic equation for electron motion: $m = m_e$, $q_e = -e$. When the drifts can be ignored ($|v_\parallel| \gg |\mathbf{U_d}|$), equation C.1 reduces to the form:

$$\frac{\partial f}{\partial t} + v_\parallel \hat{b} \cdot \nabla f + \Big(\mu_B B \nabla \cdot \hat{b} - \frac{eE_\parallel}{m}\Big)\frac{\partial f}{\partial v_\parallel} = \hat{C}(f). \tag{C.5}$$

Note that because all gradients enter into equation C.1 as $\hat{b} \cdot \nabla$, the only relevant spatial dimension is the distance along a field line, and we denote this distance as x. The drift kinetic equation for the distribution function $f(x, \mu_B, v_\parallel, t)$ can be expressed as:

$$\frac{\partial f}{\partial t} + v_\parallel \frac{\partial f}{\partial x} + \Big(- \mu_B B \frac{d \ln B}{dx} - \frac{eE_\parallel}{m}\Big)\frac{\partial f}{\partial v_\parallel} = \hat{C}(f). \tag{C.6}$$

However, it is more convenient for us to adopt the speed v and cosine of the pitch angle $\mu = v_\parallel / v$ as velocity space variables. Let us then rewrite the distribution function

as $f^*(x,\mu,v,t) = f(x,\mu_B,v_\parallel,t)$, where $\mu = \mu(x,\mu_B,v_\parallel)$ and $v = v(x,\mu_B,v_\parallel)$. The new independent variables v, and μ are related to the previous set of variables as follows:

$$v(x,\mu_B,v_\parallel) = [2B(x)\mu_B + v_\parallel^2]^{1/2} \tag{C.7}$$

$$\mu(x,\mu_B,v_\parallel) = v_\parallel[2B(x)\mu_B + v_\parallel^2]^{-1/2} \tag{C.8}$$

To change variables, we substitute f^* into equation C.6 and apply the chain rule. This requires us to evaluate the derivatives df^*/dx and $df^*/dv_\parallel$:

$$\begin{aligned}
\frac{df^*}{dx} &= \frac{\partial f^*}{\partial x} + \frac{\partial v}{\partial x}\frac{\partial f^*}{\partial v} + \frac{\partial \mu}{\partial x}\frac{\partial f^*}{\partial \mu} \\
&= \frac{\partial f^*}{\partial x} + \frac{B'(x)\mu_B}{[2B(x)\mu_B + v_\parallel^2]^{1/2}}\frac{\partial f^*}{\partial v} - \frac{B'(x)\mu_B v_\parallel}{[2B(x)\mu_B + v_\parallel^2]^{3/2}}\frac{\partial f^*}{\partial \mu} \\
&= \frac{\partial f^*}{\partial x} + \frac{v(1-\mu^2)}{2}\frac{d\ln B}{dx}\frac{\partial f^*}{\partial v} - \frac{\mu(1-\mu^2)}{2}\frac{d\ln B}{dx}\frac{\partial f^*}{\partial \mu}
\end{aligned} \tag{C.9}$$

$$\begin{aligned}
\frac{df^*}{dv_\parallel} &= \frac{\partial v}{\partial v_\parallel}\frac{\partial f^*}{\partial v} + \frac{\partial \mu}{\partial v_\parallel}\frac{\partial f^*}{\partial \mu} \\
&= \frac{v_\parallel}{[2B(x)\mu_B + v_\parallel^2]^{1/2}}\frac{\partial f^*}{\partial v} + \Big\{[2B(x)\mu_B + v_\parallel^2]^{-1/2} - \frac{v_\parallel^2}{[2B(x)\mu_B + v_\parallel^2]^{3/2}}\Big\}\frac{\partial f^*}{\partial \mu} \\
&= \mu\frac{\partial f^*}{\partial v} + \frac{(1-\mu^2)}{v}\frac{\partial f^*}{\partial \mu}
\end{aligned} \tag{C.10}$$

Substituting equations C.9 and C.10 into equation C.6 and simplifying, we arrive at the drift kinetic equation for electron distribution $f(x,\mu,v,t)$ (dropping the $*$ superscript):

$$\frac{\partial f}{\partial t} + \mu v\frac{\partial f}{\partial x} - \frac{1}{2}\frac{d\ln B}{dx}v(1-\mu^2)\frac{\partial f}{\partial \mu} - \frac{eE_\parallel}{m}\Big[\frac{1-\mu^2}{v}\frac{\partial f}{\partial \mu} + \mu\frac{\partial f}{\partial v}\Big] = \hat{C}(f) \tag{2.2}$$

C.2 The Coulomb Collision Operator

Let us denote as $\hat{C}(f_\alpha)$ the kinetic operator that encompasses the combined effect of Coulomb collisions on the population α:

$$\hat{C}(f_\alpha) = \sum_\beta \hat{C}(f_\alpha, f_\beta). \tag{C.11}$$

In equation C.11, the sum is conducted over all particle populations (indexed by β), and includes a self-collision term ($\beta = \alpha$). In equation C.11, we introduce the notation $\hat{C}(f_\alpha, f_\beta)$, which represents the effect of Coulomb collisions on a test particle population f_α as it interacts with a field population f_β.

We will adopt the results of classical kinetic theory, in which the collision operator $\hat{C}(f_\alpha, f_\beta)$ is a non-linear integro-differential operator, that describes velocity-space diffusion that arises from many small-angle collisions. Large-angle collisions, which occur between particles that approach each other with very small impact parameter, may be ignored to first forder (41). The collision operator has many equivalent representationsm, including the well-known *Landau form*, which is shown here for its relative compactness:

$$\hat{C}(f_\alpha, f_\beta) \equiv \frac{2\pi q_\alpha^2 q_\beta^2 \Lambda_{\alpha\beta}}{m_\alpha} \frac{\partial}{\partial v_j} \int \left\{ \frac{1}{m_\alpha} f_\beta(\mathbf{v}') \frac{\partial f_\alpha(\mathbf{v})}{\partial v_i} - \frac{1}{m_\beta} f_\alpha(\mathbf{v}) \frac{\partial f_\beta(\mathbf{v}')}{\partial v_i'} \right\} \frac{\delta_{ij} u^2 - u_i u_j}{u^3} d^3 v'. \tag{C.12}$$

In equation C.12, the charges and masses of the test and field populations are denoted by q_α, q_β and m_α, m_β, respectively. The velocity $\mathbf{u}$ is defined as:

$$\mathbf{u} \equiv \mathbf{v} - \mathbf{v}', \tag{C.13}$$

and $\Lambda_{\alpha\beta}$ is the well-known "Coulomb logarithm" (34). We will treat the Coulomb logarithm as a constant, that is approximately the same for e-e and e-i collisions:

$$\Lambda_{ee}, \Lambda_{ei} \approx \Lambda \equiv const. \tag{C.14}$$

C.2.1 Linearized Collision Operator

The linearized form of $\hat{C}(f_\alpha, f_\beta)$ can be obtained by decomposing the particle distributions for two species α and β into Maxwellian and non-Maxwellian parts: $f_\alpha = f_{\alpha M} + \delta f_\alpha$, $f_\beta = f_{\beta M} + \delta f_\beta$. Here it is assumed that the deviations δf_α and δf_β are tenuous relative to the background Maxwellians. Substituting these expressions into equation C.12 leads to the following expansion of $\hat{C}(f_\alpha, f_\beta)$, which follows from the "bilinearity" of the collision operator C.12:

$$\hat{C}(f_\alpha, f_\beta) = \hat{C}(f_{\alpha M}, f_{\beta M}) + \hat{C}(\delta f_\alpha, f_{\beta M}) + \hat{C}(f_{\alpha M}, \delta f_\beta) + \hat{C}(\delta f_\alpha, \delta f_\beta). \tag{C.15}$$

In the physical scenario where δf_α represents a tenuous beam of particles that is well-separated from the background Maxwellian(s), we may approximate the collision integral in the velocity regime where the beam dominates (where $f_\alpha \approx \delta f_\alpha$) by the leading term $\hat{C}(\delta f_\alpha, f_{\beta M})$. This term, which represents the interaction of δf_α with the Maxwellian field population $f_{\beta M}$ (68; 29), can be written as follows:

$$\begin{aligned} \hat{C}(f_\alpha, f_\beta) &\approx \hat{C}(\delta f_\alpha, f_{\beta M}) \\ &= \nu_D^{\alpha\beta} \mathcal{L}(\delta f_\alpha) + \frac{1}{v^2}\frac{\partial}{\partial v}\Big\{ v^3 \Big(\frac{m_\alpha}{(m_\alpha + m_\beta)} \nu_s^{\alpha\beta}(\delta f_\alpha) + \frac{1}{2}\nu_\parallel^{\alpha\beta} v \frac{\partial(\delta f_\alpha)}{\partial v} \Big) \Big\}. \end{aligned} \tag{C.16}$$

This exact expression C.16 arises from substituting an arbitrary test population δf_α and an isotropic Maxwellian field population $f_{\beta M}$ with thermal speed $v_{th,\beta}$ (centered at $\mathbf{v} = 0$) into equation C.12. Here we introduced $\mathcal{L}$, the Lorentz collision operator:

$$\begin{aligned}\mathcal{L} &= \frac{1}{2}\Big\{\frac{\partial}{\partial\mu}(1-\mu^2)\frac{\partial}{\partial\mu} + \frac{1}{1-\mu^2}\frac{\partial^2}{\partial\phi^2}\Big\} \\ &= \frac{1}{2}\frac{\partial}{\partial\mu}(1-\mu^2)\frac{\partial}{\partial\mu},\end{aligned} \tag{C.17}$$

where it is assumed the distributions are gyrotropic ($\partial f_\alpha/\partial\phi = 0$). The coefficients $\nu_D^{\alpha\beta}(v)$, $\nu_s^{\alpha\beta}(v)$, and $\nu_\parallel^{\alpha\beta}(v)$ represent the characteristic rates of perpendicular velocity diffusion, frictional slowing, and parallel energy exchange, respectively. The exact velocity-dependent expressions, which depend on the error function $\mathrm{erf}(v/v_{th,\beta})$, for these coefficients can be found in reference (29). In the high-speed regime relevant to the strahl, $v \gg v_{th,\beta}$, we can approximate $\mathrm{erf}(v/v_{th,\beta}) \approx 1$ and the various terms of equation C.16 reduce to the following expressions:

$$\nu_D^{\alpha\beta}(v)\mathcal{L}(\delta f_\alpha) \approx \frac{2\pi n_\beta q_\alpha^2 q_\beta^2 \Lambda_{\alpha\beta}}{m_\alpha^2 v^3}\frac{\partial}{\partial\mu}(1-\mu^2)\frac{\partial}{\partial\mu}(\delta f_\alpha) \tag{C.18}$$

$$\frac{m_\alpha}{(m_\alpha+m_\beta)}\frac{1}{v^2}\frac{\partial}{\partial v}\Big\{v^3\nu_s^{\alpha\beta}(v)(\delta f_\alpha)\Big\} \approx \frac{4\pi n_\beta q_\alpha^2 q_\beta^2 \Lambda_{\alpha\beta}}{m_\alpha m_\beta v^2}\frac{\partial}{\partial v}(\delta f_\alpha) \tag{C.19}$$

$$\frac{1}{v^2}\frac{\partial}{\partial v}\Big\{\frac{1}{2}\nu_\parallel^{\alpha\beta} v\frac{\partial(\delta f_\alpha)}{\partial v}\Big\} \approx \frac{2\pi n_\beta q_\alpha^2 q_\beta^2 \Lambda_{\alpha\beta} v_{th,\beta}^2}{m_\alpha^2}\Big\{-\frac{1}{v^4}\frac{\partial}{\partial v}(\delta f_\alpha) + \frac{1}{v^3}\frac{\partial^2}{\partial^2 v}(\delta f_\alpha)\Big\} \tag{C.20}$$

Using these expressions, the collision operator (eq. C.16) for the electron distribution function f (in the high-velocity regime where $\delta f_e \approx f$) takes the form:

$$\begin{aligned}\hat{C}(f) &= \hat{C}(f, f_{eM}) + \sum_i \hat{C}(f, f_{iM}) \\ &= \frac{4\pi n_e e^4 \Lambda}{m_e^2}\left[\frac{\beta}{v^3}\frac{\partial}{\partial\mu}(1-\mu^2)\frac{\partial f}{\partial\mu} + \frac{1}{v^2}\frac{\partial f}{\partial v} + \frac{v_{th,e}^2}{2v^2}\left(-\frac{1}{v^2}\frac{\partial f}{\partial v} + \frac{1}{v}\frac{\partial^2 f}{\partial v^2}\right)\right].\end{aligned} \tag{C.21}$$

Equation C.21 takes into account the interaction of the electrons with all ion species; the letter "i" in the sum indexes the ion species. The ions are electrons are assumed to have similar temperatures $T_e \approx T_i$, which allowed terms that are small to first order in the parameter

$$\left(\frac{v_{th,i}}{v_{th,e}}\right)^2 \approx \frac{m_e}{m_i} \ll 1, \tag{C.22}$$

to be neglected. The expression β appears as a coefficient which characterizes the pitch-angle diffusion amplitude, and is defined as:

$$\beta \equiv (1 + Z_{eff})/2. \tag{C.23}$$

Here, Z_{eff}, the "effective charge" of the ions (57), is defined:

$$Z_{eff} \equiv \frac{\sum_i n_i Z_i^2}{\sum_i n_i Z_i}. \tag{C.24}$$

In equation C.24, n_i and Z_i refer respectively to the number density and charge state of ion species i.

Bibliography

[1] M. R. Aellig, A. J. Lazarus, and J. T. Steinberg, *The solar wind helium abundance: Variation with wind speed and the solar cycle*, Geophys. Res. Lett., 28 (2001), pp. 2767–2770.

[2] B. R. Anderson, R. M. Skoug, J. T. Steinberg, and D. J. McComas, *Variability of the solar wind suprathermal electron strahl*, Journal of Geophysical Research (Space Physics), 117 (2012), p. A04107.

[3] P. Astfalk and F. Jenko, *LEOPARD: A grid-based dispersion relation solver for arbitrary gyrotropic distributions*, Journal of Geophysical Research (Space Physics), 122 (2017), pp. 89–101.

[4] S. D. Bale, M. Pulupa, C. Salem, C. H. K. Chen, and E. Quataert, *Electron Heat Conduction in the Solar Wind: Transition from Spitzer-Härm to the Collisionless Limit*, Astrophys. J. Lett., 769 (2013), p. L22.

[5] D. Biskamp, *Magnetohydrodynamic Turbulence*, July 2003.

[6] S. Boldyrev, K. Horaites, Q. Xia, and J. C. Perez, *Toward a Theory of Astrophysical Plasma Turbulence at Subproton Scales*, Astrophys. J., 777 (2013), p. 41.

[7] B. D. G. Chandran, T. J. Dennis, E. Quataert, and S. D. Bale, *Incorporating Kinetic Physics into a Two-fluid Solar-wind Model with Temperature*

Anisotropy and Low-frequency Alfvén-wave Turbulence, Astrophys. J., 743 (2011), p. 197.

[8] O. Chang, S. P. Gary, and J. Wang, *Whistler turbulence at variable electron beta: Three-dimensional particle-in-cell simulations*, Journal of Geophysical Research (Space Physics), 118 (2013), pp. 2824–2833.

[9] P. C. Clemmow and J. P. Dougherty, *Electrodynamics of Particles and Plasmas*, Addison-Wesley, 1969.

[10] G. Colonna, *Boltzmann and vlasov equations in plasma physics*, in Plasma Modeling, 2053-2563, IOP Publishing, 2016, pp. 1–1 to 1–23.

[11] L. L. Cowie and C. F. McKee, *The evaporation of spherical clouds in a hot gas. I - Classical and saturated mass loss rates*, Astrophys. J., 211 (1977), pp. 135–146.

[12] S. R. Cranmer, M. Asgari-Targhi, M. P. Miralles, J. C. Raymond, L. Strachan, H. Tian, and L. N. Woolsey, *The role of turbulence in coronal heating and solar wind expansion*, Philosophical Transactions of the Royal Society of London Series A, 373 (2015), pp. 20140148–20140148.

[13] C. A. de Koning, J. T. Gosling, R. M. Skoug, and J. T. Steinberg, *Energy dependence of electron pitch angle distribution widths in solar bursts*, Journal of Geophysical Research (Space Physics), 112 (2007), p. A04101.

[14] S. E. DeForest, *Spacecraft charging at synchronous orbit*, J. Geophys. Res., 77 (1972), p. 651.

[15] D. H. Fairfield and J. D. Scudder, *Polar rain - Solar coronal electrons in the earth's magnetosphere*, J. Geophys. Res., 90 (1985), pp. 4055–4068.

[16] W. C. Feldman, J. R. Asbridge, S. J. Bame, J. T. Gosling, and D. S. Lemons, *Characteristic electron variations across simple high-speed solar wind streams*, J. Geophys. Res., 83 (1978), pp. 5285–5295.

[17] W. C. Feldman, J. R. Asbridge, S. J. Bame, M. D. Montgomery, and S. P. Gary, *Solar wind electrons*, J. Geophys. Res., 80 (1975), pp. 4181–4196.

[18] R. J. Fitzenreiter, K. W. Ogilvie, D. J. Chornay, and J. Keller, *Observations of electron velocity distribution functions in the solar wind by the WIND Spacecraft: High angular resolution Strahl measurements*, Geophys. Res. Lett., 25 (1998), pp. 249–252.

[19] D. W. Forslund, *Instabilities associated with heat conduction in the solar wind and their consequences*, J. Geophys. Res., 75 (1970), p. 17.

[20] S. P. Gary, W. C. Feldman, D. W. Forslund, and M. D. Montgomery, *Heat flux instabilities in the solar wind*, J. Geophys. Res., 80 (1975), pp. 4197–4203.

[21] S. P. Gary, E. Neagu, R. M. Skoug, and B. E. Goldstein, *Solar wind electrons: Parametric constraints*, J. Geophys. Res., 104 (1999), pp. 19843–19850.

[22] S. P. Gary, E. E. Scime, J. L. Phillips, and W. C. Feldman, *The whistler heat flux instability: Threshold conditions in the solar wind*, J. Geophys. Res., 99 (1994), p. 23391.

[23] J. T. Gosling, M. F. Thomsen, S. J. Bame, and R. D. Zwickl, *The eastward deflection of fast coronal mass ejecta in interplanetary space*, J. Geophys. Res., 92 (1987), pp. 12399–12406.

[24] G. A. Graham, I. J. Rae, C. J. Owen, and A. P. Walsh, *Investigating the Effect of IMF Path Length on Pitch-angle Scattering of Strahl within 1 au*, Astrophys. J., 855 (2018), p. 40.

[25] G. A. Graham, I. J. Rae, C. J. Owen, A. P. Walsh, C. S. Arridge, L. Gilbert, G. R. Lewis, G. H. Jones, C. Forsyth, A. J. Coates, and J. H. Waite, *The evolution of solar wind strahl with heliospheric distance*, Journal of Geophysical Research (Space Physics), 122 (2017), pp. 3858–3874.

[26] A. V. Gurevich and Y. N. Istomin, *Thermal runaway and convective heat transport by fast electrons in a plasma*, Soviet Journal of Experimental and Theoretical Physics, 50 (1979), p. 470.

[27] C. M. Hammond, W. C. Feldman, D. J. McComas, J. L. Phillips, and R. J. Forsyth, *Variation of electron-strahl width in the high-speed solar wind: ULYSSES observations.*, Astronomy and Astrophysics, 316 (1996), pp. 350–354.

[28] P. Helander and D. J. Sigmar, *Collisional transport in magnetized plasmas*, 2002.

[29] S. P. Hirshman and D. J. Sigmar, *Approximate Fokker-Planck collision operator for transport theory applications*, Physics of Fluids, 19 (1976), pp. 1532–1540.

[30] K. Horaites, P. Astfalk, S. Boldyrev, and F. Jenko, *Stability analysis of core-strahl electron distributions in the solar wind*, MNRAS, 480 (2018), pp. 1499–1506.

[31] K. Horaites, S. Boldyrev, S. I. Krasheninnikov, C. Salem, S. D. Bale, and M. Pulupa, *Self-Similar Theory of Thermal Conduction and Application to the Solar Wind*, Physical Review Letters, 114 (2015), p. 245003.

[32] K. Horaites, S. Boldyrev, and M. V. Medvedev, *Electron strahl and halo formation in the solar wind*, MNRAS, 484 (2019), pp. 2474–2481.

[33] K. Horaites, S. Boldyrev, L. B. Wilson, III, A. F. Viñas, and J. Merka, *Kinetic Theory and Fast Wind Observations of the Electron Strahl*, MNRAS, 474 (2018), pp. 115–127.

[34] J. Huba, U. S. O. of Naval Research, and N. R. L. (U.S.), *NRL Plasma Formulary*, NRL publication, Naval Research Laboratory, 1998.

[35] P. Kajdič, O. Alexandrova, M. Maksimovic, C. Lacombe, and A. N. Fazakerley, *Suprathermal Electron Strahl Widths in the Presence of Narrow-band Whistler Waves in the Solar Wind*, Astrophys. J., 833 (2016), p. 172.

[36] S. I. Krasheninnikov, *Superthermal Particles and Electron Thermal Conductivity*, JETP, 67 (1988), pp. 2483–2486.

[37] R. M. Kulsrud, *MHD description of plasma*, in Basic Plasma Physics: Selected Chapters, Handbook of Plasma Physics, Volume 1 (North Holland Publishing Company, Amsterdam), A. A. Galeev and R. N. Sudan, eds., 1983, p. 1.

[38] C. Lacombe, O. Alexandrova, L. Matteini, O. Santolík, N. Cornilleau-Wehrlin, A. Mangeney, Y. de Conchy, and M. Maksimovic, *Whistler Mode Waves and the Electron Heat Flux in the Solar Wind: Cluster Observations*, Astrophys. J., 796 (2014), p. 5.

[39] D. S. Lemons and W. C. Feldman, *Collisional modification to the exospheric theory of solar wind halo electron pitch angle distributions*, J. Geophys. Res., 88 (1983), pp. 6881–6887.

[40] R. P. Lepping, M. H. Acũna, L. F. Burlaga, W. M. Farrell, J. A. Slavin, K. H. Schatten, F. Mariani, N. F. Ness, F. M. Neubauer, Y. C. Whang, J. B. Byrnes, R. S. Kennon, P. V. Panetta, J. Scheifele, and E. M. Worley, *The Wind Magnetic Field Investigation*, Space Sci. Res., 71 (1995), pp. 207–229.

[41] C.-K. Li and R. D. Petrasso, *Fokker-Planck equation for moderately coupled plasmas*, Physical Review Letters, 70 (1993), pp. 3063–3066.

[42] R. P. Lin, *WIND Observations of Suprathermal Electrons in the Interplanetary Medium*, Space Sci. Res., 86 (1998), pp. 61–78.

[43] M. Maksimovic, I. Zouganelis, J.-Y. Chaufray, K. Issautier, E. E. Scime, J. E. Littleton, E. Marsch, D. J. McComas, C. Salem, R. P. Lin, and H. Elliott, *Radial evolution of the electron distribution functions in the fast solar wind between 0.3 and 1.5 AU*, Journal of Geophysical Research (Space Physics), 110 (2005), p. 9104.

[44] C. B. Markwardt, *Non-linear Least-squares Fitting in IDL with MPFIT*, in Astronomical Data Analysis Software and Systems XVIII, D. A. Bohlender, D. Durand, and P. Dowler, eds., vol. 411 of Astronomical Society of the Pacific Conference Series, Sept. 2009, p. 251.

[45] E. Marsch and A. K. Richter, *HELIOS observational constraints on solar wind expansion*, J. Geophys. Res., 89 (1984), pp. 6599–6612.

[46] D. J. McComas, S. J. Bame, B. L. Barraclough, W. C. Feldman, H. O. Funsten, J. T. Gosling, P. Riley, R. Skoug, A. Balogh, R. Forsyth, B. E. Goldstein, and M. Neugebauer, *Ulysses' return to the slow solar wind*, Geophys. Res. Lett., 25 (1998), pp. 1–4.

[47] Y. Narita, R. Nakamura, W. Baumjohann, K.-H. Glassmeier, U. Motschmann, B. Giles, W. Magnes, D. Fischer, R. B. Torbert, C. T. Russell, R. J. Strangeway, J. L. Burch, Y. Nariyuki, S. Saito, and S. P. Gary, *On Electron-scale Whistler Turbulence in the Solar Wind*, Astrophys. J. Lett., 827 (2016), p. L8.

[48] K. W. Ogilvie, D. J. Chornay, R. J. Fritzenreiter, F. Hunsaker, J. Keller, J. Lobell, G. Miller, J. D. Scudder, E. C. Sittler, Jr., R. B. Torbert, D. Bodet, G. Needell, A. J. Lazarus, J. T. Steinberg, J. H. Tappan, A. Mavretic, and E. Gergin, *SWE, A Comprehensive Plasma Instrument for the Wind Spacecraft*, Space Sci. Res., 71 (1995), pp. 55–77.

[49] K. W. Ogilvie, R. Fitzenreiter, and M. Desch, *Electrons in the low-density solar wind*, J. Geophys. Res., 105 (2000), pp. 27277–27288.

[50] C. Pagel, S. P. Gary, C. A. de Koning, R. M. Skoug, and J. T. Steinberg, *Scattering of suprathermal electrons in the solar wind: ACE observations*, Journal of Geophysical Research (Space Physics), 112 (2007), p. A04103.

[51] E. N. Parker, *Dynamics of the Interplanetary Gas and Magnetic Fields.*, Astrophys. J., 128 (1958), p. 664.

[52] ——, *Dynamical Properties of Stellar Coronas and Stellar Winds. II. Integration of the Heat-Flow Equation.*, Astrophys. J., 139 (1964), p. 93.

[53] J. Pavan, A. F. Viñas, P. H. Yoon, L. F. Ziebell, and R. Gaelzer, *Solar Wind Strahl Broadening by Self-generated Plasma Waves*, Astrophys. J. Lett., 769 (2013), p. L30.

[54] V. Pierrard, M. Lazar, S. Poedts, Š. Štverák, M. Maksimovic, and P. M. Trávníček, *The Electron Temperature and Anisotropy in the Solar Wind. Comparison of the Core and Halo Populations*, Solar Phys., 291 (2016), pp. 2165–2179.

[55] W. G. Pilipp, K.-H. Muehlhaeuser, H. Miggenrieder, M. D. Montgomery, and H. Rosenbauer, *Characteristics of electron velocity distribution functions in the solar wind derived from the HELIOS plasma experiment*, J. Geophys. Res., 92 (1987), pp. 1075–1092.

[56] M. P. Pulupa, S. D. Bale, C. Salem, and K. Horaites, *Spin-modulated spacecraft floating potential: Observations and effects on electron moments*, Journal of Geophysical Research (Space Physics), 119 (2014), pp. 647–657.

[57] S. K. Rathgeber, R. Fischer, S. Fietz, J. Hobirk, A. Kallenbach, H. Meister, T. Pütterich, F. Ryter, G. Tardini, E. Wolfrum, and ASDEX Upgrade Team, *Estimation of profiles of the effective ion charge at ASDEX Upgrade with Integrated Data Analysis*, Plasma Physics and Controlled Fusion, 52 (2010), p. 095008.

[58] I. G. Richardson and H. V. Cane, *Near-Earth Interplanetary Coronal Mass Ejections During Solar Cycle 23 (1996 - 2009): Catalog and Summary of Properties*, Solar Phys., 264 (2010), pp. 189–237.

[59] H. Rosenbauer, R. Schwenn, E. Marsch, B. Meyer, H. Miggenrieder, M. D. Montgomery, K. H. Muehlhaeuser, W. Pilipp, W. Voges, and S. M. Zink, *A survey on initial results of the HELIOS plasma experiment*, Journal of Geophysics Zeitschrift Geophysik, 42 (1977), pp. 561–580.

[60] S. Saeed, M. Sarfraz, P. H. Yoon, M. Lazar, and M. N. S. Qureshi, *Electron heat flux instability*, MNRAS, 465 (2017), pp. 1672–1681.

[61] S. Saito and S. P. Gary, *All whistlers are not created equally: Scattering of strahl electrons in the solar wind via particle-in-cell simulations*, Geophys. Res. Lett., 34 (2007), p. L01102.

[62] ——, *Whistler scattering of suprathermal electrons in the solar wind: Particle-in-cell simulations*, Journal of Geophysical Research (Space Physics), 112 (2007), p. A06116.

[63] S. Saito, S. P. Gary, H. Li, and Y. Narita, *Whistler turbulence: Particle-in-cell simulations*, Physics of Plasmas, 15 (2008), p. 102305.

[64] C. Salem, J.-M. Bosqued, D. E. Larson, A. Mangeney, M. Maksimovic, C. Perche, R. P. Lin, and J.-L. Bougeret, *Determination of accurate solar wind electron parameters using particle detectors and radio wave receivers*, J. Geophys. Res., 106 (2001), pp. 21701–21717.

[65] C. Salem, D. Hubert, C. Lacombe, S. D. Bale, A. Mangeney, D. E. Larson, and R. P. Lin, *Electron Properties and Coulomb Collisions in the Solar Wind at 1 AU: Wind Observations*, Astrophys. J., 585 (2003), pp. 1147–1157.

[66] J. D. Scudder and S. Olbert, *A theory of local and global processes which affect solar wind electrons. II - Experimental support*, J. Geophys. Res., 84 (1979), pp. 6603–6620.

[67] J. Seough, Y. Nariyuki, P. H. Yoon, and S. Saito, *Strahl Formation in the Solar Wind Electrons via Whistler Instability*, Astrophys. J. Lett., 811 (2015), p. L7.

[68] D. Sigmar and G. Joyce, *Plasma heating by energetic particles*, Nuclear Fusion, 11 (1971), p. 447.

[69] H. M. Smith, E. Marsch, and P. Helander, *Electron Transport in the Fast Solar Wind*, Astrophys. J., 753 (2012), p. 31.

[70] H. B. Snodgrass and R. K. Ulrich, *Rotation of Doppler features in the solar photosphere*, Astrophys. J., 351 (1990), pp. 309–316.

[71] L. Spitzer and R. Härm, *Transport Phenomena in a Completely Ionized Gas*, Physical Review, 89 (1953), pp. 977–981.

[72] D. Stansby, T. S. Horbury, C. H. K. Chen, and L. Matteini, *Experimental Determination of Whistler Wave Dispersion Relation in the Solar Wind*, Astrophys. J. Lett., 829 (2016), p. L16.

[73] S. M. Tobias, F. Cattaneo, and S. Boldyrev, *MHD Dynamos and Turbulence,* in *Ten Chapters in Turbulence, ed. P.A. Davidson, Y. Kaneda, and K.R. Sreenivasan : Cambridge University Press, p. 351-404.* , 2013.

[74] D. Told, J. Cookmeyer, F. Muller, P. Astfalk, and F. Jenko, *Comparative study of gyrokinetic, hybrid-kinetic and fully kinetic wave physics for space plasmas*, New Journal of Physics, 18 (2016), p. 065011.

[75] Y. Tong, S. D. Bale, C. Salem, and M. Pulupa, *Observed instability constraints on electron heat flux in the solar wind*, ArXiv e-prints, (2018).

[76] Š. Štverák, M. Maksimovic, P. M. Trávníček, E. Marsch, A. N. Fazakerley, and E. E. Scime, *Radial evolution of nonthermal electron populations in the low-latitude solar wind: Helios, Cluster, and Ulysses Observations*, Journal of Geophysical Research (Space Physics), 114 (2009), p. 5104.

[77] Š. Štverák, P. Trávníček, M. Maksimovic, E. Marsch, A. N. Fazakerley, and E. E. Scime, *Electron temperature anisotropy constraints in the solar wind*, Journal of Geophysical Research (Space Physics), 113 (2008), p. 3103.

[78] Š. Štverák, P. M. Trávníček, and P. Hellinger, *Electron energetics in the expanding solar wind via Helios observations*, Journal of Geophysical Research (Space Physics), 120 (2015), pp. 8177–8193.

[79] B. van der Holst, W. B. Manchester, IV, K. G. Klein, and J. C. Kasper, *Predictions for the First Parker Solar Probe Encounter*, Astrophys. J. Lett., 872 (2019), p. L18.

[80] D. Verscharen, K. G. Klein, and B. Maruca, *The Multi-Scale Nature of the Solar Wind*, AGU Fall Meeting Abstracts, (2018).

[81] A. Viñas, C. Gurgiolo, T. Nieves-Chinchilla, S. Gary, and M. Goldstein, *Whistler waves driven by anisotropic strahl velocity distributions: Cluster observations*, Proc. Twelfth International Solar Wind Conference, (2010).

[82] C. Vocks and G. Mann, *Generation of Suprathermal Electrons by Resonant Wave-Particle Interaction in the Solar Corona and Wind*, Astrophys. J., 593 (2003), pp. 1134–1145.

[83] C. Vocks, C. Salem, R. P. Lin, and G. Mann, *Electron Halo and Strahl Formation in the Solar Wind by Resonant Interaction with Whistler Waves*, Astrophys. J., 627 (2005), pp. 540–549.

[84] L. B. Wilson, A. Koval, A. Szabo, A. Breneman, C. A. Cattell, K. Goetz, P. J. Kellogg, K. Kersten, J. C. Kasper, B. A. Maruca, and M. Pulupa, *Electromagnetic waves and electron anisotropies downstream of supercritical interplanetary shocks*, Journal of Geophysical Research (Space Physics), 118 (2013), pp. 5–16.

[85] P. Wurz, *Solar Wind Composition*, in The Dynamic Sun: Challenges for Theory and Observations, vol. 600 of ESA Special Publication, Dec. 2005, p. 44.1.

[86] D. Zwillinger, *CRC Standard Mathematical Tables and Formulae*, 2011.